

Optical Antennas

INAUGURALDISSERTATION

zur

Erlangung der Würde eines Doktors der Philosophie
vorgelegt der
Philosophisch-Naturwissenschaftlichen Fakultät
der Universität Basel

von

Peter Mühlischlegel

aus Biberach an der Riss, Deutschland



Basel, 2006

Genehmigt von der Philosophisch-Naturwissenschaftlichen Fakultät auf Antrag von:

Prof. Dr. D. W. Pohl
Prof. Dr. B. Hecht
Prof. Dr. H.-J. Güntherodt

Basel, Februar 2006

Prof. Dr. H.-J. Wirz, Dekan

Scientific Publications

Resonant Optical Antennas

P. Mühlischlegel, H.-J. Eisler, O.J.F. Martin, B. Hecht and D.W. Pohl
Science, 308:1607-1608, 2005.

Glue-free tuning fork shearforce microscope

P. Mühlischlegel, J. Toquant, D. W. Pohl, and B. Hecht
Rev. Sci. Instrum., 77:016105, 2006.

Tip Enhancement, Chapter: Single emitters and optical antennas

B. Hecht, P. Mühlischlegel, J.N. Farahani, H.-J. Eisler, O.J.F. Martin and D.W. Pohl
Advances in NANO-OPTICS and NANO-PHOTONICS, Edited by S. Kawata and V.M. Shalaev, *Elsevier* 2006.

Contributing Talks

Near-Field of Optical Antennas

P. Mühlischlegel, H.-J. Eisler, D.W. Pohl, B. Hecht
NFO 8, Seoul 2004.

Optical Antennas

P. Mühlischlegel, J. Farahani, H.-J. Eisler, D.W. Pohl, B. Hecht
NCCR Meeting, Gwatt 2005.

Resonant Optical Antennas for Single Molecule Spectroscopy

P. Mühlischlegel, J. Farahani, H.-J. Eisler, D.W. Pohl, B. Hecht
ICN+T, Basel 2006.

Summary

Efficient interconversion of propagating light and localized, enhanced fields is instrumental for advances in optical characterization, manipulation and (quantum) optical information processing on the nanometer-scale. A resonant optical antenna (OA) might be an optimum structure that links propagating radiation and confined/enhanced optical fields.

This thesis is concerned with the fabrication and investigation of optical antennas (OAs). We demonstrate that gold dipole and bow-tie antennas can be designed and fabricated to match optical wavelengths. For instance we fabricated slim gold dipole antennas with total lengths L in the half-wavelength range ($L = 190$ to 400 nm) on an ITO-coated glass cover slides. Micro-fabrication was performed in a two step process, applying a combination out of electron lithography and focused ion beam milling.

For OA studies we built up a scanning confocal optical microscope (SCOM) with a polarization-controlled, picosecond pulsed light source. The SCOM design aimed on the excitation and detection of nonlinear effects like the two-photon photoluminescence of gold (TPPL) in individual nano structures. Using SCOM we analyzed dipole antennas and stripes of different length.

We have identified specific antenna effects, like field-confinement and enhancement in the antenna feed gap. Upon illumination with picosecond laser pulses, white-light supercontinuum (WLSC) radiation is generated in the antenna feed gap in addition to two-photon photoluminescence (TPPL) in the antenna arms. The strength of emission and order of nonlinearity was used as a measure for the field enhancement at the position of an OA structure. On resonance strong field enhancement in the antenna feed gap drives even highly nonlinear phenomena like WLSC. The antenna length at resonance is considerably shorter than one half of the effective wavelength of the incident light. This is in contradiction to classical antenna theory, but in qualitative accordance with computer simulations that take into account the finite metallic conductivity at optical frequencies.

Computer simulations revealed that an antenna resonance is also present for aluminium dipole antennas. The resonance length of a aluminium antenna is close to one half of the effective wavelength, in agreement with classical antenna theory. In contrast to gold, aluminum dipole antennas show a much broader resonance and four times less intensity enhancement at the wavelength investigated (830 nm). Surface plasmon resonances can be excluded for aluminium antennas at this wavelength and structural dimension. Therefore the strong enhancement and shift in resonance length of the gold dipole antenna can be explained with the excitation of a surface plasmon mode with strong field concentration in the antenna feed gap. This means, that the existence of surface plasmon resonances in suitably designed antennas can greatly enhance antenna performance in the optical wavelength range.

The dimensions of the OA feed gap are far below the diffraction limit, and field distributions are only directly accessible by near-field microscopy techniques. The implementation of a scanning tunnelling optical microscope (STOM) was aimed at the direct detection of the optical near-field distribution around OAs. In a new design of the STOM scan head, fixation of the optical fiber is achieved by means of controlled pressure and elastic deformation. The avoidance of glued connections was found to improve the Q factor of the shear force sensor as well as to facilitate the replacement of the fiber probe. Illumination of the antenna structure was achieved under total internal reflection with s- and p-polarized light and three different wavelength (532 nm, 675 nm, 830 nm). A shear-force feedback system allowed for a direct comparison between optical and topographic image.

STOM measurements on a single bow-tie structure ($L = 300$ nm) revealed a field-confinement in the antenna feed gap for a polarization parallel to the antenna long axis and an excitation wavelength of 830 nm, which was absent for the other wavelengths and polarizations. The observed field localization is in qualitative agreement with computer simulations.

Future work in this field will concentrate on the exploration of OAs for high resolution SNOM imaging and on the investigation of the interaction of OAs with single-quantum systems.

Contents

Summary	v
1. Introduction	1
1.1. Overview	3
1. Basics	5
2. Antenna Theory	6
2.1. Dipole Antenna: Simple Model	6
2.2. Radiated Fields	8
2.3. Infinitesimal Dipole	11
2.4. Dipole Antenna:	
Quantitative Description	13
2.4.1. Antenna Current Distribution	13
2.4.2. Antenna Input Impedance	15
2.4.3. Transmission Properties	16
2.4.4. Receiving Properties	18
2.5. Bow-tie Antenna	22
3. Optical Properties of Metals and Metal Particles	23
3.1. Drude-Sommerfeld Model	24
3.1.1. Skin Depth	25
3.2. Localized Surface Plasmon Resonances	25
3.2.1. Plasmon Resonances of Spherical Particles	26
3.2.2. Plasmon Resonances of Elliptical Particles	28
4. Antennas at Optical Frequencies	30

II. Experimental	32
5. Sample Preparation	33
5.1. E-Beam Lithography	33
5.2. Focused Ion Beam Structuring	35
5.3. Nanorod Modification by FIB	38
6. Microscopy Techniques	40
6.1. Scanning Tunnelling Optical Microscopy	40
6.1.1. Description of the Experimental Setup	41
6.2. Confocal Optical Microscopy	43
6.2.1. Principles of Confocal Microscopy	43
6.2.2. Description of the Experimental Setup	45
6.2.3. Polarization Adjustment	46
6.2.4. Laser Pulse Width	47
III. Results	50
7. White-light Continuum Generation by Resonant Optical Antennas	51
7.1. Experimental	51
7.2. Results and Discussion	53
7.3. Summary	60
8. Near-field Studies of Optical Antennas	61
8.1. Experimental	62
8.2. FDTD Simulations	63
8.3. Results and Discussion	64
8.4. Summary	69
Bibliography	70
A. First Appendix	81
A.1. Glue-free tuning fork shear-force microscope	81
A.1.1. Introduction	81
A.1.2. Design and Characterization	82
A.1.3. Operation	86

A.1.4. Summary	88
B. Second Appendix	89
B.1. Programming	89
B.1.1. antenna.m	89
B.1.2. plasmon.m	91
C. Third Appendix	93
C.1. Overview of Analyzed Optical Antennas	93

1. Introduction

A number of nano-optical methods [1] have been developed in recent years that allow for optical characterization with a resolution much smaller than the diffraction limit ($\sim \lambda/2$). They are based on the confinement of electromagnetic (e.m.) fields by appropriate shaped nano-structures used instead of focusing lenses and mirrors. Prominent structures used for field confinement and local enhancement are small apertures and tips, used as probes in scanning near-field optical microscopy (SNOM) [2, 3]. Such 'conventional' probes were used, for instance, to establish one- and two-photon fluorescence imaging and Raman spectroscopy with spacial resolution < 20 nm [4–6]. The structural design of conventional near-field probes is relatively simple, which leads to a limitation in achievable confinement and enhancement for e.m. fields.

Key for the improvement of near-field probes might be the concept of the *optical antenna* (OA), a nanometer sized metal structure similar to a radio wave antenna, but down-scaled in size. Classical antennas, such as radio wave antennas, are designed to efficiently capture e.m. waves and to confine their energy in a small volume ($\ll \lambda/2$ in all dimensions) called feed gap. The functional analogy of near-field probes with classical antennas was recognized by several authors [7–12], but so far no systematic studies of OAs exist.

Efficient interconversion of propagating light and localized, enhanced fields is not only instrumental for advances in optical characterization [3, 6, 13–15], but also for optical manipulation [16–18], and (quantum) optical information processing [19–23] on the nanometer-scale. This requirement recently triggered a search for favorable structures [3, 6, 9–15, 23–27] and materials [20, 28]. Resonant OAs excel among other structures by combining (i) field-line concentration at a local shape singularity i.e. a gap [3, 6], (ii) optimum impedance matching to freely propagating waves, and (iii) resonant collective oscillations (plasmons) of the free electron gas [14, 15, 21, 27] in the antenna arms. While the field enhancement in the feed gap obviously increases with decreasing width [26], variation of the overall antenna length should result in a pronounced resonance in

analogy to the radio wavelength regime.

The nanometer-scale dimensions of optical antennas raise a twofold experimental challenge, viz. manufacturing with sufficient precision and identification of specific antenna effects. The first challenge can be met by means of modern micro-fabrication techniques, demonstrated for bow-tie antennas at infrared and, more recently, at optical frequencies [9, 10, 25, 26]. In this work we could successfully fabricate nanometer sized dipole and bow-tie antennas by means of a combination of electron beam lithography and focused ion beam milling.

The identification of specific antenna effects is the second experimental challenge. The dielectric properties of metals at optical frequencies very much deviate from those of metals at radio frequencies. Therefore antenna performance could strongly be influenced by the optical properties of metals.

For systematic antenna studies we built a scanning confocal optical microscope (SCOM) with a polarization controlled, picosecond (ps) pulsed light source. The high optical fields e.g. in the focus of a pulsed laser source are able to excite nonlinear processes in materials, like the two-photon photoluminescence (TPPL) of gold [26, 29, 30], leading to white light emission. Specific antenna effects were identified by detecting white light emission from OAs and stripes in different length using a ps laser pulses powerful enough to excite white-light super-continuum (WLSC) [31–33] in addition to TPPL, and by comparing explicitly the responses of OAs and stripes.

Recording white light emission as a function of antenna length revealed a pronounced OA resonance. The experiment showed that field enhancement by a resonant OA is able to excite in addition to TPPL a highly nonlinear processes like WLSC generation. The detected white light emission from antennas was up to three orders of magnitude higher than that from solid gold stripes of the same size but without feed gap. The conclusion that WLSC emission origins from the antenna feed gap was confirmed by numerical simulations. The simulations showed that the field enhancement in the feed gap reaches intensity levels sufficient to achieve dielectric breakdown [34].

The strong localized field enhancement in the gap of an OA results in strong energy density gradients, which may allow for trapping of nanometer-sized polarizable particles, too small to be trapped in a classical light focus [16]. In addition to field confinement OAs provides unusual illumination properties. The WLSC originating from the feed gap volume may allow for new forms of local spectroscopy and interactions with nano-structures and single-quantum systems. The findings could contribute to improved designs of sen-

sors based on surface-enhanced Raman scattering (SERS) and allow for single-molecule sensitivity [13] in high resolution SNOM imaging.

We have showed that ideas from classical antenna theory can be even applied in the optical regime. This could further greatly facilitate the search for optimum field enhancement devices, by tapping the vast knowledge of classical antenna theory. Last but not least not only receiving properties of OAs are of interest for nanoscale science. In the reversed case, by using an OA as emitter, the emission of a fluorescent molecule placed in the feed gap could be greatly enhanced [35, 36].

In a different approach we intended to directly image the optical near-field of a bow-tie antenna using a home-built scanning tunnelling optical microscope (STOM). The near-field images revealed field-confinement in the antenna gap for a certain polarization and wavelength, which is in agreement with computer simulations.

1.1. Overview

This work is organized in three parts. The first part gives an overview on radio wave antenna theory and solid state theoretical concepts, both expected to be relevant for the function of optical antennas.

Chap. 2 is concerned with classical antenna theory, with emphasis on dipole antennas. The importance of the current density distribution for optimum antenna performance is discussed and the resonance length of a classical dipole antenna is determined and explained.

Chap. 3 addresses the difference of metals at optical frequencies compared to the radio frequency regime. The finite permittivity of metals influences the penetration depth of e.m. fields into metals and allows for surface plasma resonances in small particles. These effects are expected to alter the antenna properties at optical frequencies.

Chap. 4. is intended to give a physical understanding in which respect the properties of antennas are altered by the optical properties of metals. Methods are introduced, that have been used for near-field simulations of optical antennas.

The second part of this theses describes the experimental methods used to fabricate and investigate OA performance.

Chap. 5 discusses various lithographic methods for optical antenna preparation and gives

details on the structuring process.

Chap. 6 gives an introduction to the applied microscopy techniques used to identify specific OA effects. The home-build setups are described with emphasis on some important experimental aspects. These are for instance the implementation of a constant gap mode by a newly designed shear-force microscope, the control of polarization and the measurement of the pulse width of the excitation laser.

The last part contains the main results of this thesis.

Chap. 7 discusses the measurements used to identify specific OA effects. SCOM images, power and polarization dependence, the emission spectrum and the resonance of optical dipole antennas of different lengths are presented.

Chap. 8 discusses the approach to identify local field enhancement in the antenna feed gap using STOM. Optical near-field measurements of a bow-tie structure are presented. STOM images obtained for different polarizations and wavelengths are discussed and compared with near-field computer simulations.

Part I.

Basics

2. Antenna Theory

This chapter gives a short introduction to classical antenna theory, with emphasis on dipole antennas.

First we introduce a simple model of a dipole antenna, that motivates why antennas radiate electro magnetic (e.m.) radiation and why antennas of certain length produce better field confinement than others. Then we outline a formalism, that allows us to calculate the fields radiated by an antenna. The model of an infinitesimal dipole (ID) is used to discuss the different character of the fields in near- and far-field region. The ID model further helps to appreciate the difference between the radiated power and the power stored in the near-field of an antenna. Then we analyze the dipole antenna in more detail. A realistic current density of a dipole antenna is obtained using Pocklington's integral equation. The antenna input impedance is defined and the concept of an equivalent antenna circuit is introduced. The representation of an antenna by an impedance simplifies the calculation of transmitted and received power for antennas of different length. These concepts are used to find the optimum dipole antenna length for which the transmitted or received power are maximal.

2.1. Dipole Antenna: Simple Model

A two wire transmission line (Fig 2.1A) fed by an alternating voltage source, is a very inefficient radiator. The current is reflected at the termination, which results in a standing wave along the line. Since the current in each line element has opposite phase, radiation tends to cancel in the far-field due to destructive interference. By bending the end of the two wires in opposite directions the structure becomes a dipole antenna. This structure radiates much more efficient, since now the currents in the antenna arms are in phase [37] (see Fig 2.1B). The time average current $|I_g|$ in the antenna circuit increases and the generator has to deliver power to maintain the radiation. Since the current distribution along the transmission line is sinusoidal, we expect that also the

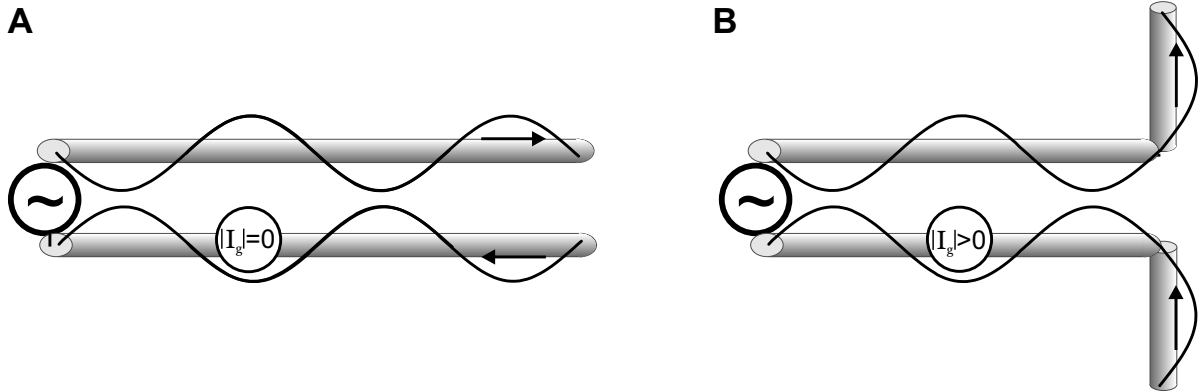


Figure 2.1.: Sketch of transmission line without (A) and with (B) dipole antenna.

current along the arms of the antenna is sinusoidal. Actually this is a good approximation for thin antennas (with radius $a < 0.05\lambda$ [37]) and even for thicker antennas which do not exceed $\lambda/2$ in length [38]. The sinusoidal current distribution is given by [38, 39]

$$I_s(z) = I_m \sin(k(\frac{1}{2}L - |z|)) \quad , \quad (2.1)$$

where I_m is the current amplitude, L the total antenna length, a the radius of the wire and k the wave vector. This first approximation is already very useful to calculate radiation patterns for different antenna length L (see section 2.2), but since I_m is not specified it is difficult to compare the radiated power between antennas of different length. However by using Eq. (2.1) one can motivate why some antenna lengths are more suitable for field confinement than others. The continuity equation $\frac{d}{dt}\rho(\mathbf{x}, t) = -\nabla \cdot \mathbf{J}(\mathbf{x})$ can be simplified for a time harmonic one dimensional current density along the z-axes. In this case it reads as

$$\frac{d}{dt}\rho(z)e^{-i\omega t} = -\frac{d}{dz}I(z)e^{-i\omega t} \quad , \quad (2.2)$$

which shows that the charge density $\rho(z)$ is proportional to the first derivative of the current $I(z)$. Figure 2.2A-B compares the current and charge density of a half-wave ($L = \lambda/2$) with that of a full-wave ($L = \lambda$) dipole antenna. The current of the half-wave antenna drops from its maximum value to zero right at the antenna feed-gap. This discontinuity results in a singularity for the charge density and hence in a high amount of closely packed opposite charges, facing each other over the narrow feed-gap (Fig. 2.2C). This leads to a large field confined inside the feed-gap.

The current of the full-wave antenna has no maximum and therefore no discontinuity at

the gap (assuming a infinite small gap). Therefore charges are much less concentrated and fields in the gap are much smaller (Fig. 2.2D).

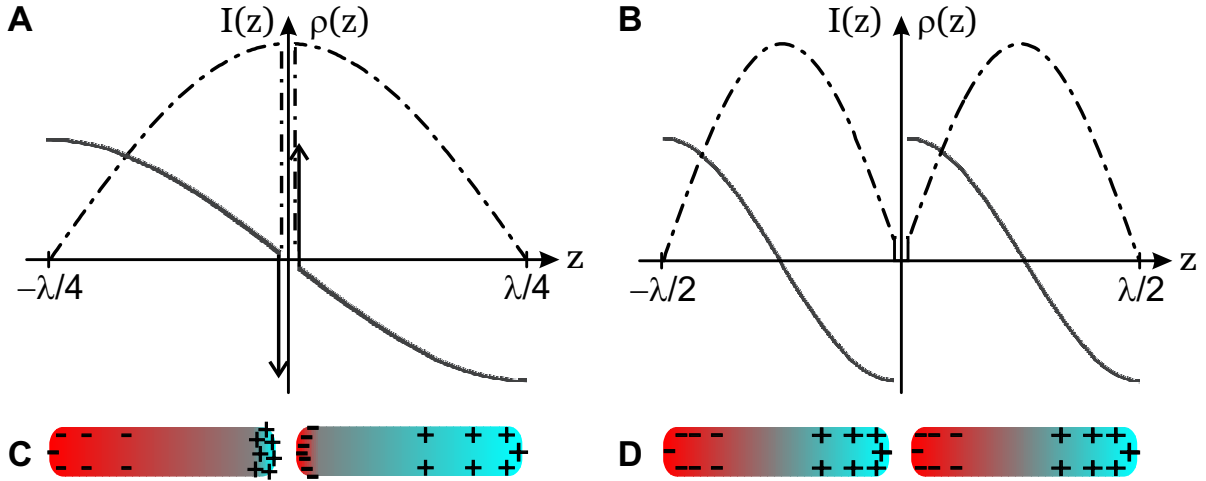


Figure 2.2.: Sinusoidal approximation: Comparison between half-wave and full-wave dipole antenna. (A) Current density (dashed dotted line) and charge density (solid line) of a half-wave antenna. Note singularity (indicated by arrows) at the feed gap for the half-wave antenna. (B) Same as in (A) for full-wave dipole antenna. (C)-(D) Surface charges, expected from charge density, for half- and full-wave dipole.

2.2. Radiated Fields

We now outline a formalism to calculate the fields radiated and scattered by an antenna. For a detailed derivation of the presented formulas from Maxwell's equations we refer to text books [37, 39].

The physical origin of radiation are accelerated charges along the antenna. The charges, whether in a transmitting or receiving antenna are driven by an external field \mathbf{E}^{ex} . For a transmitting antenna the external field is given by: $\mathbf{E}^{ex} = V_0/\Delta$, where V_0 is the generator voltage, applied locally to the antenna input terminals over the feed gap size Δ . In the receiving mode the incoming field drives the charges and a voltage over the feed-gap is the measured signal. In both cases, the external field induces a current density \mathbf{J} in the antenna arms (Fig. 2.3A, B). In turn the current generates its own field \mathbf{E}^s , that is radiated/scattered by the antenna. The total electric field is given

as:

$$\mathbf{E}^t(\mathbf{r}) = \mathbf{E}^{ex}(\mathbf{r}) + \mathbf{E}^s(\mathbf{r}) . \quad (2.3)$$

The fields must satisfy Maxwell's equation and in addition fulfill boundary conditions

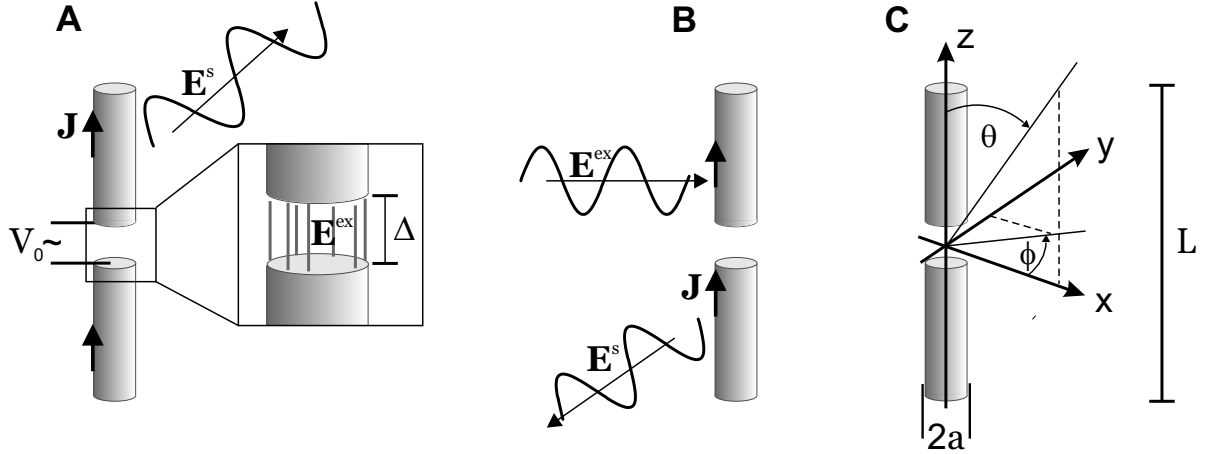


Figure 2.3.: Transmitting (A) and receiving (B) dipole antenna. V_0 : Generator voltage. \mathbf{E} : External field. Δ : Feed-gap size. \mathbf{E}^s : Radiated/scattered field. \mathbf{J} : Current density. (C) Coordinate systems used for antenna description.

given by the shape and material properties of the antenna. Note, that in a similar way scattering by arbitrary particles can be formulated [40].

Metals at radio frequency can be assumed to be perfect conductors. Therefore the tangential components of the total electric field vanish at the antenna surface, which is a generally used boundary condition in classical antenna theory. We emphasize, that the radiating/receiving antenna is an electromagnetic boundary value problem in which the current distribution on the arms of the antenna emerges as part of the solution, not as input [41].

The coordinate system shown in Fig. 2.3C is used for the following theoretical description of antennas. Provided that the current density is known, the vector potential \mathbf{A} can be determined by

$$\mathbf{A}(x, y, z) = \frac{\mu}{4\pi} \int_V \mathbf{J}(x', y', z') \frac{e^{-ikR}}{R} dV' . \quad (2.4)$$

where the primed coordinates represent the source points inside or on the surface of the antenna volume V . The unprimed coordinates represent the observation point, and R the distance from any source point to the observation point and is given by

$$R = \sqrt{(x - x')^2 + (y - y')^2 + (z - z')^2} . \quad (2.5)$$

Although magnetic sources are not physical, in fact both electrical and magnetic equivalent current densities are used to represent actual antenna systems. For example an aperture antenna, such as a waveguide or horn, can be represented by an equivalent magnetic current density \mathbf{M} [41, 42]. Therefore a second vector potential is introduced

$$\mathbf{F}(x, y, z) = \frac{\varepsilon}{4\pi} \int_V \mathbf{M}(x', y', z') \frac{e^{-ikR}}{R} dv' . \quad (2.6)$$

Once the vector potentials \mathbf{A} and \mathbf{F} have been found the electric and magnetic fields radiated by the antenna are given by [37]

$$\begin{aligned} \mathbf{E} &= \mathbf{E}_A + \mathbf{E}_F = -i\omega\mathbf{A} - i\frac{1}{\omega\mu\varepsilon}\nabla(\nabla \cdot \mathbf{A}) - \frac{1}{\varepsilon}\nabla \times \mathbf{F} , \\ \mathbf{H} &= \mathbf{H}_A + \mathbf{H}_F = \frac{1}{\mu}\nabla \times \mathbf{A} - i\omega\mathbf{F} - i\frac{1}{\omega\mu\varepsilon}\nabla(\nabla \cdot \mathbf{F}) , \end{aligned} \quad (2.7)$$

where ω is the frequency of the external field, μ and ε are determined by the magnetic and dielectric properties of the surrounding medium and the wavevector is given by $k = \omega\sqrt{\mu\varepsilon}$. In the following we consider only electric currents and hence F the part coming from the magnetic sources, is set to zero. Therefore (2.7) simplifies to

$$\begin{aligned} \mathbf{E} &= -i\omega\mathbf{A} - i\frac{1}{\omega\mu\varepsilon}\nabla(\nabla \cdot \mathbf{A}) , \\ \mathbf{H} &= \frac{1}{\mu}\nabla \times \mathbf{A} . \end{aligned} \quad (2.8)$$

The fields, radiated by an antenna, are connected with a transport of e.m. energy. The quantity used to describe the power density associated with an e.m. is the instantaneous Poynting vector

$$\mathbf{S} = \mathbf{E} \times \mathbf{H} . \quad (2.9)$$

Since most instruments measure the time average of the fast oscillating e.m fields, it is instructive to define the time average pointing vector \mathbf{W} , that writes in the complex representation as [37]

$$\mathbf{W} = \frac{1}{2}(\mathbf{E} \times \mathbf{H}^*) . \quad (2.10)$$

\mathbf{W} represents the complex average power density associated with the radiated fields.

The complex average power moving in the radial direction is obtained by integrating \mathbf{W} over a closed sphere S of radius r

$$P = \oint_S \mathbf{W} \cdot d\mathbf{s} = P_r + iP'_{reac} . \quad (2.11)$$

The real part P_r is associated with the total radiated power and represents a measurable far-field quantity. Typical antenna characteristics like the *directivity* and the *gain* of an antenna are based on P_r [37]. The imaginary part P'_{react} can be associated with the reactive power stored in the reactive near-field of an antenna, which will be clarified in the next section.

2.3. Infinitesimal Dipole

A wire with length l and radius a both much smaller than the wavelength is regarded as infinitesimal dipole (ID). The current density inside the ID is assumed to be constant. By specifying the source, the fields are simply derived by (2.4) and (2.8). The fields of an ID are instructive to clarify terms like far- and near-field as well as radiated and reactive power. The ID can be seen as building block for more complex antenna structures. In addition it helps to make a link between particle plasmons and antennas.

For an ID or point source, placed at the origin of the coordinate system (2.5) reduces to $R \approx r = \sqrt{x^2 + y^2 + z^2}$, and the vector potential (Eq. 2.4) is given by

$$\mathbf{A}(\mathbf{x}) = \frac{\mu}{4\pi} \frac{e^{-ikr}}{r} \int_V \mathbf{J}(\mathbf{x}') d\mathbf{x}' . \quad (2.12)$$

Since the current density is assumed to be constant it is expressed by a linear current element $\mathbf{J}(\mathbf{x}) = I_0 \mathbf{e}_z$ along the z-axis [37]. The integral in (2.12) simplifies to

$$\int_V \mathbf{J}(\mathbf{x}') d\mathbf{x}' = \mathbf{e}_z I_0 \int_{-l/2}^{l/2} dz' = \mathbf{e}_z I_0 l , \quad (2.13)$$

where \mathbf{e}_z is a unit vector. By transforming \mathbf{A} and (2.8) into spherical coordinates, the radiated e.m.-dipole-field writes as [37]

$$\begin{aligned} H_r &= H_\theta = 0 , \\ H_\phi &= i \frac{k I_0 l \sin(\theta)}{4\pi r} \left[1 + \frac{1}{ikr} \right] e^{-ikr} \end{aligned} \quad (2.14)$$

and

$$\begin{aligned}
 E_r &= \frac{I_0 l \cos(\theta)}{2\pi r^2} \left[1 + \frac{1}{ikr}\right] e^{-ikr} , \\
 E_\theta &= \frac{I_0 l \sin(\theta)}{4\pi r} \left[1 + \frac{1}{ikr} - \frac{1}{(kr)^2}\right] e^{-ikr} , \\
 E_\phi &= 0 .
 \end{aligned} \tag{2.15}$$

Note that the fields corresponds to the fields of an oscillating dipole with the dipole moment given by $\mathbf{p} = iI_0 l \mathbf{e}_z / \omega$ [41].

The fields character depends strong on the distances to the source and is usually classified in the following way. In the *reactive near-field*, $r \ll \lambda$, only field terms which drop faster then $1/r$ ($1/r^3$ for E- and $1/r^2$ for H-field) are considered. The electric field, apart from its oscillation in time, is similar to the static electric dipole-field with non-vanishing radial components. Since the H-field term depends only on $1/r^2$ the near-field is predominantly electric. In the *far-field*, $r \gg \lambda$ only terms with $1/r$ are considered. The radial components of the E-field vanish and E- and H-field components are perpendicular to each other and transverse. Since the variation in r is separable from variations in θ and ϕ the shape of the radiation pattern is no longer dependent on r .

The complex average pointing vector (2.10) writes for the ID-fields (see Eqs. 2.14) and 2.15) in spherical coordinates as

$$\mathbf{W} = \frac{1}{2} (\mathbf{a}_r E_\theta H_\phi^* - \mathbf{a}_\theta E_r H_\phi^*) = \mathbf{a}_r W_r + \mathbf{a}_\theta W_\theta ; , \tag{2.16}$$

where $\mathbf{a}_{r,\theta}$ represents the unit vectors. Since $d\mathbf{s} \perp \mathbf{a}_\theta W_\theta$, (2.11) simplifies and we can write the complex power moving in radial direction as [37]

$$P = \int_0^{2\pi} \int_0^\pi W_r r^2 \sin \theta \, d\theta \, d\phi = P_r + iP'_{reac} . \tag{2.17}$$

As shown in [37] p. 137 the radial component W_r has a real and an imaginary part, whereas the transversal component W_θ is purely imaginary. Therefore P_r represents the total radiated real power, since the real part of \mathbf{W} is totaly radial ($\mathbf{a}_r W_r \parallel d\mathbf{s}$). The transversal component $\mathbf{a}_\theta W_\theta$ is purely imaginary. This components do not leave the sphere and does not contribute to the integral in (2.17). Hence the imaginary part P'_{reac} does *not* represent the total reactive power stored in the near-field of the ID.

Later we will calculate the complex radiated power by means of the antenna input impedance. According to the ID we will interpret the real part as radiated and the imaginary part as reactive power. The difference will be, that the complex power calculated by the antenna input impedance fully includes the total reactive power, that we will denote as P_{react} .

2.4. Dipole Antenna: Quantitative Description

The dipole antenna (DA), two conducting wires separated by a small gap, is the most basic type of antenna. As discussed earlier, the approximated current density of a DA is sinusoidal. For the calculation of radiated and received power by an dipole antenna the first order approximation is not very useful, since the current amplitude is not specified. To determine the current amplitude and also to obtain better physical understanding it is worthwhile to analyze the DA as a electromagnetic boundary-value problem. One of the first solutions to this problem were given by H. C. Pocklington [43] and E. Hallén [44], both giving integral equations for the current distribution. In the following we will concentrate on Pocklington's solution, since it is more general and adaptable for many types of feed sources [37].

2.4.1. Antenna Current Distribution

This section describes how the current distribution of linear DA is found by means of the Pocklington's integral equation [37, 43]. Starting point is an external field \mathbf{E}^{ex} incident on a perfectly conducting wire. \mathbf{E}^{ex} induces a current density \mathbf{J} in the wire, which generates a radiated electric field \mathbf{E}^s (Fig. 2.3). At any point in space the total electric field \mathbf{E}^t is the sum of external field and radiated/scattered field Eq. (2.3). For a perfect conductor the current density flow is only in z-direction, along the surface. Neglecting edge effects the calculation of \mathbf{A} with (2.4) reduces to

$$A_z = \frac{\mu}{4\pi} \int_{-L/2}^{L/2} \int_0^{2\pi} J_z \frac{e^{ikR}}{R} a d\phi' dz' , \quad (2.18)$$

where $R = \sqrt{(x - x')^2 + (y - y')^2 + (z - z')^2} = \sqrt{\rho^2 + a^2 - 2\rho a \cos(\phi - \phi') + (z - z')^2}$. If the wire is very thin, the surface current density J_z is not a function of the azimuthal angle ϕ . Therefore an equivalent line/filament current I_z located at the antenna surface ($\rho = a$) can be defined as: $I_z(z') = 2\pi a J_z$. With this (2.18) writes as

$$A_z = \frac{\mu}{4\pi} \int_{-L/2}^{L/2} \left[\int_0^{2\pi} \frac{1}{2\pi a} I_z(z') \frac{e^{ikR}}{R} a d\phi' \right] dz' . \quad (2.19)$$

Using (2.8) the scattered field is given by

$$E_z^s = -i \frac{\omega}{k^2} \left(\frac{\partial}{\partial z^2} + k^2 \right) \int_{-L/2}^{L/2} I_z(z') G(z, z') dz' , \quad (2.20)$$

where $G(z, z') = \frac{1}{2\pi a} \int_0^{2\pi} \frac{e^{ikR}}{4\pi R} d\phi'$.

Solving this equation for the surface ($\rho = a$) of a perfect conducting cylinder, where the total field along the surface vanishes, we can set $E_z^s((\rho = a)) = E_z^{ex}((\rho = a))$, by which (2.20) is transformed into *Pocklington's* integral equation

$$-i \frac{k^2}{\omega} E_z^{ex}(\rho = a) = \int_{-L/2}^{L/2} I_z(z') \left[\left(\frac{\partial}{\partial z^2} + k^2 \right) G(z, z') \right] dz' . \quad (2.21)$$

This function can be discretized using the *method of moments* [37, 45] leading to a linear equation,

$$\sum_{m=-M}^M G_{nm} I_m = E_n^{ex} , \quad (2.22)$$

which can be solved numerically by inverting the matrix G_{nm} [45]. Finally the source has to be modelled. For small gaps the delta gap model is appropriate [37]. The delta gap model comprises to set the field E_n^{ex} in the gap to V_0/Δ (Δ =gap width) and to zero elsewhere (Fig. 2.3B). The calculation (see appendix B.1.1) of the complex one dimensional current density was performed by using the MATLAB function 'pocklington.m' implemented by S. J. Orfanidis [45].

A comparison between the sinusoidal current distribution and the realistic complex current density for various antenna lengths is shown in Fig. 2.4. For the calculation the antenna diameter was kept fix ($a = \lambda/500$) for all lengths. The sinusoidal distribution

was normalized to the maximum of the pocklington current. Note that for $L = \lambda/2$ the current is highest compared to other lengths and its maximum is right at the feed gap ($z = 0$).

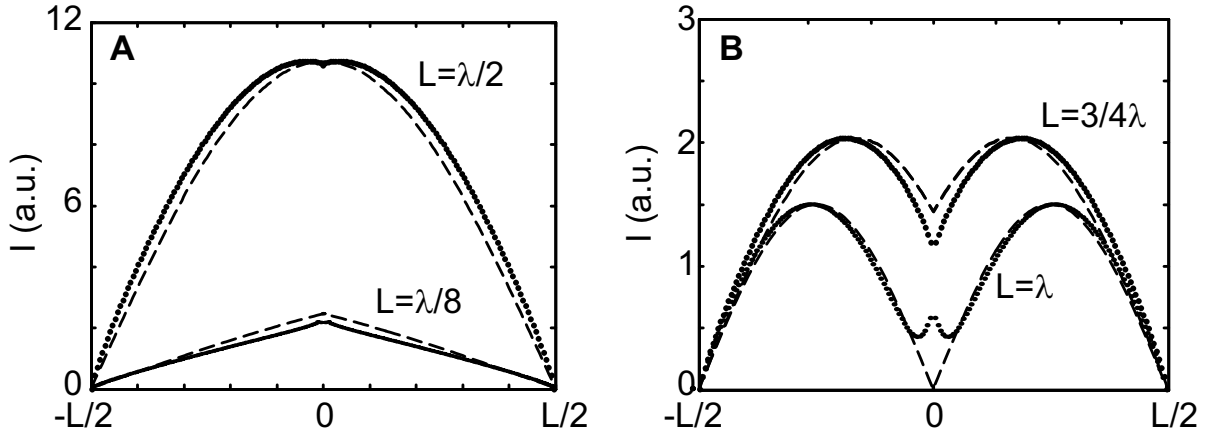


Figure 2.4.: One dimensional current densities for various antenna length L . Dashed line: Sinusoidal approximation. Dots: Pocklington's solutions for the current.

2.4.2. Antenna Input Impedance

The complex current distribution of an antenna could be found by solving the *Pocklington's* integral equation for ideal metals. Once the current distribution of a DA is given it is straight forward to calculate the vector potential (2.4) and the radiated fields (2.8). From this the time average radiated power can be calculated. A simpler way for the calculation of the received or transmitted power by an antenna is to use the concept of an equivalent circuit where the antenna is represented by its input impedance Z_a . Z_a is defined as the potential difference V_0 maintained at the feed gap divided by the current I_0 , and reads as [38, 39]

$$\begin{aligned} Z_a &= V_0/I_0 \\ &= R_a + iX_a = R_\Omega + R_r + iX_a. \end{aligned} \quad (2.23)$$

Z_a is usually a complex quantity. The real part R_a is a measure of how much power is consumed by an antenna. R_Ω denotes for ohmic losses inside the antenna, whereas the radiation resistance R_r , corresponds to losses due to radiation. The imaginary part X_a arises from the fact, that voltage V_0 and resulting current I_0 at the feed gap are not in phase [39] and is related to the reactive power stored in the near-field (see Eq. 2.17).

2. Antenna Theory

The impedance of the antenna was calculated by (2.23), where I_0 is obtained from the current distribution derived from Pocklington's integral equation with the delta gap model and $V_0 = 1$ V (see appendix B.1.1). Since Pocklington's solution assumes perfect conductors, we neglect R_Ω and set

$$R_a = R_r \quad (2.24)$$

for all further calculations.

Figure 2.5A shows a plot of the obtained Z_a , parameterized by the antenna length for two antennas with different ratios a/L . One appearing difference between the two ratios

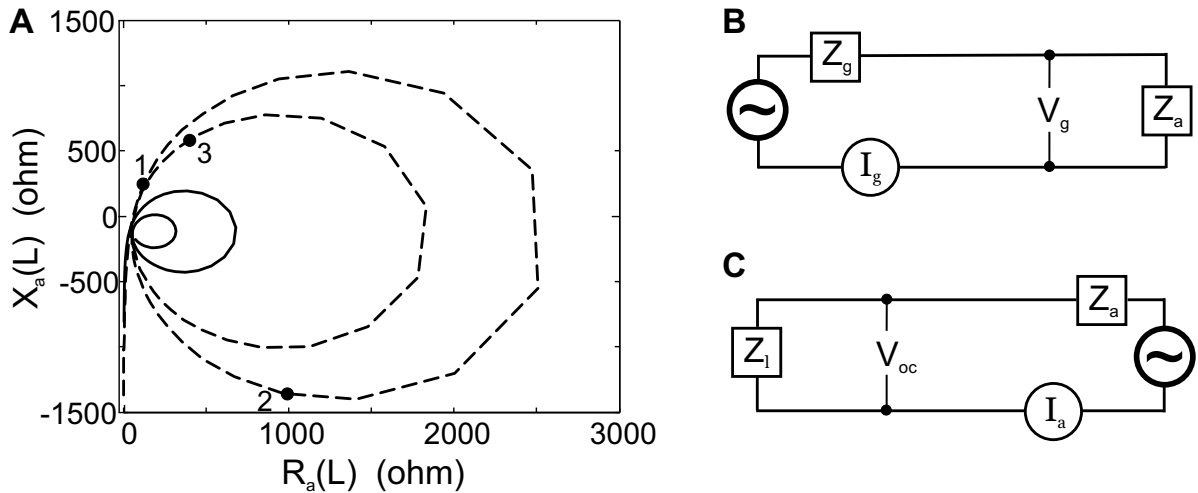


Figure 2.5.: (A) Input impedance for cylindrical center-fed dipoles with two different length-to-radius ratios L/a (solid line: $L/a = 100$, dashed line: $L/a = 4000$). The numbered dots correspond to $L = \lambda/2$ (1), $L = \lambda$ (2) and $L = 3/2 \lambda$ (3). (B)-(C) Thévenin equivalent circuit for a transmitting (B) and receiving (C) antenna. Z_g , Z_a , Z_l : Impedances of generator, antenna and load.

is the variation in impedance for different antenna length. The variation of Z_a with L reduces for thicker DA. For antenna lengths close to $\lambda/2$ the difference in Z_a almost vanishes.

With the definition of Z_a it is now possible to represent the antenna by a Thévenin equivalent circuit [37, 39]. In Figure 2.5B the Thévenin equivalent of an antenna operating as a transmitter is shown. A generator with an oscillating voltage V_g and self impedance Z_g drives the antenna represented by the Z_a . In the receiving case (Fig. 2.5C) the antenna with self impedance Z_a generates a voltage V_{oc} at the feed-gap, what drives the load Z_l . Knowing the currents I_g , I_a it is straight forward to calculate the transmitted and received power by an antenna.

2.4.3. Transmission Properties

The transmission properties of an antenna depends critically on Z_a . Z_a together with Z_g determines the current in the Thévenin equivalent circuit (see Fig 2.5B), which is given as: $I_g = V_g/(Z_g + Z_a)$. The total complex average power delivered to the antenna is then simply given by:

$$P = \frac{1}{2}|I_g|^2 Z_a = \frac{|V_g|^2}{2} \frac{R_a + X_a}{(R_a + R_g)^2 + (X_a + X_g)^2} = P_r + iP_{reac} . \quad (2.25)$$

From the analysis of the power radiated by a infinitesimal dipole (see Eq. 2.11) we already know that the imaginary part of P can be assigned to the reactive power flow P_{reac} , stored in the reactive near-field. This time P_{reac} represents the total reactive power. The real part of P has usually in addition to the radiative power P_r a resistive part P_Ω , which heats up the antenna structure due too ohmic losses in the metal. Since ohmic losses are neglected for the calculation of Z_a (see Eq. 2.24), P_Ω is not included in (2.25).

Figure 2.6A shows absolute real and imaginary part of P for a dipole antenna versus the antenna length. For the calculation of P we set Z_g to zero. Notice that the maximum

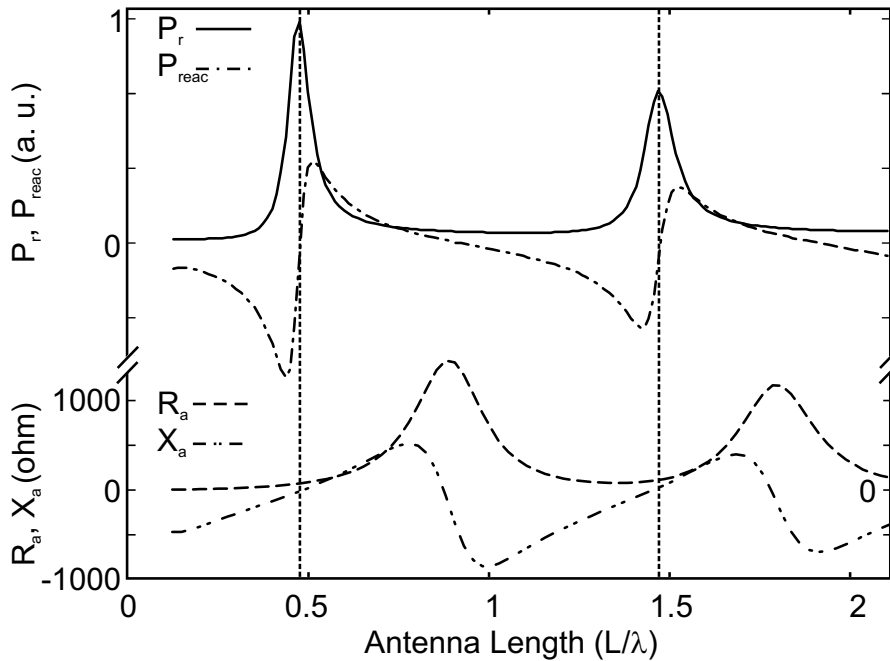


Figure 2.6.: Power transmitted for different dipole antenna lengths compared with the antenna impedance

radiation occurs close to $\lambda/2$ and $3/2\lambda$, at the position where P_{react} is zero and hence all power from the generator is converted to far-field radiation. This is also the position, where X_a goes through zero and hence current and voltage are in phase. For the antenna lengths $L \approx \lambda$ and $L \approx 2\lambda$, X_a and P_{react} are also zero, but now the high values of Z_a reduce I_g , which results in a low radiated power. We conclude that a antenna resonance occurs when the feed gap current density is high and in phase with the excitation voltage.

2.4.4. Receiving Properties

Starting point is similar to the derivation of Pocklington's integral equations. The incident external field generates a current density in the antenna arms, which results in a reradiated/scattered field. The electric field component parallel to the antenna is given by [39]

$$E_{\parallel}^{ex} = E_0 \sin \theta \exp(ikz \cos \theta) \quad , \quad (2.26)$$

where E_0 is the amplitude of the external field and θ the incident angle (see Fig. 2.3). Further was the reference phase of the incident field taken to be at the center of the antenna ($z = 0$). Assuming a perfect conductor the parallel component of the total electric field at the surface must vanish

$$E_{\parallel}^t = E_{\parallel}^{ex} + E_{\parallel}^s = 0 \quad \text{or} \quad E_{\parallel}^s = -E_{\parallel}^{ex} \quad . \quad (2.27)$$

The parallel field E_{\parallel}^s is compensating $-E_{\parallel}^{ex}$ on the antenna surface and induces a potential difference

$$V' = E_{\parallel}^{ex} dz = -E_0 \sin \theta \exp(ikz \cos \theta) dz \quad (2.28)$$

over each antenna element dz . V' drives a current in the antenna arm, which contributes to the current at the antenna feed-gap I_{sc} . The contribution of each voltage element to the feed-gap current is denoted as dI_{sc} .

According to the reciprocity theorem [39] the ratio between a voltage V_0 applied at the feed-gap divided by the current $I(z')$ generated in the antenna arm element dz' is equivalent to the ratio of the voltage V' applied along dz' divided by the resulting current dI_{sc} at the feed-gap. With V' given by (2.28) the reciprocity theorem yields

$$\frac{V_0}{I(z)} = \frac{-E_0 \sin \theta \exp(ikz \cos \theta) dz}{dI_{sc}} \quad , \quad (2.29)$$

which can be transformed to

$$I_{sc} = \frac{-E_0 \sin \theta}{V_0} \int_{-L/2}^{L/2} I(z) \exp(ikz \cos \theta) dz . \quad (2.30)$$

The current distribution $I(z)$ in (2.30) can be obtained from (2.22).

Representing the receiving antenna by a Thévenin equivalent circuit (see Fig. 2.5C) it is straight forward to calculate the power dissipated in the load and in the antenna. The time average power delivered to the load P_l respective to the antenna P_a is given by

$$P_{l,a} = \frac{1}{2} \left| \frac{V_{oc}}{Z_a + Z_l} \right|^2 Z_{l,a} = \frac{1}{2} |I_a|^2 Z_{l,a} . \quad (2.31)$$

Z_a of a receiving antenna is the same as for an transmitting antenna and is obtained from (2.23). The open circuit voltage (see Fig. 2.5C) writes as $V_{oc} = I_{sc} Z_a$, where I_{sc} is determined by (2.30). The dissipated average power P_a , results from ohmic and reradiation losses, represented by Z_a . In analogy to optics, the losses might be denoted as absorbtion and scattering. Neglecting ohmic losses, the real and imaginary part of P_a can be interpreted as average reradiated P_r and reactive power P_{reac} in a similar way as we have done for the transmitting DA and the infinitesimal dipole (see section 2.3).

For an antenna not connected to any external load it seems to be reasonable to consider the capacity of the gap as load impedance. Assuming that $a \ll \lambda$ the impedance should be similar to that of a plate capacitor even at high frequencies [46]. Hence the ideal capacity of a small gap ($d \ll a$) writes as $C_{gap} = 2\pi \varepsilon_c \varepsilon_0 a^2/d$, where d is the size of the gap, a the radius of the wire and ε_c and ε_0 are the permittivity of material inside the capacitor and of free space. The pure capacitive load impedance of the gap is then given by

$$Z_l = i\omega C_{gap} , \quad (2.32)$$

assuming infinite ohmic resistance of the gap.

With this model absolute values for P_a and P_l were computed for different antenna length (Fig. 2.7A). The antenna length L influences the antenna impedance Z_a and the open circuit voltage V_{oc} , both used for the calculation of $|P_a|$ and $|P_l|$ by (2.31). Maxima occur in $|P_a|$ for L close to $\lambda/2$, λ and $3/2\lambda$. The first ($L = \lambda/2$) and last ($L = 3/2\lambda$) maxima of $|P_a|$ are due to high antenna currents $I(z)$, increasing the value of I_{sc} (see Eq. 2.30) and hence also V_{oc} in (2.31). The center maximum of $|P_a|$ at $L \sim \lambda$ is due

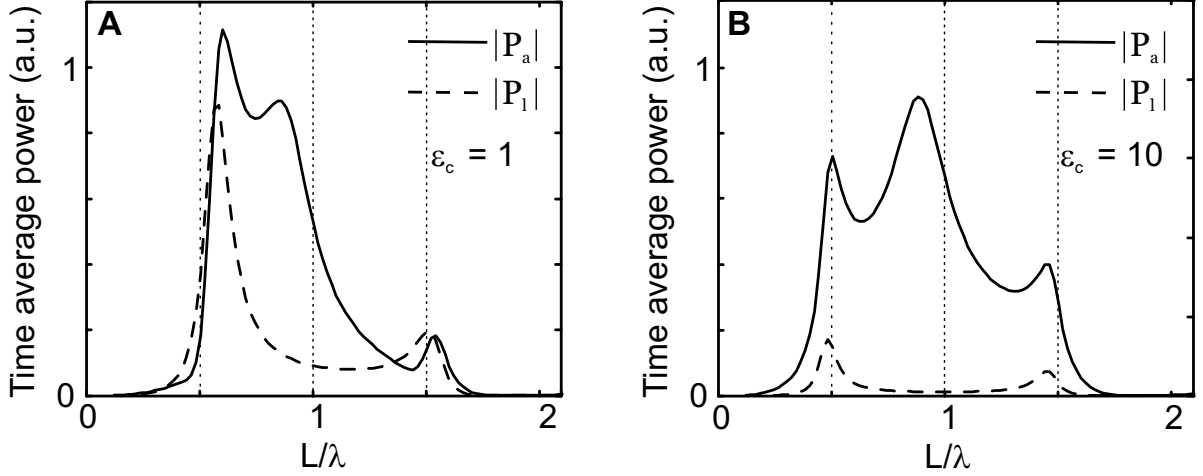


Figure 2.7.: Absolute power received $|P_l|$ and reradiated $|P_a|$ by dipole antenna, assuming a pure capacitive load of the gap, for different antenna lengths.

to a high value of Z_a , which is the result of a huge R_r at this length. As discussed we identified R_r to be responsible for the power radiated back from the antenna. The relative height of the three peaks of $|P_a|(L)$ depends on the ratio L/a , which affects the maximum values of R_r . For smaller values of L/a the absolute value of Z_a reduces (see Fig. 2.5A) and hence also radiation losses are diminished.

$|P_l|$ shows only maxima close to $L \sim \lambda/2$ and $L \sim 3/2\lambda$. At these lengths I_a reaches a maximum, which results in a maximum power dissipation in the load Z_l . This is comparable with the transmitting antenna, where the optimum antenna length is connected with a maximum current I_g at a length slightly smaller $\lambda/2$. The remarkable shift in the optimum antenna length between the analyzed receiving antenna and transmitting antenna is due the difference in used impedances. For the transmitting antenna Z_g was set to zero, whereas for the receiving DA, Z_a and Z_l both have appreciable values.

This brings us to another important aspect in antenna theory, the matching of the load (Z_g or Z_l) to the antenna impedance. For a receiving antenna optimum power transfer to the load is achieved under conjugate matching [37]: $Z_a = -Z_l$. For a transmitting antenna conjugate matching is achieved when $Z_a = -Z_g$. Fig. 2.8A, B shows the influence on the resonance for differently matched loads. A shift in resonance length and peak power is observed as the result of a change in ϵ_c from 1 to 10, corresponding to a capacitive load of $\sim 200i$ respective $\sim 20i$. That is, because Z_a (see Fig. 2.5A) matches better to $Z_l \sim 200i$ at $L > \lambda/2$ and to $Z_l \sim 20i$ at $L < \lambda/2$.

To estimate the field enhancement in the antenna gap, we followed again the model of an ideal plate capacitor. The field enhancement writes as: $EE^*/E_0E_0^*$, where $E = U/d = (I_a Z_l)/d$ is the field inside the capacitor and E_0 is the incident introduced by (2.26). Figure 2.8 shows the calculated field enhancement versus antenna length, for three different values of Z_l . Additional to changing ϵ_c , the gap distance was varied, which also effects Z_l . As expected from Fig. 2.7 the field enhancement increases and

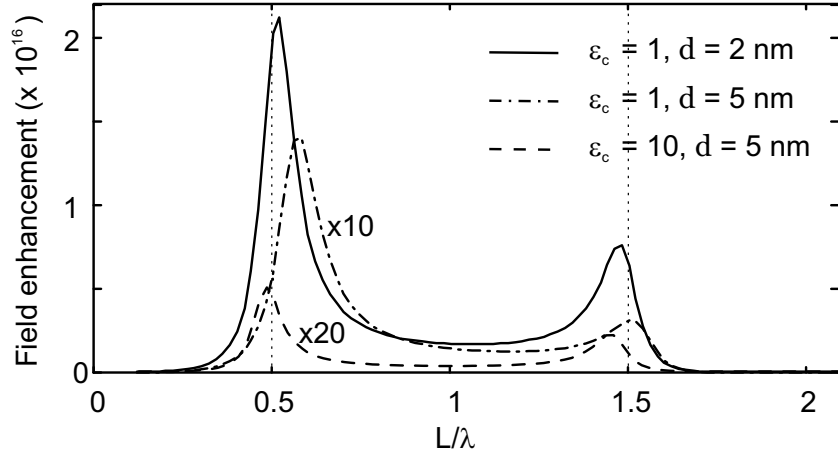


Figure 2.8.: Approximated field enhancement $EE^*/E_0E_0^*$ in an antenna feed-gap for three different values of Z_l .

shifts to larger L for a reduction of ϵ_c from 10 to 1. Reducing the gap distance leads to a further increase in EE^* , but with a shift back to shorter L , since a reduction in d is equivalent to an increase of ϵ_c . The high of the calculated field enhancement is tremendous and probably overestimated. Nevertheless electric fields inside an antenna feed-gap are known to be high and can be used to generate sparks between the antenna arms (corona effect).

2.5. Bow-tie Antenna

An other basic and simple designed antenna type is the bow-tie antenna. It consists of two opposing tip-to-tip metal triangles, separated by a small gap (see Fig. 2.9). Similar to a dipole antenna, the ratio between the physical length and the incident wavelength determines their impedance. Additional to the length L , the angle α (see Fig. 2.9) influences the antenna impedance and hence its resonance behavior. The impedance of a bow-tie antenna with large α can be denoted as broad-band impedance, which make

them useful for a larger frequency range [47]. For further antenna types, we refer to text books [37, 39].

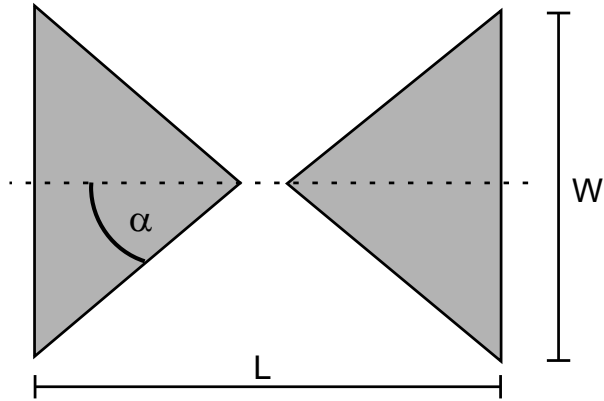


Figure 2.9.: Sketch of a bow-tie antenna

3. Optical Properties of Metals and Metal Particles

The great variety in how objects reflect, transmit or scatter visible light is a consequence of their different optical properties. There are two sets of quantities often used to describing the optical properties of materials: the complex refractive index $N = n' + in''$ and the complex dielectric function (permittivity) $\varepsilon = \varepsilon' + i\varepsilon''$. The two sets of quantities are not independent. They are related by $N^2 = \varepsilon$ and each quantity can be expressed by the real and imaginary part of the other [40]. Reflection and transmission at interfaces is described more simply by n' and n'' , while scattering and absorption by small particles is usually expressed by ε' and ε'' .

The frequency dependence of the optical properties is derived from the Lorentz model for a dielectric medium and the Drude-Sommerfeld model for conductors [40]. These microscopic models describe in a classical way the polarization of matter by an incident electrical field. In the Lorentz model a driven harmonic oscillator acts as a model for the electronic response of matter to an external electric field. The spring constant models a parabolic potential, defining the binding force acting on the electron by the positive core of the atom. The incident field leads to a displacement \mathbf{r}_0 of an electron which is associated with a dipole moment $\mathbf{p} = e\mathbf{r}_0$. The cumulative effect of dipoles result in a macroscopic polarization $\mathbf{P} = n\mathbf{p}$, where n is the number of electrons per unit volume.

To extend the validity of Maxwell's equations from vacuum to matter, so-called constitutive relations are added. The constitutive relation describing polarization \mathbf{P} of matter by an electric field \mathbf{E} writes $\mathbf{P} = \chi\varepsilon_0\mathbf{E}$, where the material depending electric susceptibility χ is given by the relation $\chi = 1 - \varepsilon$. Expressing \mathbf{P} by the microscopic polarization one finds

$$n\mathbf{r}_0 = (1 - \varepsilon)\varepsilon_0\mathbf{E} . \tag{3.1}$$

3.1. Drude-Sommerfeld Model

The model for the motion of a free electron in a conductor follows from the Lorenz model by 'clipping the spring', that is, by setting the spring constant equal to zero [40]. Therefore the equation of motion writes as

$$m_e \frac{\partial^2 \mathbf{r}}{\partial t^2} + m_e \Gamma \frac{\partial \mathbf{r}}{\partial t} = e \mathbf{E} e^{-i\omega t}, \quad (3.2)$$

where e and m_e are the charge and the effective mass of free electrons, and ω is the frequency of the incident electric field \mathbf{E} . The damping term is proportional to $\Gamma = v_F/l$ where v_F is the Fermi velocity and l is the electrons mean free path between scattering events. The solution to (3.2) is found by $\mathbf{r}(t) = \mathbf{r}_0 e^{-i\omega t}$ what gives the microscopic polarization $\mathbf{p} = e \mathbf{r}_0$. Together with (3.1) the 'Drude' dielectric function ε_d is given by:

$$\varepsilon_d = \varepsilon_b - \frac{\omega_p^2}{\omega^2 + \Gamma^2} + i \frac{\omega_p^2 \Gamma}{\omega(\omega^2 + \Gamma^2)} = \varepsilon'_d + i \varepsilon''_d \quad (3.3)$$

where $\omega_p = \sqrt{ne^2/m_e \varepsilon_0}$ is the volume plasma frequency and ε_b has the value of 1 when only conduction electrons are considered. To include the contribution of the bound electrons to the polarizability the value of ε_b has to be adapted [48]. The real and the imaginary parts of the dielectric function (see Eq. 3.3) are plotted in Fig. 3.1 together with experimental measured values [49]. Obviously the Drude-Sommerfeld model is quite

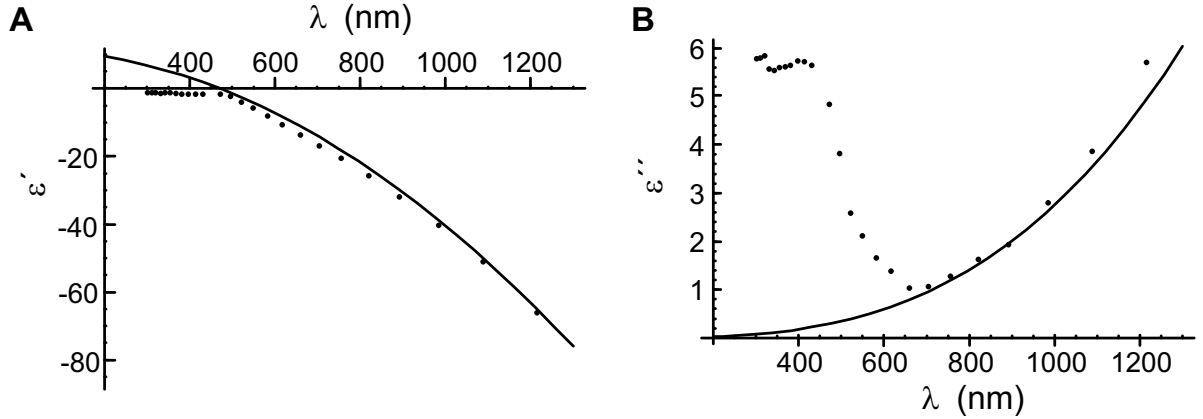


Figure 3.1.: Real (A) and imaginary (B) part of the dielectric function of gold. Dots: experimental data [49]. Line: Drude-Sommerfeld model taking into account contribution of bound electrons $\varepsilon_b = 9.8$, the plasma frequency $\omega_p = 13.8 \cdot 10^{15} s^{-1}$ and the damping term $\Gamma = 1.075 \cdot 10^{14} s^{-1}$.

accurate for gold in the infrared region, but it shows strong deviation in the visible. The

deviation occurs due to interband transitions, where photons with higher energies can excite electrons from deeper bands into the conduction band. In noble metals the transition electrons originate from the completely filled d-bands, which are relatively close to the Fermi-energy and allows for interband transition at optical frequencies. In a classical picture this contribution can be described by oscillation of bound electrons, that results in an even better fit between theory and measurement [1].

3.1.1. Skin Depth

The penetration of an e.m. field into matter is described by the imaginary part of N . The electric field is attenuated by the factor $e^{-\omega n'' z/c}$, where $c/(\omega n'')$ can be defined as skin depth. For $|\varepsilon'| \gg \varepsilon''$ the skin depth can be approximated by [50]:

$$\delta = \frac{c}{\omega n''} \approx \frac{c}{\omega \sqrt{|\varepsilon'|}} \quad (3.4)$$

Taking realistic values of $|\varepsilon'|$ for gold ($\varepsilon' = -25$, [49]) and aluminium ($\varepsilon' = -46$, [51]) at $\lambda = 800$ nm we find that the skin depth is about 25 nm for gold and 18 nm for aluminium. The assumption that metals are perfect conductors ($|\varepsilon'| \rightarrow \infty$) and that the field is restricted to the outside of the antenna is no longer valid at optical frequencies. The current inside the antenna body contribute to additional ohmic losses, which could affect the efficiency of an OA.

3.2. Localized Surface Plasmon Resonances

Localized surface plasmons (LSPs) are charge density oscillations confined to metallic nanoparticles and metallic nanostructures [50]. Excitation of a LSP resonance (LSPR) results in strong light scattering, in the appearance of strong surface plasmon absorption bands and an enhancement of the local e.m. field. The spectral position of the LSPR is highly sensitive to the structural geometry and material of the nanostructure as well as to the surrounding environment. A review about the exploitation of LSPR for various applications is given in [52].

LSPR of spherical particles can be theoretically described by Mie-Theory (by G. Mie published in 1908), which provides exact solution to Maxwell equation for scattering of a

plain wave by a sphere with arbitrary radius and isotropic dielectric properties embedded in a homogeneous medium. Results from Mie-Theory obtained for scattering of small spheres can equivalently be described by a quasi-static approximation [40] also known as Rayleigh Theory (Lord Rayleigh published in 1871). The following shortly summarizes the results of the quasi-static approximation for spherical and elliptical particles. For a detailed description we refer to text books [40, 50].

3.2.1. Plasmon Resonances of Spherical Particles

For particles much smaller than the wavelength, it turns out that the scattered fields can be approximated by the fields of a radiating dipole. The physical interpretation is that the particle is polarized by the incoming wave, since it is quasi stationary over the dimension of the particle (Figs. 3.2A, B). The dipole moment of a sphere with radius $a \ll \lambda$ and dielectric constant ε_1 embedded in a medium with dielectric constant ε_m is given by [40]:

$$\mathbf{p} = 4\pi\varepsilon_m a^3 \frac{\varepsilon_1 - \varepsilon_m}{\varepsilon_1 + 2\varepsilon_m} \mathbf{E}_0 = \varepsilon_m \alpha \mathbf{E}_0 \quad , \quad (3.5)$$

where \mathbf{E}_0 is the static electric field inside the medium, without any particle. Note that the field inside the particle is assumed to be uniform in the electrostatic approximation. This is fairly true when the skin depth is larger than the particle diameter. The dipole moment oscillates with the frequency of the applied field; therefore the dipole produces an e.m. field that radiates (i.e. scatters). The radiated/scattered field depends in magnitude on the dipole moment and hence on the polarizability

$$\alpha = 4\pi a^3 \frac{\varepsilon_1 - \varepsilon_m}{\varepsilon_1 + 2\varepsilon_m} \quad , \quad (3.6)$$

that becomes obvious by looking at the scattering cross section, that writes as [40] $C_{sca} = \frac{k^4}{6\pi} |\alpha|^2$. A resonance in the polarizability leads to strong scattering, referred to as LSPR and interpreted as a collective oscillation of the free electrons in the particle. A LSPR occurs for minimal values of the denominator in (3.6) which is given by $|\varepsilon_1 + 2\varepsilon_m| = \sqrt{(\varepsilon_1' + 2\varepsilon_m)^2 + (\varepsilon_1'')^2}$, when the dielectric constant of the surrounding medium is assumed to be real. Scattering experiments in the visible regime show that the electrostatic approximation holds for particles with radius < 20 nm. The plasmon resonances of gold colloids in water and oil is indicated in Fig. 3.2C. The shift in resonance wavelength is influenced by the surrounding medium and the optical properties

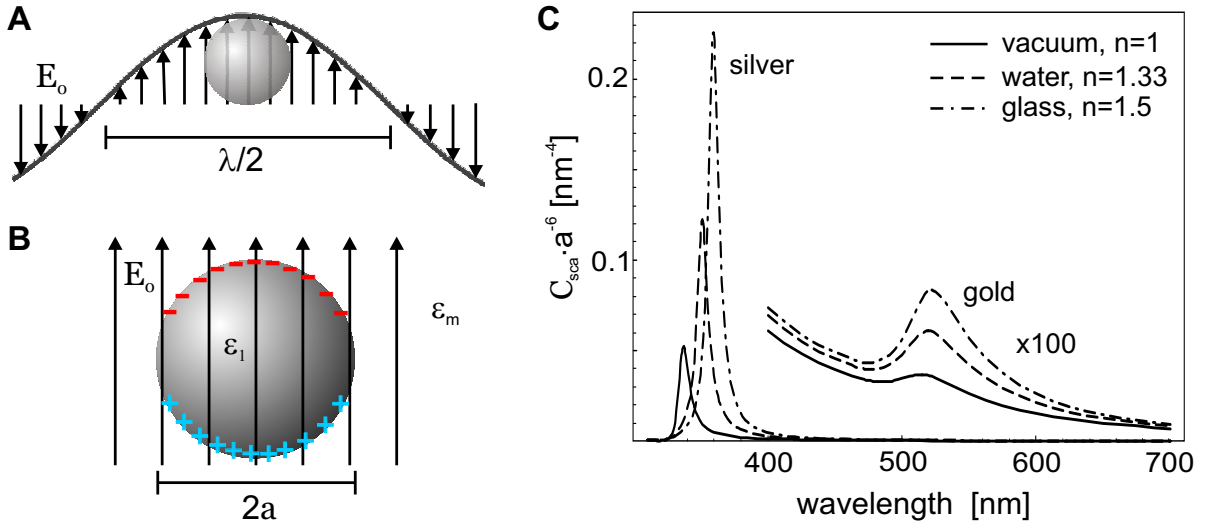


Figure 3.2.: Scattering by a sphere in the electrostatic approximation. (A) Incident field E_0 and particle. (B) Electrostatic approximation. (C) Scattering cross-section of spherical gold and silver particles ($a = 20$ nm) in different environments normalized by the particle radius (from [1])

of the sphere material.

Since the particle is point like the scattered fields are obtained from the vector potential \mathbf{A} given by Eq. (2.12). The integral over the source current density can be related by means of the continuity equation to the induced dipole moment [41], that writes as

$$\int_V \mathbf{J}(\mathbf{x}') d\mathbf{x}' = i\omega \int_V \mathbf{x}' \rho(x') d\mathbf{x}' = i\omega \mathbf{p}. \quad (3.7)$$

Comparing (3.7) with the integral over the current density of the infinitesimal dipole antenna (2.13), one finds: $i\omega \mathbf{p} = I_0 l \mathbf{e}_z$. Therefore, scattering by small particles can be viewed as being either dependent on the induced dipole moment \mathbf{p} , or equivalent, by a induced current I_0 in direction of the incident field. In the optical regime the magnitude of the current strongly depends on the dielectric function and shape of the particle. When exciting a LSPR the polarization/current reaches a maximum value. Since high antenna currents are a precondition for good antenna performance the excitation of LSPR could enhance antenna performance at optical frequencies.

3.2.2. Plasmon Resonances of Elliptical Particles

Since dipole antennas are closer in shape to elliptical particles as to spheres, it is of interest to look for the plasmon resonances of elliptical particles. Unlike to spheroids their resonances are in addition to the dielectric function influenced by the shape. The quasi-static approximation for spheres can be expanded to spheroids by introducing a shape factor. The polarizability of a elliptical particle (see Fig. 3.3A) with the incident field along its long axis a is given by [40]:

$$\alpha = 4\pi abc \frac{\varepsilon_1 - \varepsilon_m}{3L_s(\varepsilon_1 - \varepsilon_m) + 3\varepsilon_m} \quad (3.8)$$

where L_s is a shape factor influenced by the eccentricity e . For a prolate spheroid ($b = c$) L_s is defined as:

$$L_s = \frac{1 - e^2}{e^2} \left(\frac{1}{2e} \ln \frac{1+e}{1-e} - 1 \right); \quad e^2 = 1 - \frac{b^2}{a^2} \quad (3.9)$$

For gold nanorods embedded in a homogenous medium (index matching fluid: $\varepsilon_m = 2.25$) with length up to 150 nm and diameter of ~ 25 nm the simple quasi static calculation of long-axis plasmon resonances is in good agreement with experimental data [53].

The structures investigated in this work are in length and width about 2 times bigger

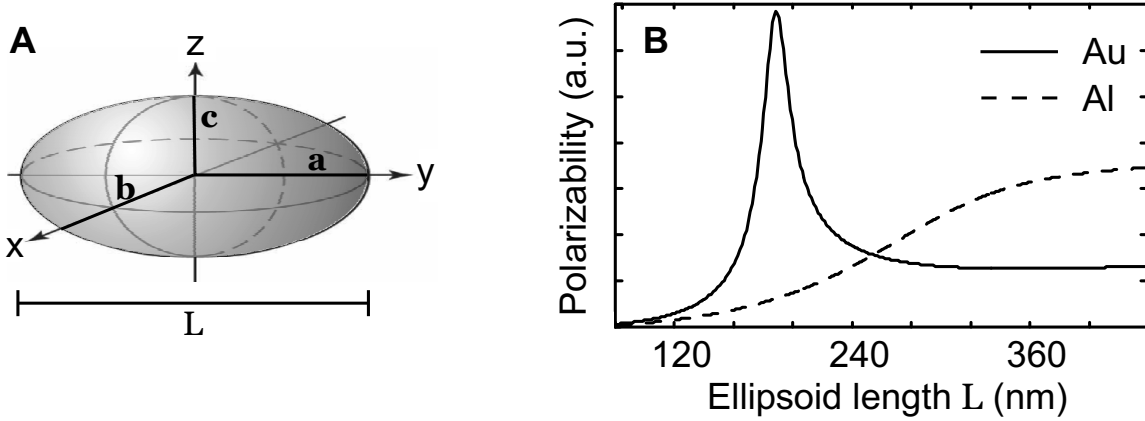


Figure 3.3.: Polarizability of an ellipsoid in the electrostatic approximation (A): Ellipsoid with semiaxis a, b, c (B): Long-axis polarizability of a gold (Au) and an aluminum (Al) ellipsoid ($b = c = 20$ nm) versus total length $L = 2a$. The calculation was performed with the program plasmon.m (see appendix B.1.2)

as the nanorods analyzed in [53]. This limits the validity of a static calculation in our case. Figure 3.3B shows the calculated long-axis polarizability (see Eq. 3.8) of

a gold and a aluminium ellipsoid ($c = b = 20$ nm) versus their total length. The dielectric constant of gold ($\varepsilon_{Au} \approx -25 + i \cdot 1.6$) and aluminum ($\varepsilon_{Al} \approx -46 + i \cdot 29$) were chosen for a fixed incident wavelength (830 nm). To account for the glass-air interface the surrounding medium was chosen with an intermediate dielectric constant $\varepsilon_{glass/vacuum} = 3.25/2$ between glass and vacuum.

The gold ellipsoid shows a peak in polarizability at a length of about 180 nm, which is related to a surface plasmon resonance. By increasing the dielectric constant of the surrounding this resonance can be shifted to shorter ellipsoid lengths. For the aluminum ellipsoid, it is apparent that there is no resonance. Even when we reduced the diameter in the calculation by a factor of 10, no resonance was observed. From this we conclude that no surface plasmons can be excited in aluminum particles with a diameter > 2 nm in a common dielectric surrounding at infrared frequencies.

4. Antennas at Optical Frequencies

It is difficult to predict how the antenna characteristics (e.g. resonance length) are influenced, when an antenna is scaled to the optical regime. From the previous chapters we gained some insight into classical antenna theory and the optical properties of metals. This helps us now to appreciate in which respect the physical properties of an optical antenna (OA) differs from that of radio wave antenna.

At optical frequencies metals are no longer perfect conductors and the assumption made by classical antenna theory, that e.m. fields are restricted to the outside of an antenna is no longer valid. Depending on the permittivity of the antenna material the fields penetrate the surface in an extent given by the skin depth. At optical frequencies the skin depth for many metals is quite large and is, even for thick antennas, comparable with the antenna diameter. Seeing the antenna as e.m. boundary problem, the large skin depth at optical frequencies increases the complexity of the problem. The solution given by classical antenna theory are no longer fully applicable. The current distribution and hence the antenna input impedance of optical antennas will differ to some degree from the predictions made by classical antenna theory. This will affect the resonance length as well as the achievable field enhancement in the feed gap of an OA.

A strong influence on the input impedance of OA is also expected due to the existence of localized surface plasmon resonances, which for noble metals occur at optical frequencies (see Figs. 3.3). A LSPR can be interpreted as either a strong polarization of the particle or as a huge increase of the current density inside the particle. Provided that a LSPR increases mainly the current amplitude and causes only minor changes of the current distribution and phase, it could greatly enhance OA performance. On the other hand also metals that do not support LSPRs should still show an antenna resonance.

Deviation of the current density in an OA compared to that of an classical antenna

is not only expected due to the difference in material properties. Also constrains in nano-fabrication influence the function of an OA. For instance the feed-gap size is a critical parameter. We used the delta-gap source model of classical antenna theory to calculate the current density of an antenna. This model has to be modified when the lithographically produced feed-gap is no longer small compared to the antenna length. Further we suspect, that grain-boundaries and surface roughness have effects on the current flow inside OA.

To predict in more detail the function of an OA one has to perform computer simulations, that take into account the antenna shape and the finite and frequency dependant permittivity of the antenna material. Two methods were used to support the interpretation of the experimental data. The first method is based on a Green's tensor approach [54]. Simulations with this method were performed by O. J. F. Martin from the EPFL. For further simulations, we also used a commercial software (LUMERICAL), based on the finite-difference time-domain (FDTD) method [55]. Both methods were used to calculate the e.m. field components and field intensities around the antenna structure and in the feed gap. The methods require, that at least the structure itself is discretized in a computational grid. The grid size ($dx, dy, dz < \lambda/(50 \cdot n)$) must be small compared to the wavelength and smaller than the smallest feature in the computation volume. Structures with very fine details, require a larger computational domain, that result in much longer solution times. In that respect the Green's tensor approach is favorable, since only the antenna structure has to be discretized, and not the dielectric background. Nevertheless computer simulations are also limited in accuracy. The finite grid size could introduce numerical errors into the solution, leading to artifacts in the calculated field distribution [56]. Numerical simulations are further limited, since they hardly can take into account for the exact structural shape, the surface roughness and grain-boundaries existing in real OAs. Experimental investigation is needed to learn more about the properties of OA, and how they are effected by real structural defects.

Part II.
Experimental

5. Sample Preparation

Precise structuring of metals in the nm-regime is a non trivial task, especially for gold which has a high mobility at room temperature and tends to form clusters. The requirements for one of the simplest antenna structures (dipole antenna) are smooth lines well below 100 nm in width and feed gap sizes in the range of 10 nm. Only a few lithographic methods based on electron beam (e-beam) [25, 57, 58], focused ion beam (FIB) [59–62] and atomic force microscopy (AFM) [63–65] are able to generate sub 100 nm metal lines. E-beam lithography is by far the most used and flexible. It is established for a long time in semiconductor industry. For the optical investigations of antenna structures it is advantageous to produce them on a transparent (e.g. glass) substrates. However e-beam lithography, FIB milling and scanning electron microscopy (SEM) characterization requires a conductive sample. Therefore the glass substrate has to be coated with a thin layer of a transparent and conductive material. A natural choice for the coating material is indium tin oxide (ITO) [25].

This chapter describes the fabrication of OA by means of e-beam lithography and a combined method based on e-beam lithography and FIB milling. For both approaches ITO coated glass was used as substrate. Finally a short report is given on the modification of gold nanorods by FIB, which is a promising approach for OA preparation. For the later study thermal oxidized titanium was used to achieve conductivity of the substrate.

5.1. E-Beam Lithography

A lithographic mask is produced by means of a focused e-beam in an electron sensitive resist (e.g. PMMA) which covers the substrate. In an SEM prepared for lithography tasks, the e-beam is controlled by the pattern generation software and is scanned in a controlled way over the sample. Where the e-beam hits the resist the polymer chains break (for positive resist) and can be dissolved with a developer. The remaining resist

can then be used as a mask for the metallization in an evaporation chamber. In a last step the resist is dissolved, which removes all deposited material except at the areas exposed to e-beam. A detailed description of this so call lift-off technique is given in [66].

The e-beam lithography facilities were available in the Institute of Physics at the University of Basel in the group of Ch. Schönenberger. A Jeol JSM-IC848 SEM controlled by the ELPHY Quantum (Raith GmbH) pattern generation software was employed. The substrate was a 1 mm thick glass coated with a 100 nm thick layer of ITO, kindly provided by Unaxis. A positive resist in a solution of 6% solids (1:3, Chloroform:Alresist 950 K [AR-P 671.09]) was spin coated for 45 s at 4000 rpm. The achieved layer thickness after backing the resist at 170°C for 30 min was about 600 nm. After e-beam exposure, the sample was dipped into the developer (1:3, Metyle-2-pentatone isoButylmetylKeton:2-isopropanol) for 45 s and rinsed with 2-isopropanol after. Metal deposition was done in an e-beam evaporation chamber at a rate of ~ 3 nm/s. The lift-off was done in acetone.

First simple dipole structures were prepared, consisting out of two lines separated by a small gap. The pattern generation software was used to vary the gap width, length and exposer dose for the structure. A result of dose reduction is a reduced length and width of the structure. By changing the e-beam dose in a row of equal dimensioned structures it was possible to produce small gaps in the range of a few 10 nm (see Fig. 5.1). The limiting factor was the line width of the structures. Short lines were usually in width of ~ 100 nm. A thinner line width of about 80 nm was only achieved for longer lines (> 500 nm). In principle, the limitation in width is due to backscattered electrons from the substrate, which reduces the resolution. By applying a two-layer electron-sensitive resist, backscattering is minimized and a reduction of the line width to the sub 50 nm regime should be possible [57, 58]. Practically, the condition of the e-beam facility and the experience of the user have influence on the achievable line width. The double layer method was already applied with the given e-beam facility and a minimum line width of ~ 90 nm was reported [66].

The limitation in line width and the structural detail achieved with the used e-beam lithography facility is obvious not sufficient for the production of high-definition optical antennas. A nano-fabrication method where a line width of ~ 50 nm is direct achievable was preferable, witch led us to FIB structuring.

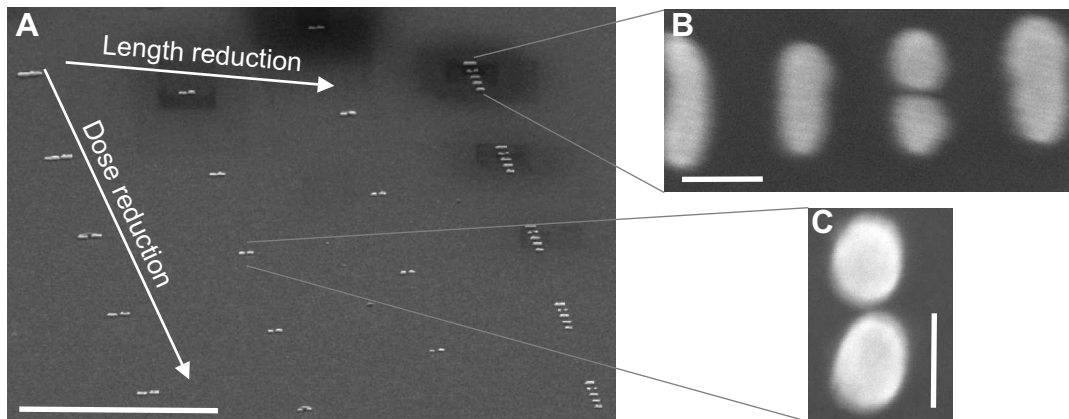


Figure 5.1.: Antenna structure produced by e-beam lithography on ITO substrate. (A) SEM image of the structured array, scale bar $5 \mu\text{m}$. (B) Yggi Uda like antenna structure. (C) Dipole structure (scale bar in B and C 200 nm)

5.2. Focused Ion Beam Structuring

Focused ion beam (FIB) technology can be used for nano-structuring in many different ways: Lithography, removal and chemical vapor deposition in the sub 100 nm range was reported [59, 60]. Furthermore metal-organic cluster complexes can be used for high-resolution 3D patterning [61, 62].

We chose to use the basic capability of the FIB to remove material. Material is removed, where the focus of the ion beam hits the sample. By using small ion currents a focus size in the sub 10 nm is achievable. But the resolution is not only given by the focus size. The minimum line width depends also on the depth of the milled line [67]. This limits, for example the achievable line width of a 60 nm deep line to about 30 nm [67]. The drawback of a low ion currents are low milling rates, that make material removal time consuming and hence very expensive. This was compensated by a pre structuring with e-beam lithography (see section 5.1), minimizing the amount of material removed during FIB milling.

FIB structuring of optical antennas was performed with a dual beam FIB (FEI 235, EMPA Dübendorf). It consists of a combination of FIB and SEM in one machine. This powerful tool offers the possibility to image a sample in the SEM-mode without damaging the sample surface by ions. Subsequent modification of a desired position on the sample can be achieved in FIB-mode by ion beam removal of material. This ability of the dual beam FIB made a pre structuring of the substrate with another lithographic

method feasible.

In a first step, an array of gold patches surrounded by a large finding structure was prepared by e-beam lithography (Fig. 5.2). As a substrate, a ITO-coated glass-cover

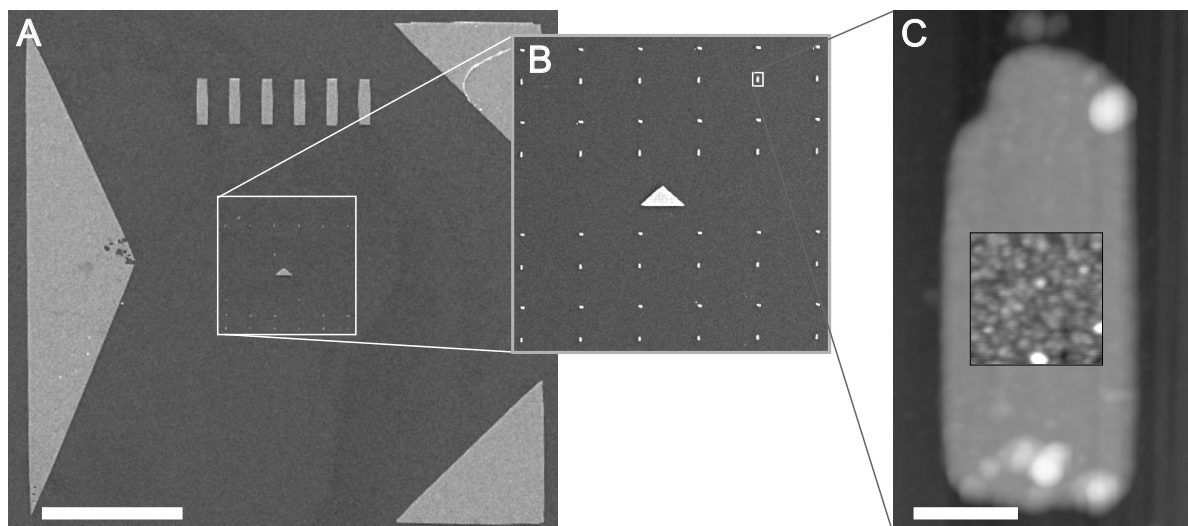


Figure 5.2.: (A) SEM-image of gold patch array and triangular finding structures. (B) Zoom ($50 \times 50 \mu\text{m}^2$) on patch array. (C) AFM-image of one gold patch ($400 \times 800 \times 40 \text{ nm}^3$) before FIB modification. Inset shows high resolution AFM-image ($250 \times 250 \text{ nm}^2$) used for surface roughness measurement.

slide (10-20 nm ITO on ~ 0.17 mm thick glass, kindly provided by the group of Prof. Oelhafen, University Basel) was used. To get an idea of the achievable gold film quality, we measured exemplarily the surface roughness (1.0 nm RMS) by AFM, in the center of a patch (Fig. 5.2D). The measured patch height was ~ 40 nm. The roughness and quality of the patches was checked again in the SEM-Mode, at 10 kV and 80000 magnification, immediately before FIB structuring. Only patches showing a smooth surface in the SEM image, comparable with the patch checked by AFM, were chosen for FIB structuring (like in Fig. 5.3A).

Focusing and alignment of i- and e-beam were performed on the large triangular finding structure shown in Fig. 5.2A on the left side. In a ideal case of a perfect alignment of i- and e-beam on the same focal spot, the milling pattern can be positioned in respect to the SEM-image. A small drift of the e-beam focus relative to the i-beam focus, made it necessary to take an i-beam image first. The position of the milling patterns (white boxes 1-5 in Fig. 5.3A) was then placed in respect to the taken i-beam image and was milled out sequently by the FIB. An illustration of the structuring process and the results

are shown in Fig. 5.3. To prevent material deposition in the antenna gap (~ 20 nm)

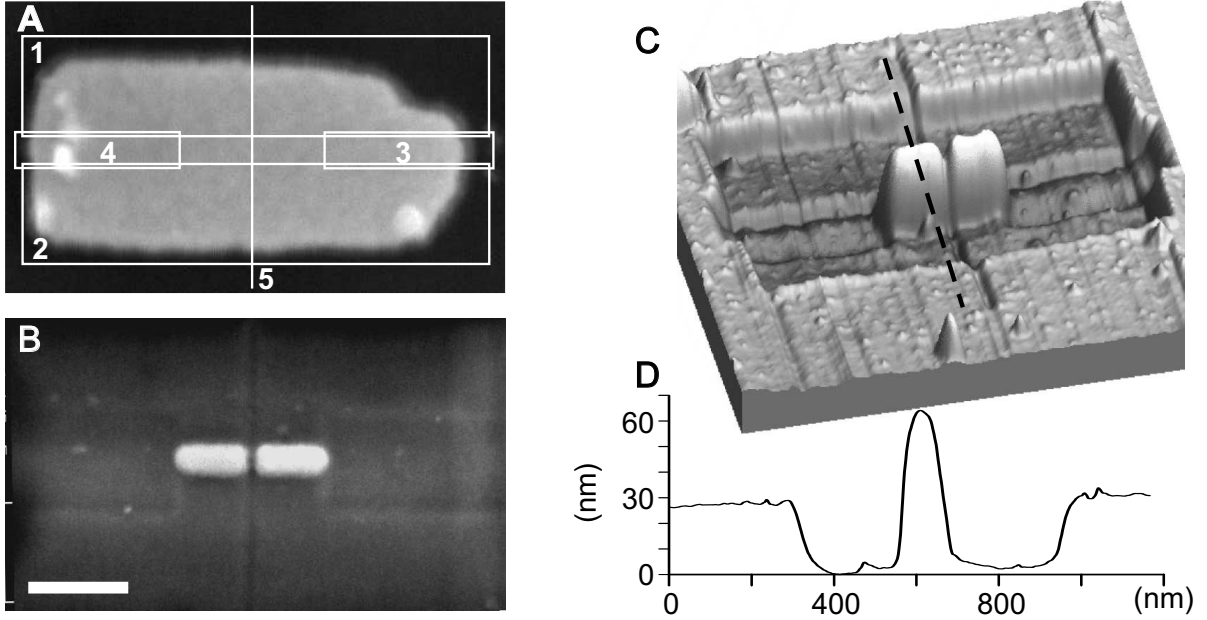


Figure 5.3.: FIB assisted antenna fabrication. (A) SEM-image of gold patch. Pattern 1-5 (white boxes) were removed subsequently by the ion-beam with following structuring parameters: I-beam acceleration voltage: 30 kV, i-beam current: 1 pA, magnification: $\times 80000$, material file: Si-small, milling depth: $z = 0.04 \mu\text{m}$ for pattern 1-4, $z = 0.06 \mu\text{m}$ for pattern 5. (B) Resulting antenna structure. (C) 3D AFM-image, dashed line is indicating position of line profile shown in (D).

pattern 5 was structured last. For complete gold removal, the FIB had to cut slightly into the substrate, leaving a shallow depression ($\sim 20 - 30$ nm) around the structure, clearly visible with the AFM (Fig. 5.3C and D). The AFM image reveals also a reduction (> 5 nm) of height of the antenna structure, compared to the original film thickness. This is partly due to the i-beam imaging, which was performed for pattern positioning, before FIB structuring.

The main advantages of FIB structuring are the relatively sharp edges of the structure and the good reproducibility. Immediate structural shape control allows for fast optimization of the milling pattern. Drawbacks are the implantation of ions (here gallium) into the metal film that could cause minor changes to the dielectric constant and conductivity. FIB milling of gold films results in a rough surface with sometimes a few gold grains in the surrounding of the structure. The removed material deposits in a

uncontrolled way on the sample, which requires to keep some distance between different structures.

5.3. Nanorod Modification by FIB

Another promising approach for OA fabrication was to modify gold nanorods by cutting them by FIB to the desired dimension. The rods were grown in a seed-mediated process in solution [68], by the group of Prof. C. J. Murphy at the University of South Carolina. The diameter of the rods was ~ 25 nm and the maximum length was close to 600 nm. The nanorod solution was diluted with ethanol and spun onto the substrate. The substrate was glass (0.17 mm) covered with a 3-4 nm thick titanium layer, thermal oxidized at 150-200 °C, resulting in a slightly conducting and transparent TiO_x film. UV-lithography was used to generate a finding structure on the sample (Fig. 5.4A). This enabled characterization and selection of single rods in the right dimension with a conventional SEM before FIB modification.

The superior quality of the rods is illustrated in Fig. 5.4B, showing a gold nanorod next to a gold structure produced by e-beam lithography. The surface is smooth and no grain boundaries are visible. Diffraction analysis and high resolution transmission electron microscopy of mature nanorods showed superpositions of two specific pairs of crystallographic zones, either $\langle 112 \rangle$ and $\langle 100 \rangle$ or $\langle 110 \rangle$ and $\langle 111 \rangle$, which were consistent with a cyclic penta-twinned crystal with five $\{111\}$ twin boundaries arranged radially to the $[110]$ direction of elongation (see ref. [69]). In contrast to the evaporated structure there are no grain boundaries perpendicular to the rod long axis. This crystallographic properties results in reduced plasmon damping and reduction of non-radiative losses [53], which is expected to be of great advantage for OA efficiency.

The transformation of a nanorod into an OA was done in the following way: The rod was chosen in SEM-mode, then one low current i-beam image in FIB-mode was taken. This image was used to place the pattern 1-3 for ion milling (see Fig. 5.4C). After ion milling a shallow depressions (~ 20 nm) is left on both sides of the OA arms. The arms are separated by a 10-20 nm-wide gap in the center (Fig. 5.4D). In the scope of this work, it was only possible to produce a few antennas from nanorods. Therefore a systematic optical investigation of nanorod antennas with different length was not

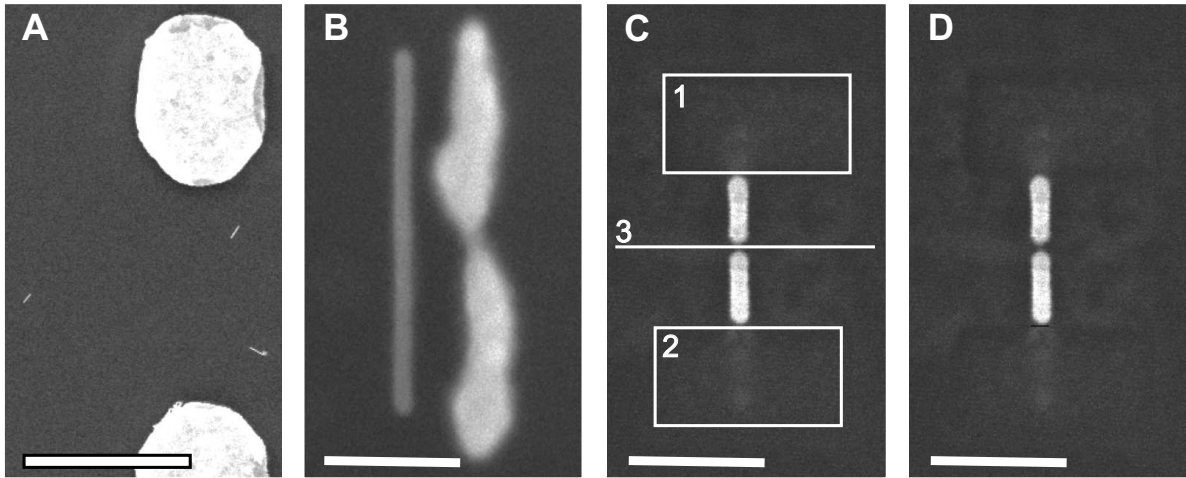


Figure 5.4.: SEM-images of nanorod sample.(A) Orientation markers and single gold nanorods, scale bar $5 \mu\text{m}$. (B) Comparison between grown nanorod with rod produced by e-beam lithography. (C) Nanorod with indicated FIB milling pattern 1-3 (milling parameters: I-beam acceleration voltage: 30 kV, i-beam current: 2 pA, magnification: $\times 100000$, material file: Si-small, milling depth: $z = 0.02 \mu\text{m}$ for box 1-3). (D) OA after FIB milling. (B)-(D) Scale bar 200 nm

possible. It was found in agreement with the measurements discussed in chapter 7, that white light emission is much more efficient generated by a nanorod antenna as by a nanorod of equal length.

6. Microscopy Techniques

A further experimental challenge was to prove field-confinement and enhancement in the feed gap of OA structures. The dimensions of the feed gap are far below the diffraction limit, and hence only directly accessible by near-field microscopy techniques [1], that reach resolution limits on the order of $\lambda/20$ [2]. The implementation of a scanning tunnelling optical microscope (STOM) was aimed at the direct detection of the optical near-field distribution around OAs. Furthermore a scanning confocal optical microscope (SCOM) was built. It was designed to exploit nonlinear effects to detect in an indirect way the field enhancement induced by resonant OAs.

The implementation of the experimental setups (STOM and SCOM) and the programming of the data acquisition, was a major part of this thesis. This chapter describes the principles and designs of the two setups used for OA studies.

6.1. Scanning Tunnelling Optical Microscopy

The scanning tunnelling optical microscope (STOM), also called photon scanning tunnelling microscope (PSTM), combines far-field illumination with near-field detection. The sample is illuminated such that the illumination beam undergoes total internal reflection on the sample-air interface. This is achieved by using a prism or a high numerical aperture (NA) objective [70]. The resulting evanescent surface wave decays exponentially along the surface normal. The decay length is on the order of 100 nm [71]. A bare or metallized tapered glass fiber is dipped into the evanescent field to locally couple near-field light into the fiber where it is converted into propagating modes that are guided towards a detector.

The detection of the evanescent field at each surface position allows in ideal cases (e.g. weakly scattering samples) the reconstruction of the optical near-field distribution in

a given height above the sample surface. In general the interpretation of the detected STOM images is a crucial and difficult problem. In principle multiple scattering between the sample and the tip has to be taken into account. Neglecting multiple scattering, it is possible to describe the detection process by a convolution of the undisturbed near-field intensity with a function accounting for the tip shape. Some theoretical efforts exist that try to recover the exact shape of the imaged structure by mathematical inverse scattering and deconvolution of measured data and tip shape [72].

Near-field measurements performed with aperture probes in constant gap mode have the risk of artifacts induced by topography [73]. Topography artifacts are reduced for pure dielectric probes. In addition dielectric probes have the advantage that the field distribution is much less disturbed by a dielectric than by metallized tip. On the other hand, the spatial confinement of the collection area for a dielectric tip is neither very small nor well defined. Therefore dielectric probes can introduce severe artifacts in the imaging process of strongly scattering samples. These artifacts originate from the fact that fields are most efficiently coupled into the fiber along the tip shaft and not at the tip end [1]. Since the tip is no point-like scatterer the collection efficiency can depend in a complicated way on the specific three-dimensional structure of the tip and on the polarization of the incident light. Nevertheless, for weakly scattering samples, STOM with bare and metalized tapered fibers has been successfully applied in the study of surface plasmon waveguides [74–76], integrated optical waveguides [77–79] and low dimensional semiconductor structures [80] where the near-field distribution close to the interface is of interest. Several groups have reported optical resolution below 100 nm, even with bare fibers [74, 81, 82].

6.1.1. Description of the Experimental Setup

The STOM used for antenna investigation (Fig. 6.1) was build up on top of an inverted microscope (Zeiss Axiovert). The whole setup was placed on a vibration damped table and covered by a box to shield air flow and background light. The illumination wavelength could be varied. This was realized by three semiconductor cw laser diodes (output power: ~ 10 mW, λ : 532 nm, 675 nm, 830 nm), coupled into the fiber used for illumination. The polarization direction of the illumination beam was adjusted by a combination of a fiber polarization controller and a polarizer. The light exiting the fiber

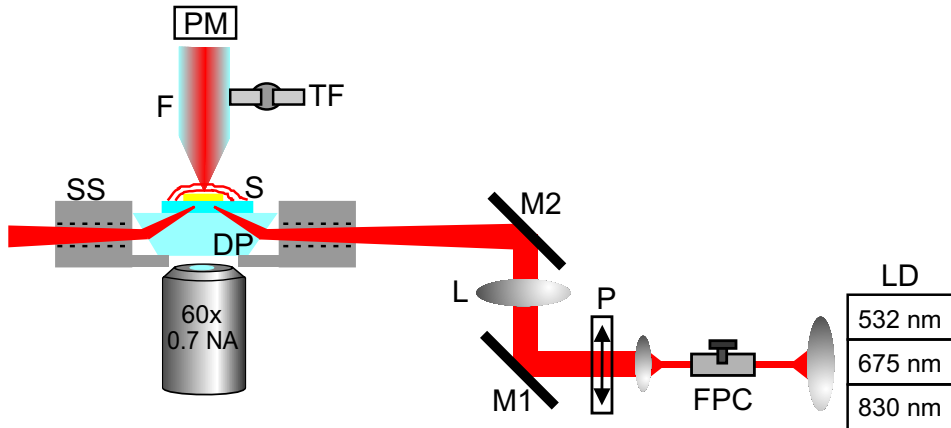


Figure 6.1.: STOM setup used for antenna investigation. SS: regulated x-y scan stage. F: tapered glass fiber. PM: photo multiplier, DP: dove prism, S: sample, TF: tuning fork, M1,M2: mirrors, L: focusing lens P: polarizer, FPC: fiber polarization controller, LD: laser diode array

was collimated and focused by a lens ($f = 400$ mm) into a dove prism, to which the sample was connected with index matching fluid. The prism was incorporated in a plate mounted onto a regulated piezoelectric x-y scan stage (Physik Instrumente, P-733). The angle of incidence was adjustable in a narrow range ($72 \pm 5^\circ$) by a mirror (e.g. M1 in Fig. 6.1). This allowed for overlapping of the resulting elliptical illumination area (semi axis: $a \sim 50 \mu\text{m}$, $b \sim 15 \mu\text{m}$) with a structure of interest. An objective underneath the prism was used to monitor the process of overlapping and positioning of the tapered fiber probe above the structure. The far end of the glass fiber holding the fiber probe was connected to a photomultiplier tube. Scan images were acquired by either scanning the fiber probe (with a tube piezo, see appendix A.1) or the sample. The output voltage of the photomultiplier tube was recorded for each sample/tip position for a given time, depending on the scan speed. The probe-sample distance (~ 10 nm) was controlled by means of a quartz tuning-fork attached to a fiber probe acting as piezoelectric shear-force sensor. A new glue-free design of the shear-force microscope scan head is described in appendix A.

6.2. Confocal Optical Microscopy

Confocal optical microscopy is a far-field technique and hence limited in resolution by diffraction. Nevertheless the high optical fields in the focus of a confocal microscope can

be exploited to excite nonlinear processes in materials, leading to wavelength shifted light emission. The strength of emission and order of nonlinearity can be used as a measure for the field enhancement at the position of the structure. A well known nonlinear process, is the two-photon excited photoluminescence (TPPL) observed at rough metal surfaces [26, 29, 30] and single metal particles [30]. Local field enhancement has been found to be a prerequisite for efficient TPPL generation. Confocal optical microscopy with a pulsed excitation source was successfully applied to generate and detect TPPL [30].

6.2.1. Principles of Confocal Microscopy

Confocal optical microscopy was invented by Marvin Minsky in the 50ths [83]. One possible realization of a confocal microscope is depicted in Fig. 6.2. In a confocal optical microscope (COM) the focal detection area overlaps with the focal excitation spot in the object. A beamsplitter separates the excitation path from the detection path. Light scattered from the focal excitation area is collected by the same objective and is focused by a lens onto the image plane, where the detector is positioned. Resolution and contrast in a COM is gained by a spatially confined excitation and by spacial filtering (e.g. with a pinhole) in the detection path. Only objects on the optical axis and in the conjugated image plane are focused onto a pinhole and hence reach the detector without attenuation. Light coming from laterally displaced positions is blocked by the pinhole and is not detected. The imaging properties of a microscope can be specified by its point spread function (PSF) [1, 84]. As the name implies, the point-spread function defines the spread of a point source by the imaging process. The total point spread function of a microscope can be regarded as the product of the excitation-PSF and the detection-PSF, $PSF_{total} = PSF_{excitation} \cdot PSF_{detection}$. The resolution of a microscope can be defined by the full width at half maximum (FWHM) of the total point spread function.

In wide-field microscopy the excitation is not localized and can be described by a plain wave. Therefore the FWHM of the total-PSF is basically the FWHM of the detection-PSF. For a point-source, like a fluorescing molecule, the detection-PSF is given by an Airy-pattern, representing the intensity distribution on the detector. Resolution in a wide-field microscopy can be defined by $FWHM_w = 0.51 \frac{\lambda}{NA}$, which is the FWHM of the Airy-pattern. NA is the numerical aperture of the objective and λ the wavelength used

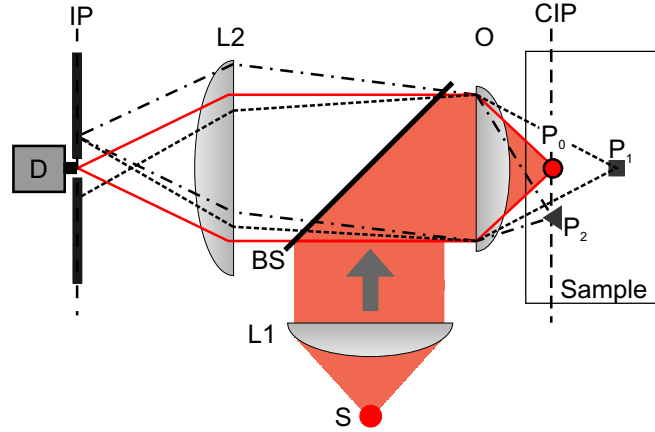


Figure 6.2.: Scheme of an inverted confocal optical microscope. S: illumination source, BS: beam splitter O: objective, L1: collimating lens L2: focusing lens, IP: image plane, CIP: conjugated image plane, P_0 : focal detection area, P_1 , P_2 : points outside focal detection area.

for illumination.

In a COM, where a point-source is used for illumination the excitation-PSF is also given by an Airy-pattern. The total-PSF is hence the square of the Airy-pattern, which reduces the lateral resolution to $\text{FWHM}_c = 0.37 \frac{\lambda}{NA}$. This is a factor of 1.3 smaller than the FWHM_w of wide-field microscopy. In practice the illumination source of a COM has a finite extend. To achieve optimum resolution the excitation-PSF has to be diffraction limited. Therefore the magnification M of the imaging system times the illumination source diameter has to be smaller than FWHM_w . $M = f_O/f_{L1}$ is determined by the focal length of the objective f_O and the collimating lens f_{L1} (see Fig. 6.2).

The main advantage of confocal microscopy compared to wide-field microscopy is the improved axial resolution, which allows for optical sectioning. The improved axial resolution is a result of the selective excitation and can be defined by $\text{FWHM}_{axial} = 2 \frac{n\lambda}{NA^2}$, which represent the axial extent of the total-PSF. For a detailed theoretical deduction of resolution in confocal microscopy by its point spread function we refer to [1, 84]. Further advantages of confocal microscopy is a improved signal to noise ratio in dense samples, reduces bleaching in fluorescing samples, and higher achievable excitation intensities.

Image formation in a COM can be achieved pixel by pixel by raster scanning either sample (piezoelectrically) or excitation beam (by mirrors) in x-y-direction and simulta-

neously recording the detector output at each x-y-position. A COM based on raster scanning the sample or focus is denoted as scanning confocal optical microscope (SCOM).

6.2.2. Description of the Experimental Setup

The SCOM setup is based on the inverted microscope with a piezo-electric scanner, described in section 6.1.1. The SCOM setup was designed for the excitation and detection of the two-photon excited photoluminescence (TPPL) of gold [29, 30]. In the detection path, filters are placed to discriminate the excitation light from the green shifted light produced by the TPPL process.

The SCOM setup is schematically depicted in Fig. 6.3. For the pulsed excitation a femtosecond (fs) Ti:sapphire laser (Tiger-200, Time-Bandwidth Co.) at a wavelength of 830 nm and a repetition rate of 80 MHz was used. The laser light was coupled into a single mode fiber (3MTM, FS-SN-4224, mode cut-off 697 nm) to guide it to the microscope. Light exiting the fiber was collimated (~ 10 mm beam diameter) and spectrally cleaned by a narrow band pass filter (Z 830/10x Chroma Tech.). The half-width of the pulse (from the peak to the 1/e position) was about 6 picoseconds (ps) (for details see section 6.2.4). The polarization of the light at the back aperture of the objective was adjusted by a fiber polarization controller (FPC) together with a near-infrared sheet polarizer (Melles Griot). The excitation beam was directed by a beams splitter to the objective (NA 1.3, Olympus) and to a photo diode (PDA 400, Thorlabs) used for continuous power control. In the detection path a bandpass (D600/300, Chroma Tech.) and notch filter (Kaiser Optical Systems) were used to suppress the excitation light. An analyzer (New Focus) could be used to probe the polarization state of the emitted light. The detection system could be switched by a flipable mirror between a single photon avalanche diode (SPAD, Perkin-Elmer AQR-13) and a grating spectrometer (Acton Research Corp., SpectraPro 2300i). The SPAD was used together with the bandpass filter to acquire SCOM images. The spectrometer was used with the notch filter only to acquire spectra of single structures.

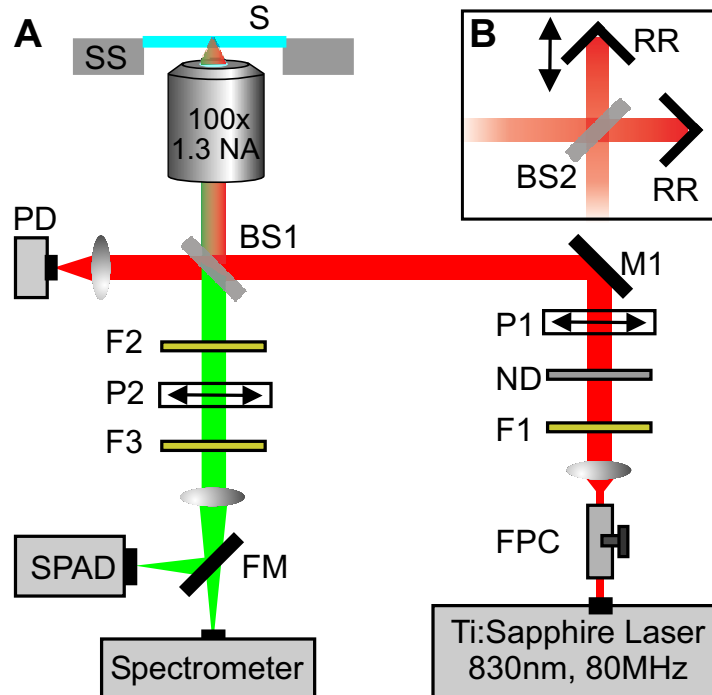


Figure 6.3.: Experimental setups used to investigate optical antennas. (A): Configuration for scanning confocal microscopy and local spectroscopy: S: sample, SS: regulated x-y scan stage, FPC: fibre polarization controller, F1: narrow band pass filter, F2: band pass filter, F3: holographic notch plus filter, ND: neutral density wheel, P1: NIR polarizer, P2: VIS analyzer (New Focus), M1: mirror, FM: flipable mirror, BS1,2 50/50 beam splitter, PD: photodiode for intensity measurements, SPAD: single photon counting avalanche diode. (B): Configuration used for autocorrelation measurements; the Michelson interferometer composed of BS2 and retro reflectors RR replaces M1 in A.

6.2.3. Polarization Adjustment

The polarization of the excitation beam was controlled by the FPC and P1. A sketch of the setup for the polarization adjustment is shown in Fig. 6.4A. First the FPC was adjusted without analyzer A in a way that turning P1 did not change the power measured with detector D at back aperture of the objective (see Fig. 6.4 B). This is equivalent to an almost circular polarization at the fiber output. Then by introducing analyzer A the polarization state could be adjusted in relation to the sample plane. Using the arrangement depicted in Fig. 6.4A each polarizer position could be assigned to a polarization direction in the sample plane. For example a polarization along the sample x-direction corresponds to the polarizer positions of 175° and 355° .

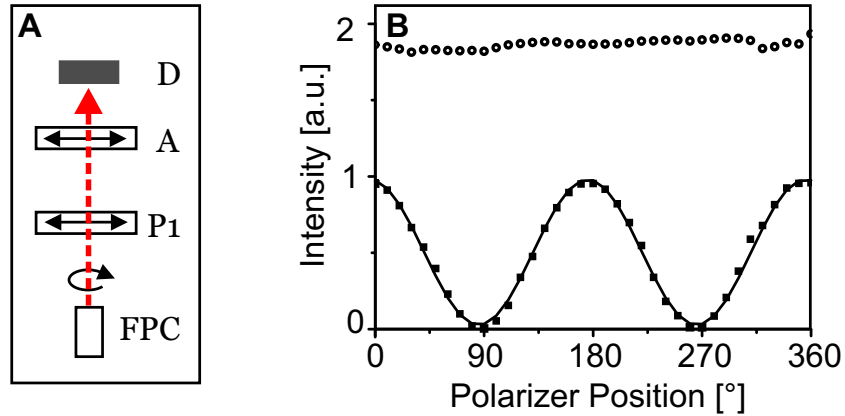


Figure 6.4.: Polarization adjustment of the incident beam. (A): Setup for adjustment. P1: polarizer (from Fig. 6.3), A: analyzer at back aperture position, D: detector (B): Detected power versus polarizer position. With (squares) and without (circles) analyzer. Solid line shows fit of the data to \sin^2 -law.

6.2.4. Laser Pulse Width

The fs pulse of the Ti:sapphire laser was coupled into a single mode fiber. Dispersion causes the pulse to spread while it propagates through the fiber. A dispersive medium is characterized by a frequency depended wave vector which for smooth variations can be approximated by its Taylor series: $k(\omega) = k_0 + k'(\omega - \omega_0) + \frac{1}{2}k''(\omega - \omega_0)^2 + \dots$, where $k' = \frac{dk}{d\omega}|_{\omega_0}$ and $k'' = \frac{d^2k}{d\omega^2}|_{\omega_0}$.

Mathematically, a pulse of a monochromatic source can be approximated by a transform-limited pulse

$$E(t) = E_0 \exp\left[-\frac{1}{2}(t/\tau)^2\right] \exp(i\omega_0 t) . \quad (6.1)$$

A short pulse in time has a finite width in frequency space. Since in a dispersive medium the propagation constant depends on the frequency, different parts of the pulse travel with different group velocities, which can results in a spreading of the pulse. The spreading of the pulse half-width τ to a new value τ_p can be calculated by [85]

$$\tau_p = \sqrt{\tau^2 + \left(\frac{k'' \cdot z}{\tau}\right)^2} , \quad (6.2)$$

where z is the travelling distance of pulse in the dispersive medium. In addition to the increase in width dispersion changes the pulse shape. For positive dispersion ($k'' > 0$) the frequency of the pulse increases linearly with time, also called positive chirp. Therefore the electric field of the pulse after propagation through the fiber is given by

[85]

$$E(t) = E_0 \exp\left[-\frac{1}{2}(t/\tau_p)^2\right] \exp[i(\omega_0 t + \beta t^2)], \quad (6.3)$$

where the chirp is quantified by β .

The pulse width of the laser pulse is commonly measured by nonlinear autocorrelation technique. In order to measure an autocorrelation function (ACF) we integrated a Michelson interferometer into the setup (see Fig. 6.3B). The incoming pulse was split into two pulses with identical power by a 50:50 beam splitter. The pulses were delayed in respect to each other by moving one retroreflector on a micrometer screw controlled baseplate. At the output of the Michelson interferometer the pulses are combined again and propagate collinear with a time delay t' in direction of the sample. The intensity at the output is given by $I(t, t') = |E(t - t') + E(t)|^2$, where $E(t)$ corresponds to the laser pulse field of a chirped pulse (see Eq. 6.3). The autocorrelation function (ACF) of n-order is given by

$$G(t') = \frac{1}{T} \int_{-T}^T [I(t, t')]^n dt, \quad (6.4)$$

where T is the detector response time. In an experiment the first order ACF is simply measured by recording the signal from a linear photo detector simultaneously with the time delay. For higher order ACF measurement one has to utilize nonlinear effects (e.g. second/third harmonic generation). Only the measure of higher order ACF can be used to determine the laser pulse width. A measurement of the first order ACF can only be used to determine the coherence length of the signal [86].

The nonlinear generation of photo luminescence (PL) from optical antennas (see Fig. 6.5A) was used to measure a higher order ACF. This was done by detecting the PL signal simultaneously with the RR position, which is proportional to the time delay. The RR position was measured with the help of a potentiometer coupled to the micrometer screw of the moveable RR. The first order ACF was measured simultaneously by the photo diode (see Fig. 6.3). The measured higher order ACFs are shown in Fig. 6.5B. The best fit to the measured data was achieved by a second order ACF of a chirped pulse (see Eq. 6.3) with $\tau_p = 5.7$ ps and $\beta = 0.8 \cdot 10^{-24} \text{ s}^{-2}$. The pulse half-width is in good agreement with the value ($\tau_p \approx 5$ ps) calculated from (6.2) using experimental parameters (fiber length: $z \approx 13$ m, initial pulse width: $\tau \approx 100$ fs, dispersion: $k'' \approx 40 \text{ ps}^2/\text{km}$ for SiO_2 at $\lambda = 830$ nm [85]).

The strong deviation of the measured data from the calculated second order ACF deviation near zero delay (Fig. 6.5B) is due to a higher-order nonlinearity which domi-

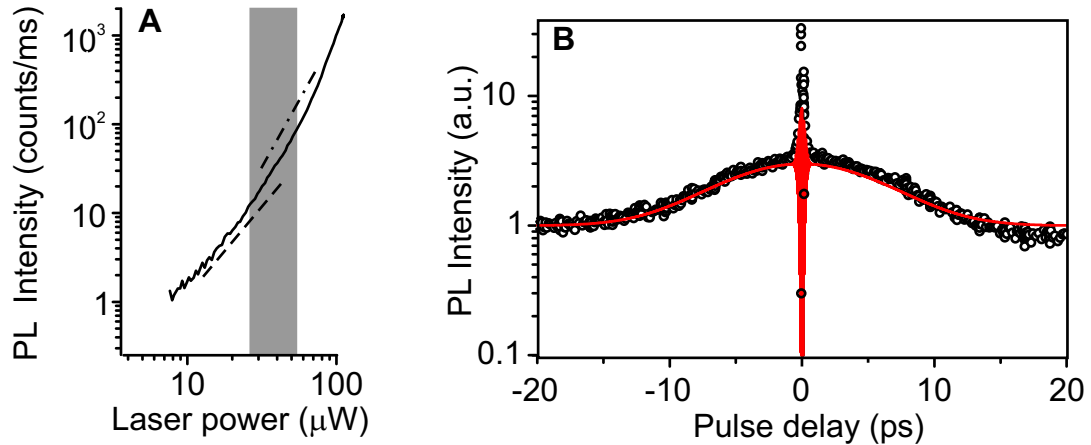


Figure 6.5.: (A) PL power dependence of the antenna used for ACF measurement. The nonlinearity is indicated: Dashed line - second order, dashed dotted line - third order. (B) Normalized autocorrelation signal of the excitation pulses with the antenna from (A) as nonlinear element. Open circles: Measured data, red line: Fit to a second order ACF of a chirped pulse.

nates at high power (see Fig. 6.5A). Close to zero delay the maximum average power at the back aperture increases due to constructive interference from about $27 \mu\text{W}$ to about $54 \mu\text{W}$, indicated by the gray underlay in Fig. 6.5A. This is connected to a shift from at least second order to at least third order nonlinearity in the PL signal. For a second order ACF the background to noise ratio is 1:8 and 1:32 for the third-order ACF [86]. The latter ratio fits quite well with the measured ratio of about 1:34 (see Fig. 6.5B).

Part III.

Results

7. White-light Continuum Generation by Resonant Optical Antennas

We demonstrate that gold dipole antennas can be designed and fabricated to match optical wavelengths. Specific antenna effects were identified with picosecond laser pulses powerful enough to excite white-light supercontinuum (WLSC) in addition to two-photon excited photoluminescence (TPPL) and by comparing explicitly the responses of optical antennas (OAs) and stripes. On resonance, strong field enhancement in the antenna feed gap leads to WLSC generation.

TPPL is a second-order process well documented for gold [26, 29, 30]. WLSC is a higher order optical nonlinearity found in various dielectric materials such as glass [31, 33] and water [32], but not in gold [26, 29, 30]. WLSC hence provides information on the field enhancement outside the OA arms. The mechanisms underlying WLSC are not well known but require a minimum power density of roughly 1 GW/cm^2 . Both mechanisms contribute to the "white light continuum" (WLC) recorded in our experiment, the contribution from each being distinguished by their spectral features and power dependencies.

7.1. Experimental

We fabricated slim dipole antennas and stripes with full length $L = 190$ to 400 nm and widths 45 nm from 40 nm thick gold patches on ITO coated glass cover slides (for details see section 5.2). Figure 7.1A shows a large-scale SEM image of the obtained structures. The numbers are used to identify the structures. Figure 7.1B shows identical region as in Fig. 7.1A, overlaid with high-resolution SEM images. The well-structured OAs and stripes are marked with squares ($2.5 \times 2.5 \mu\text{m}^2$). Poorly structured OAs/stripes and

7. White-light Continuum Generation by Resonant Optical Antennas

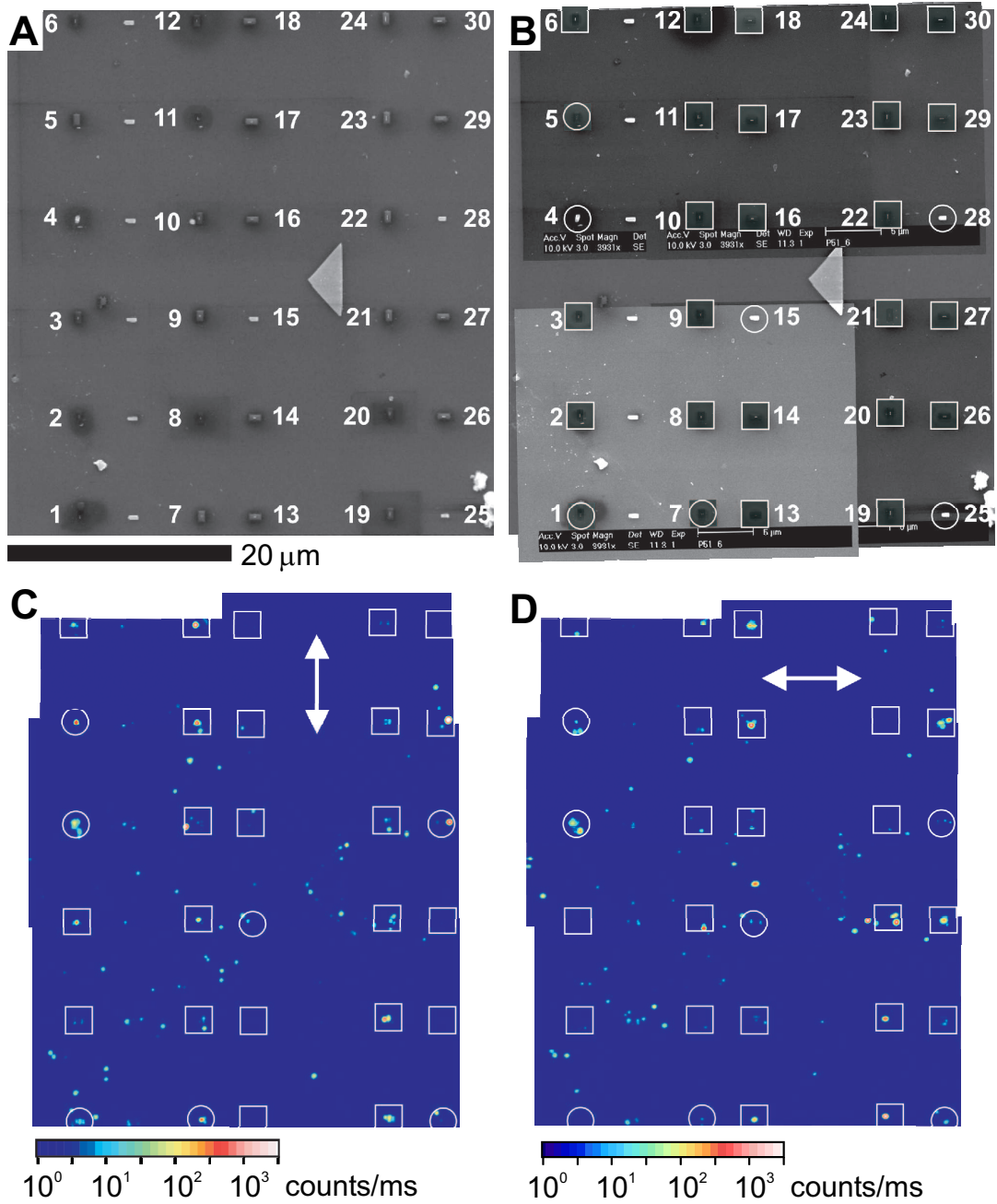


Figure 7.1.: (A, B) SEM image of sample with OA/stripe array and correlated (C, D) confocal images for horizontal and vertical polarization (white arrows)

unstructured patches are marked with circles.

The sample with the OA/stripe array was mounted in an inverted optical microscope modified for confocal operation in reflection (see section 6.2.2 and Fig. 6.3). Laser pulses with a maximum average power $150 \mu\text{W}$ were focused (1.3 NA, ∞) to a diffraction-limited spot on the sample (FWHM $\approx 325 \text{ nm}$). The pulse length ($\sim 6 \text{ ps}$ half width at $1/e$ position) was determined by means of an autocorrelation measurement (see section 6.2.4). The intensity in the laser focus has a peak value of $\sim 0.06 \cdot 10^9 \text{ W/cm}^2$ and is more than a factor 5 below the damage threshold. A similar damage threshold value for gold bow-tie antenna structures was obtained in [26]. The polarization at the sample was linear and adjustable in direction (see section 6.2.3). The pulses were spectrally cleaned with a line filter before entering the microscope and blocked with a notch filter in front of the detectors. Upon illumination with the pulsed laser (average power $110 \mu\text{W}$), white-light-continuum (WLC) was generated at certain sample positions. WLC emission maps were recorded by scanning the sample, using a single-photon counting avalanche diode (SPAD) in combination with an additional bandpass filter (450 – 750 nm).

7.2. Results and Discussion

The obtained confocal images for vertical and horizontal polarization are shown in Figs. 7.1C-D, both composed of 7 overlapping scan images each. The coincidence of the emission spots with the positions of OAs and stripes was confirmed with a precision of better than 100 nm by comparison of large-scale SEM and optical images (see Fig. 7.1).

Figure 7.2 gives an example for correlating SEM and confocal images of OAs and of a stripe. An overview of all OAs and stripes investigated (including enumeration) is presented in the appendix C (Figs. C.2-C.4). Sizeable WLC emission was found only at the positions of OAs, for OAs of a certain length range, and for OAs orientation along the pump polarization (see e.g. Fig. 7.2C, #12). Due to the strong nonlinearity, WLC is observed only for a narrow range of angles around the polarization direction parallel to the antenna (0°) and vanishes completely for orthogonal polarization (90°) (see Fig. 7.3). A fit of the data to a \cos^8 -law indicates a fourth order nonlinearity of the process generating the WLC. We also analyzed the emission properties of the

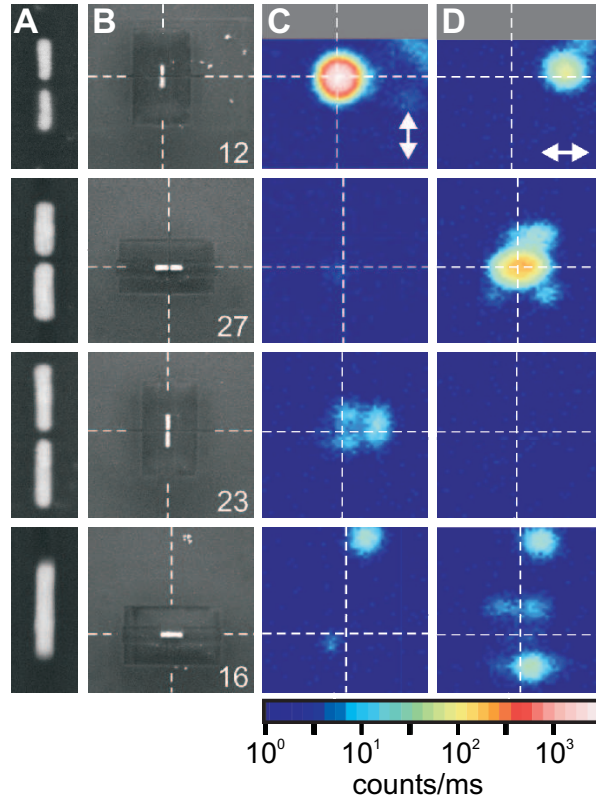


Figure 7.2.: Examples of OAs and of a stripe. (A and B) SEM images, zoom and overview, respectively. (C and D) confocal scan images of the WLC generated by vertically and horizontally polarized laser pulses, respectively (average power $110 \mu\text{W}$, logarithmic color code). Dimensions: (A) $180 \times 450 \text{ nm}^2$; (B to D) $2 \times 2 \mu\text{m}^2$.

OAs. Therefore the excitation polarization was oriented 45° off the antenna main axis and WLC was recorded as a function of analyzer (P2 in Fig. 6.3) orientation. The emitted light is polarized along the OA main axis as well, independent of the excitation polarization, which indicates the importance of the OA also for the process of WLC emission (Fig. 7.3). For comparison, signals from stripes are barely detectable (Fig. 7.2C, #16), and are frequently associated with WLC generation at the rims of the depressions around the antenna.

For the identification of the nonlinear process responsible for WLC emission we measured spectra and power dependencies of individual structures at fixed sample positions. The WLC spectra (Fig. 7.4) extend over a considerable range on both sides of the laser line independent of antenna length. We concentrate here on the short wavelength wing. At

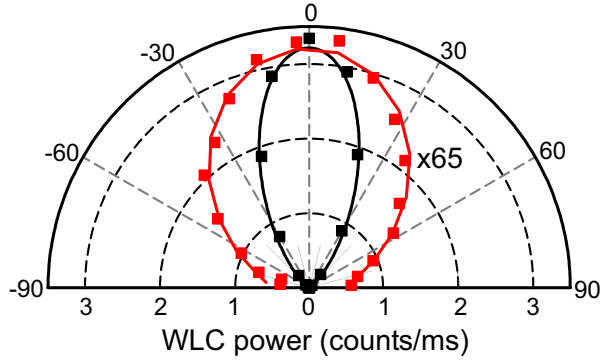


Figure 7.3.: Polarization dependence of WLC excitation and emission recorded on antenna #12 with an average power of $\sim 110 \mu\text{W}$. Black squares: WLC emission as function of polarization of the excitation laser. Black line: Fit of the data to a \cos^8 -law. Red squares: detected WLC as a function of analyzer orientation. Red line: Fit of the data to a \cos^2 -law.

low power, the intensity falls off monotonously towards short wavelengths, typical for TPPL of gold [29, 30]. At high power, the spectrum is dominated by a broad peak around 560 nm that we assign to WLSC. The increase with excitation intensity of the area underneath the peak around 560 nm indicates a higher than 3-order nonlinear process, which is typical for the WLSC generation process.

Fig. 7.5 shows the dependence of WLC power on laser power for OAs of different lengths. The log/log curves first rise with slope 2 (dashed lines), which is typical for TPPL. For high-power excitation, the curves follow a fourth-order power law (dash-dotted lines), supporting the above assignment to WLSC.

The nonlinearity of the WLC process was used to determine the laser pulse length right at the position of an OA by means of the autocorrelation technique (see section 6.2.4) with a slightly modified setup (see Fig. 6.3B). The measured autocorrelation function (Fig. 6.5B) has a background to noise ratio of 1:34 at zero delay and average excitation power of $54 \mu\text{W}$. This ratio corresponds to a higher than third-order nonlinear process [86] involved in WLC generation. The same result is determined by the measured power dependence. A slope > 3 at $54 \mu\text{W}$ is measured for the antenna #11 (see Fig. 7.5) used for the autocorrelation measurement.

We note that Refs. [26, 30] report second-order behavior only although the same materials and a similar range of excitation power are applied. The main differences to the present experiment are the use of femto- instead of picosecond laser pulses and of structures of a different, possibly less favorable shape.

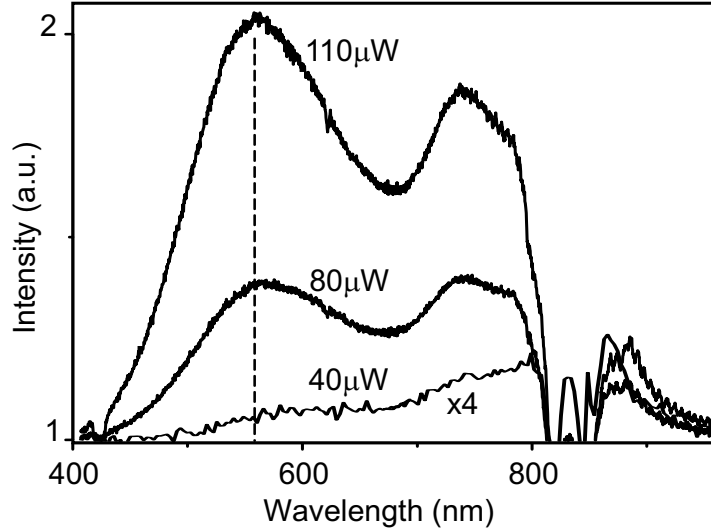


Figure 7.4.: WLC spectra of antenna #11 for different excitation powers. Note the increase of the peak at 560 nm for increasing excitation power

The field enhancement in the antenna feed gap obviously increases with decreasing width [26, 87], variation of the overall antenna length should result in a pronounced resonance in analogy to the radio wavelength regime (see section 2.4.4). The variation of WLC power with OA/stripe length L is displayed in Fig. 7.6A (see appendix Fig. C.1 for numeration) for low- and high-power excitation, corresponding to a dominance of TPPL and WLSC, respectively. For the shortest and largest lengths, the antenna emission is about ten times ($30 \mu\text{W}$), respectively a hundred ($110 \mu\text{W}$) times stronger than the emission of the corresponding stripes. The antenna emission goes through a maximum in between, while the stripe emission hardly varies over the whole range of lengths. The ratio of emission intensities between stripes and OA reaches values as large as ~ 30 (#17, $L = 258 \text{ nm}$) and ~ 2000 (#12, $L = 250 \text{ nm}$), respectively. The emission data scatter considerably between individual antennas although only structures were included in Fig. 7.6A that showed a high degree of perfection in the SEM (see appendix C Figs. C.2-C.4A,B). This suggests that the WLC emission might be influenced also by material imperfections not visible in the SEM. The emission from the antennas is more than 10^3 times stronger than that from solid gold stripes of the same dimensions but without feed gap. Variation of the overall length of the antenna reveals a sharp resonance significantly below one half of the effective excitation wavelength.

The near-field intensity enhancement factor ($= |E/E_0|^2$) 10 nm above OAs and stripes vs. length L in steps of 20 nm, was computed by O. J. F. Marin using the Green's tensor

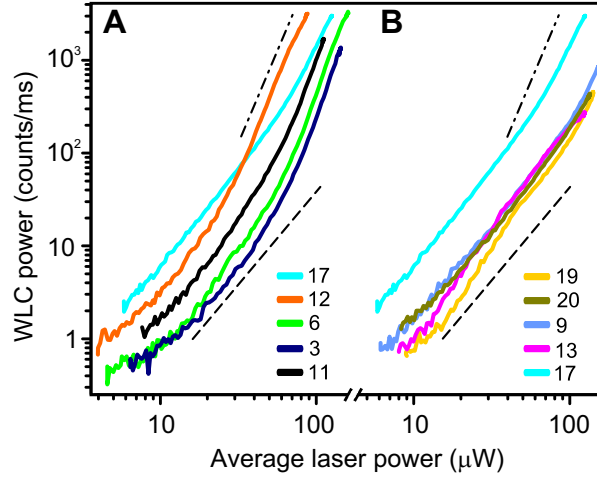


Figure 7.5.: WLC power dependence of ORAs with different lengths, grouped according to the dominant nonlinearity. (A) Fourth order, dashed-dotted line. (B) Second order, dashed line.

technique [54]. E_0 refers to the incident evanescent field in the absence of an antenna. Figure 7.6, B to D reveal drastic differences between antennas and stripes of the same length as well as between antennas of different lengths. This refers to both spatial distribution and amplitude of the enhancement. The strong field concentration in the feed gap of the resonant antenna (Fig. 7.6C) suggests that WLSC is generated mainly in the underlying ITO/glass substrate, possibly also in water that might condense inside the gap or in the air next to the gap.

As a figure of merit for the antenna response, $R(L)$, we use the near-field intensity, integrated, i.e. averaged over the whole antenna area plus its immediate environment ($600 \times 200 \text{ nm}^2$). Although being a somewhat arbitrary choice, the similarity of $R^2(L)$ and $R^4(L)$ with the experimental data is obvious, showing a flat response for the stripes, but a pronounced peak for the OAs for the same antenna length as in the experiment (Fig. 7.6A). No fit parameters were used in Fig. 7.6A except for a scaling factor.

Both experiment and computer simulation reveals a sharp OA resonance. The OA resonance length refers to the excitation wavelength, since WLSC generation depends critically on the field enhancement in the gap. From classical antenna theory we would expect that the first antenna resonance occurs close to half of the excitation wavelength. The permittivity of the substrate and the finite thickness of the antennas reduce the wavelength at the interaction zone. Assuming an intermediate refraction index $n = 1.25$ for the

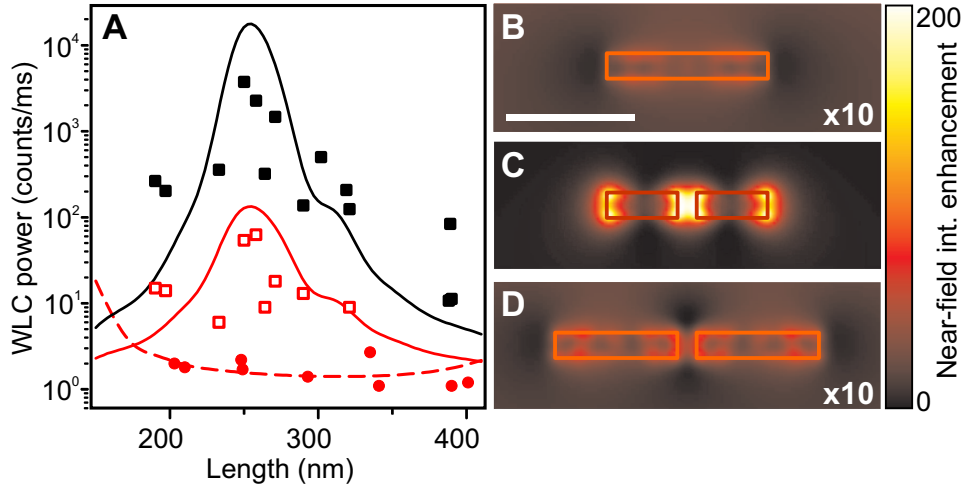


Figure 7.6.: Fig. 4. (A) Variation of WLC power with antenna/stripe length. Filled and open squares, OA at 110 and 30 μW , respectively; circles, stripe at 110 μW ; solid red and black curves, $R^2(L)$ and $R^4(L)$ for OAs, respectively; dashed line, $R^2(L)$ for stripes. (B to D) Near-field intensity enhancement factor computed 10 nm above a stripe ($250 \times 40 \text{ nm}^2$), a resonant antenna ($250 \times 40 \text{ nm}^2$), and an off-resonant antenna ($410 \times 40 \text{ nm}^2$), feed gap 30 nm, gold on glass, $\lambda = 830 \text{ nm}$, $\varepsilon = -25.3 + i1.6$ [49] and 2.25, respectively. Scaling factor in (B) and (D), $10 \times$. Scale bar, 200 nm.

glass/air interface the effective excitation wavelength reduces to $\lambda_{\text{effective}} = 830/1.25 \text{ nm}$. The half-wave resonance of a classical antenna would therefore be expected at an antenna length of $\sim 330 \text{ nm}$. This is in contrast to the observed resonance, which is significantly below one half of the effective excitation wavelength.

As discussed in section 4 the surface plasmon resonances could have an influence on the resonance length of an OA. To estimate the influence of surface plasmon resonances on the antenna resonance we compared the antenna resonance of gold OAs with that of an aluminium OAs. For this simulation we used a commercial FDTD program (LUMERICAL). Figure 7.7A shows the calculated maximum intensity enhancement in the feed gap center versus OA length. The antenna geometry and monitor plane is depicted in Fig. 7.7B. The intensity enhancement of the gold structure shows a resonance peak at a similar position as observed in the experiment and calculated with the Green's tensor technique [54]. In particular, the shoulder to the right of the resonance is reproduced. An antenna resonance is also present for aluminium dipole antennas. The resonance length ~ 325 of a aluminium antenna is in agreement with classical antenna theory close to one half of the effective wavelength of 330 nm. In contrast to gold, aluminum dipole

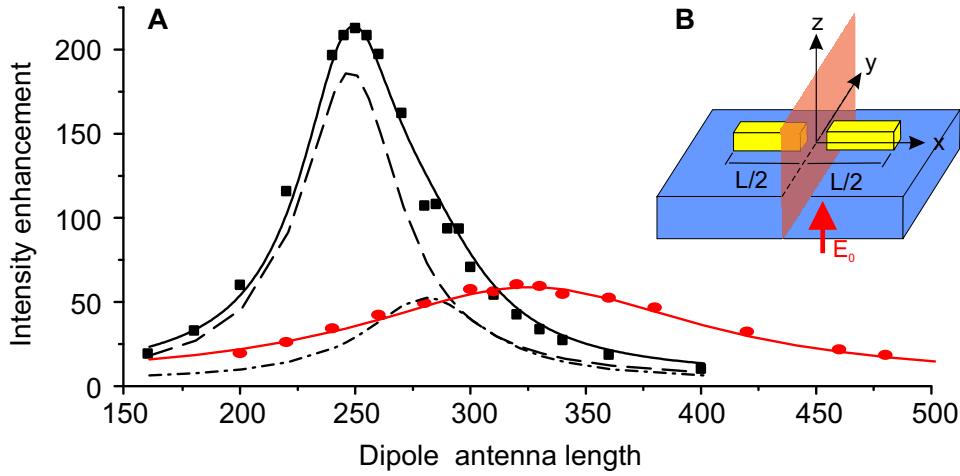


Figure 7.7.: (A) Maximum intensity enhancement in the center of the antenna feed gap versus antenna length. Dots: data points obtained from FDTD simulations, black for gold , red for aluminum. Red line: fits to Lorentzian peak function. Black line: fit to a sum of two Lorentzian peak functions indicated by the dashed and dashed-dotted line. (B) Geometry and field monitor plane used for FDTD simulation.

antennas show a much broader resonance and four times less intensity enhancement. A contribution from localized surface plasmon (see section 3.2.2) resonances can be excluded for aluminium antennas at the analyzed wavelength and structural dimension. Therefore we relate the strong shift in resonance length of the gold dipole antenna to the excitation of a surface plasmon mode with strong field concentration in the antenna feed gap. The shoulder to the right of the resonance reproduced with both simulation methods is interpreted as the classical half-wave resonance of gold. For a modified antenna design that results in a coincidence of the plasmon resonance with the antenna resonance even higher field enhancement factor may be expected. Further increase of the enhancement is expected from a reduction of the feed gap width [26, 87, 88].

7.3. Summary

We have fabricated nanometer-scale gold dipole antennas, designed to be resonant at optical frequencies. On resonance, strong field enhancement in the antenna feed gap leads to white-light super continuum generation. White-light emission from resonant antennas is more than 10^3 times stronger than that from solid gold stripes of the same

dimensions but without feed gap. The antenna length at resonance of a gold dipole antenna is considerably shorter than one half of the wavelength of the incident light. This is in contradiction to classical antenna theory, but in qualitative accordance with computer simulations that take into account the finite conductivity of metals at optical frequencies. Computer simulation revealed that the resonance length of exact the same dipole structure, but made from aluminium is close to half the wavelength of the incident light. Therefore we identify the strong enhancement and shift in the resonance length of the gold dipole antenna with the excitation of a surface plasmon mode with strong field concentration in the antenna feed gap. This means, that the existence of surface plasmon resonances and a slightly adapted antenna design can greatly enhance antenna performance in the optical wavelength range.

WLSC originating from the feed gap volume provides very unusual illumination properties that may allow for new forms of local spectroscopy (for instance single-molecule Raman) and interactions with nano-structures and single-quantum systems.

8. Near-field Studies of Optical Antennas

Imaging of confined fields in an OA feed-gap requires near-field techniques and was so far only performed for microwave antennas [9]. Here we report on our approach that aimed on the direct imaging of confined optical fields inside a bow-tie antenna feed-gap by means of a scanning tunnelling optical microscope (STOM). The bow-tie antenna was chosen for their simple design, their broadband resonance characteristic [47], and because of the high field enhancement expected in the antenna feed-gap [26]. Comparison of measurement and simulation indicates that intense, localized near-field features of a resonant optical antenna were imaged by STOM.

In STOM the interpretation of the detected signals is a crucial and difficult problem (see section 6.1). In an ideal case, assuming a non-disturbing point like probe, the detected signal is proportional to the intensity distribution $I(\mathbf{r}, \omega) = |\mathbf{E}(\mathbf{r}, \omega)|^2$ at the probe position. In STOM experiments with uncoated tapered fiber probes one has to account for the finite tip, which integrates the optical field over a certain volume. STOM analysis of single square metal structures suggests, that the signal detected with a probe at constant height h_1 is similar to the calculated near-field intensity at a different height $h_2 > h_1$. The choice of h_2 in the calculation corresponds to a rough modelling of the averaging process occurring inside the finite tip volume [74].

For the interpretation of our STOM measurements we followed a slightly different approach. We calculated the near-field intensity distribution I_{near} for a height of 10 nm to include intense near-fields that couple to the tip apex. To account for the collection efficiency of a sharp tip only the xy-components of the electric field are considered in I_{near} . Further we calculated the 'far-field' intensity distribution I_{far} for a height of 150 nm above the structure to include far-field components that couple to the tip shaft. The final intensity distribution measured by a STOM tip is modelled by a summation of $c \cdot I_{near}$ and I_{far} . The small collection efficiency of the finite tip volume compared to

the tip shaft is included by a constant factor c .

8.1. Experimental

The bow-tie structure was cut out of a 35 nm thick gold patch by means of FIB milling in a similar way as described for the linear dipoles in section 5.2. Figure 8.1 shows an SEM image and a topographic image of the fabricated structure. A total length $L \sim 300$ nm,

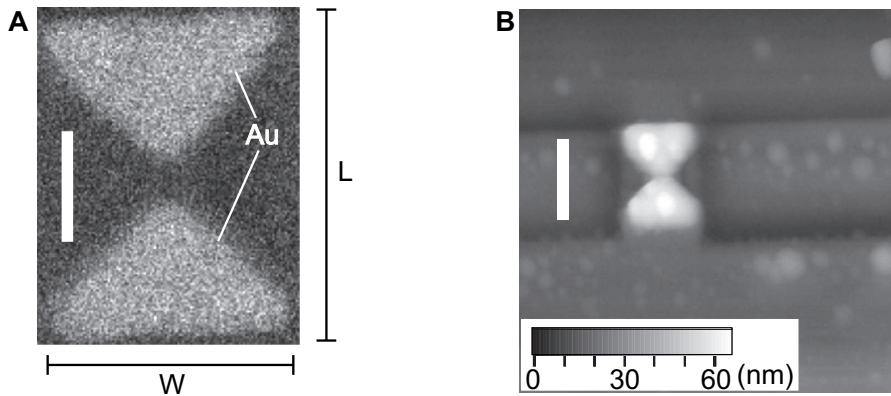


Figure 8.1.: Investigated bow-tie antenna. (A) SEM image; scale bar 100 nm. (B) Topography, acquired with shear-force feedback; scale bar 300 nm

a width $W \sim 220$ nm and a feed-gap size of ~ 30 nm was measured in the SEM image (Fig. 8.1A). The topographic image reveals, that the structure is surrounded by a rough, 20-30 nm deep depression (see Fig. 8.1B), which results from the structuring process (see section 5.2).

STOM images of the structure were acquired with the setup described in section 6.1.1. Key features of the setup are: (1) The shear-force feedback, which keeps a constant distance (~ 10 nm) between tip and sample. (2) The illumination of the sample under total internal reflection, established by different cw laser diodes (532 nm, 675 nm or 830 nm). (3) Adjustable polarization (e.g. s- and p-polarization). (4) Optical image and shear-force image were acquired simultaneously.

Dielectric tapered tips, produced by tube etching [89] of a single mode fiber (cut-off wavelength 630 nm), were used as near-field probes. The use of bare dielectric tips is advisable, since a metalized tip in dimension similar to the antenna structure would strongly disturb the near-field because of multiple scattering between tip and sample.

Furthermore a metalized tip would detune the antenna resonance. In addition, the topographic resolution of a metalized tip is reduced due to its large tip radius, which would make a direct cross reference of optical and topographic image much more difficult.

8.2. FDTD Simulations

We performed FDTD simulations [55] for a gold bow-tie geometry on a flat glass support. The bow-tie geometry ($W = 220$, $L = 300$, height= 35 nm, feed gap size= 30 nm) chosen for the simulation was similar to the structure produced by FIB milling (Fig. 8.1A). A sketch of the geometry used for the simulation is shown in Figure 8.2. Note that the corners forming the feed gap of the bow-tie structure was assumed to be flat over a distance of 10 nm (Fig. 8.2). The dielectric function for gold [49] and glass was given by the simulation software. The discretization cells were chosen to be $3 \times 3 \times 3$ nm³ cubes. Exemplarily two monitor planes ($x = 0$ nm and $y = 0$ nm) are indicated in Fig. 8.2B. The simulation was performed for two incident direction of s-polarized light (Fig. 8.3A). Normal incident was chosen to appreciate the influence of the antenna length L on the achievable field enhancement. Fig. 8.3B shows the calculated maximum field enhancement for varies wavelength calculated for the $y = 0$ nm plane, that corresponds to the center of the feed gap. Due to a limitation in the FDTD software (LUMERICAL), the

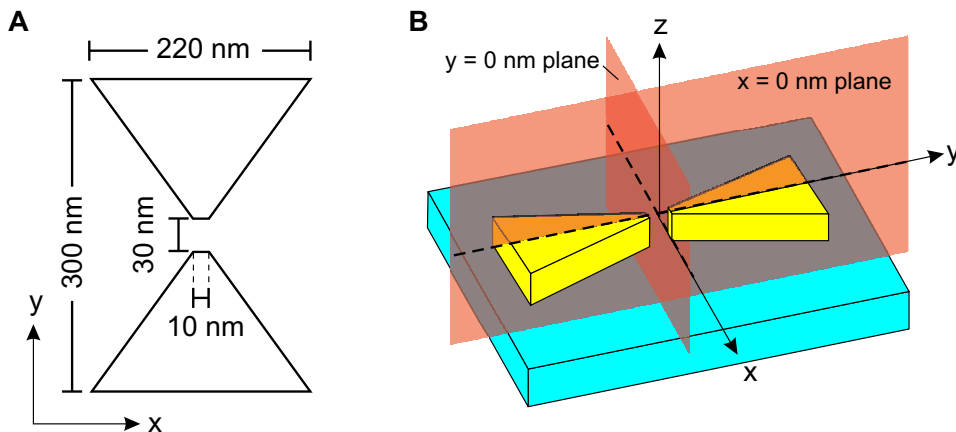


Figure 8.2.: Sketch of bow-tie geometry . (A) Bow-tie dimensions used for FDTD simulations, $height = 35$ nm (B) Position of field monitor planes used for FDTD simulations.

maximum incident angle was limited to 55° . This differs from the actual experimental

situation, where the angle of incident was $\sim 70^\circ$. According to the simulations the influence of the incident angle on the antenna resonance wavelength is not very pronounced. The resonance wavelength shifts slightly from around 900 nm for normal incident to 875 nm for the 55° incident light. Notable is the drop of the intensity enhancement from ≈ 350 down to ≈ 100 .

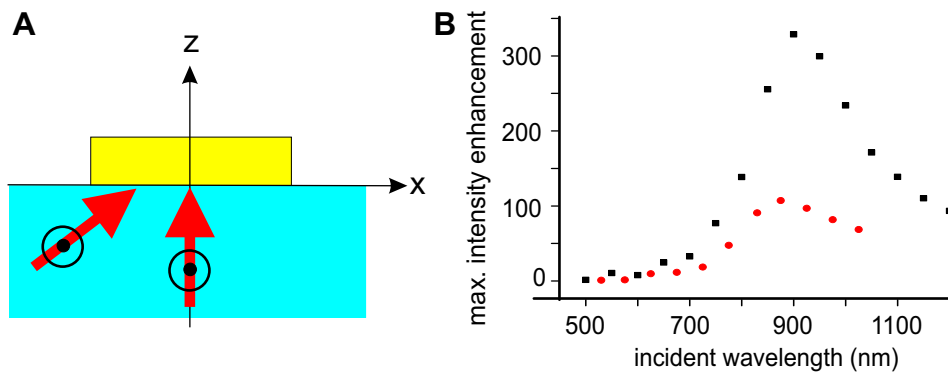


Figure 8.3.: (A) Sketch of two different angle (0° and 55°) of incident light used for the simulations; polarization along y-axis. (B) Maximum field enhancement in $y = 0$ nm plane (i.e. feed-gap) for normal incident (black) and for an incident angle of 55° (red).

8.3. Results and Discussion

STOM measurement were performed for three wavelengths under s- and p-polarizations with one and the same tip in constant gap mode. Therefore a comparison of the different STOM images is possible and helps to distinguish topographic artifacts from local field enhancement signatures. The acquired, normalized optical STOM images are shown in Fig. 8.4A1-A3 and Fig. 8.5A1-A3. The images were normalized to the average intensity of the evanescent wave measured on a flat glass air interface without structure. For the interpretation of the images one has to take into account that pure dielectric probes have the disadvantage that the near-field components detected by the tip apex are superimposed with far-field components. Especially STOM images recorded on strongly scattering particles and on rough surfaces are affected by scattered field components that couple to the fiber along the tip shaft [77]. Therefore we assign the extended area of intensity enhancement observed in all measurements (see Figs. 8.4 and 8.5 A1-A3) to far-field components.

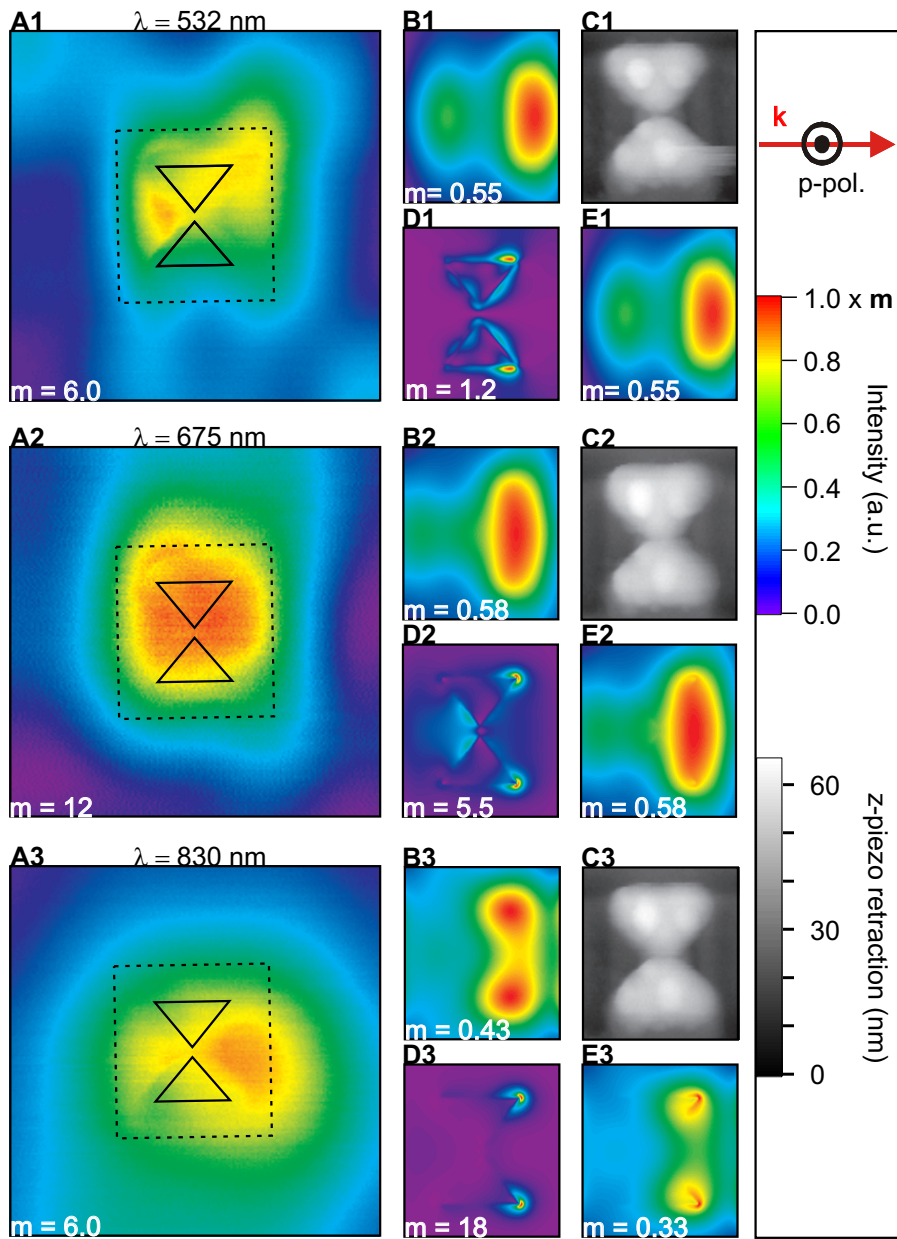


Figure 8.4.: STOM images and FDTD calculation for p-polarization. A1-A3: Optical STOM images at indicated wavelength with marked position of bow-tie antenna. Box sizes ($450 \times 500 \text{ nm}^2$) equal to image size in B-E; m : Maximum value of the color scale. B1-B3: Calculated near-field intensity 150 nm above glass/air interface. C1-C3: Shear-force image. D1-D3: Calculated near-field 45 nm above glass/air interface. E1-E3: Image composed from B and D.

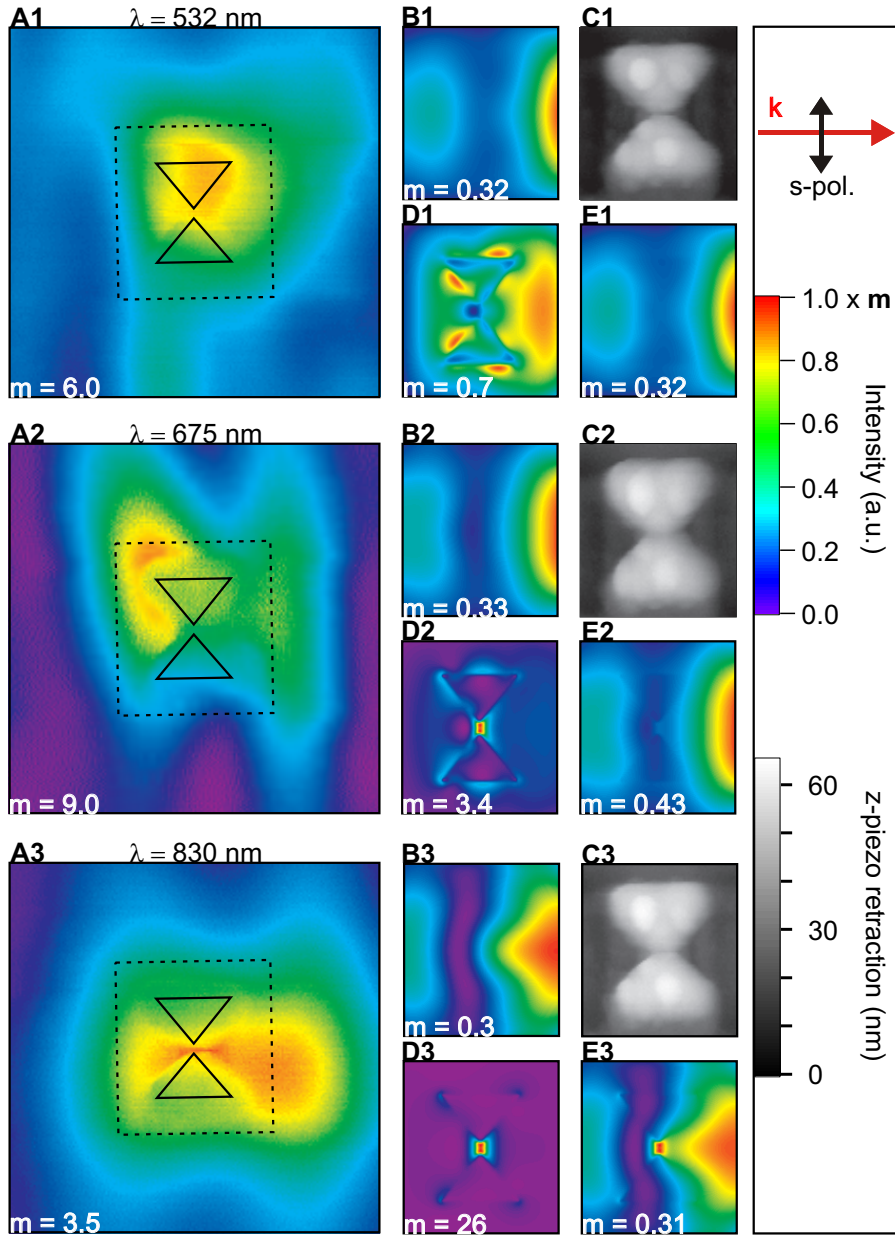


Figure 8.5.: STOM images and FDTD calculation for s-polarization. A1-A3: Optical STOM images at indicated wavelength with marked position of bow-tie antenna. Box sizes ($450 \times 500 \text{ nm}^2$) equal to image size in B-E; m : Maximum value of the color scale. B1-B3: Calculated near-field intensity 150 nm above glass/air interface. C1-C3: Shear-force image. D1-D3: Calculated near-field 45 nm above glass/air interface. E1-E3: Image composed from B and D.

Now we want to see in more detail if our measurements can be reproduced by FDTD simulations. As discussed we assume that the measured intensity recorded in the STOM images is a superposition of near-field and far-field components. To account for the far-field we calculated the field intensity distribution $I_{far} = (|E_x|^2 + |E_y|^2 + |E_z|^2)/|E_0|^2$ at a height $z = 150$ nm above the glass/air interface, normalized to the incident field E_0 (Figs. 8.4B1-B3 and Figs. 8.5B1-B3). Similar to the measured data the intensity I_{far} is extended over a large area and does not show any field localization. The maxima ($m = 0.3 - 0.6$) and average values of the simulated intensity I_{far} are like the measured data ($m = 3.5 - 12$) within one order of magnitude. The absolute intensity values are not reproduced, since the simulation does only account for the intensity in one plane. Generally higher values of the maximum and average intensity are calculated for p-polarization, which is in agreement with the measured data. Only the STOM image in Fig. 8.5A3 shows a strongly localized area right over the antenna feed-gap, not observed for the other polarizations and wavelengths.

For the calculation of the near-field intensity we considered that sharp tips are more sensitive to the x - y components, whereas damaged tips are also sensitive to the z components of the electric field [81, 90]. The good topographic resolution that is evident from Figs. 8.4C1-C3 and Figs. 8.5C1-C3 indicates that the used tip was quite sharp. Therefore we neglected the z -component of the electric field and calculated the near-field intensity enhancement $I_{near} = (|E_x|^2 + |E_y|^2)/|E_0|^2$ in a height $z = 45$ nm above the glass/air interface (Fig. 8.4C1-C3 and Fig. 8.5C1-C3). Where z is given as the sum of structural height (~ 35 nm) and tip-surface distance (~ 10 nm). Figures 8.5D2 and D3 show highly localized fields for a excitation wavelength of 675 nm and 830 nm and for s-polarization, but only for 830 nm the field has sizeable intensity. For p-polarization high fields on the two outer edges of the structure in Fig. 8.4D3 are observed. Note that in the simulation outer edges of the structure are sharper than the edges forming the gap.

Further we assumed that the far- and near-fields have different coupling efficiencies. With this assumption the total simulated intensity, which compares to the measured intensity is given by

$$I_{tot} = I_{far} + c \cdot I_{near} , \quad (8.1)$$

where c is an arbitrary but constant factor. $c = 0.8 \cdot 10^{-2}$ was chosen to give the best visual agreement between simulated and measured data. The result, I_{tot} is shown in Fig. 8.4E1-E3 and Fig. 8.5E1-E3. A weak near-field signal is likely to be obscured by

the simultaneously detected far-field (background). The near-field intensity in the gap is only visible and clearly distinguishable from the background intensity in Fig. 8.5E3. Note that here a maximum in near-field intensity falls together with a minimum in far-field intensity, which is in accordance with the measured image in Fig. 8.5A3. It seems that the collection efficiency for far-fields was ~ 100 higher than for near-fields, which can be explained by the vast difference in volume between tip apex and the tip shaft.

Figure 8.5A3 is analyzed in more detail in Fig. 8.6. A line profile (Fig. 8.6B), along the line indicated in the magnified image (Fig. 8.6A), shows a intensity localization of about 20 nm. This is even smaller than the gap and probably results from the fact

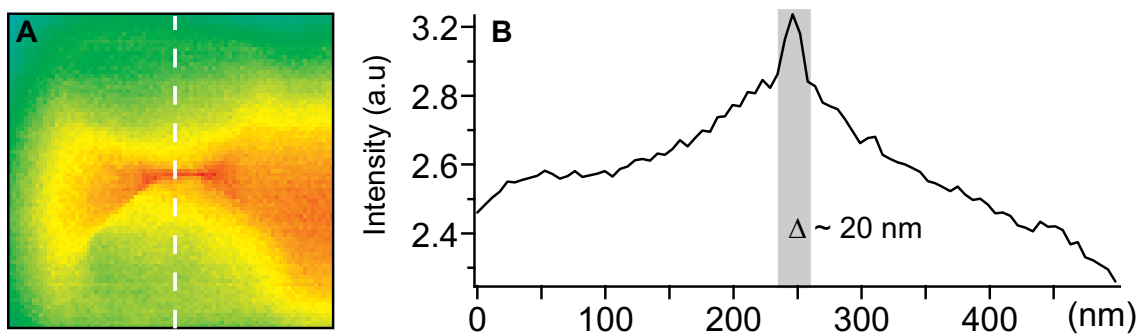


Figure 8.6.: (A) Magnification of region with intensity enhancement; measured for 830 nm and s-polarization (500×500 nm²). (B) Line profile along the line indicated in (A).

that the tip slightly dips into the gap (see Fig. 8.5C3), where the intensity is highest. The strong localization of the field enhancement in the feed-gap and its strong decay outside the gap is demonstrated by near-field simulations (Fig. 8.7). Perpendicular to the dashed line in Fig. 8.6A the field intensity is quite extended and looks almost like a far-field pattern of a dipole. This is in agreement with our assumption, that only right over the feed-gap near-field components couple into the tip, whereas further to the side the far-field dominates the measured intensity.

8.4. Summary

A nanometer sized bow-tie antenna structure was investigated by STOM for s- and p-polarized light and three different wavelength (532 nm, 675 nm, 830 nm). A shear-force

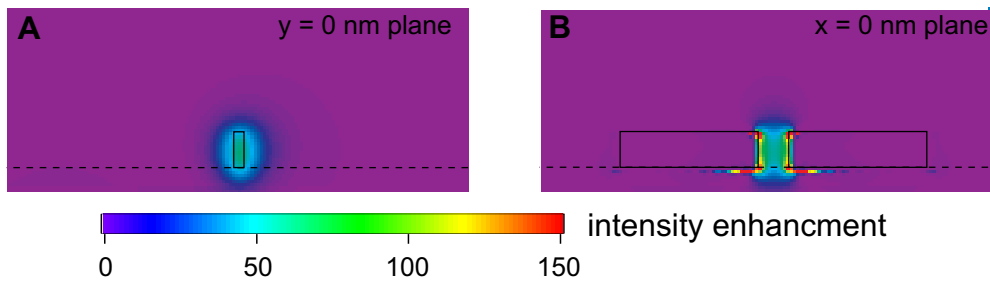


Figure 8.7.: Field enhancement in $y = 0$ nm (A) and $x = 0$ nm (B) plane for an incident wavelength of 830 nm. Boxes outline bow-tie geometry. Dashed line indicates glass/air interface.

feedback system allowed for a direct comparison of optical and topographic image. Both, experiment and simulation showed a frequency dependant variation of the field intensity at the feed-gap of an optical antenna. We relate this to a resonance behavior of the analyzed bow-tie structure, similar to radio wave antennas. Only at resonance highly localized and enhanced fields are present in the feed-gap. Further we demonstrated the potential of STOM to image high localized fields in extension far below the diffraction limit. As precondition we identified the existence of extremely high, localized near-fields, that dominate over the detected far-fields.

Bibliography

- [1] L. Novotny and B. Hecht. *Principles of Nano-optics*. Cambridge University Press, Cambridge, 1 edition, in press.
- [2] D.W. Pohl, W. Denk, and M. Lanz. Optical stethoscopy: Image recording with resolution $\lambda/20$. *Appl. Phys. Lett.*, 44:651–653, 1984.
- [3] B. Knoll and F. Keilmann. Near-field probing of vibrational absorption for chemical microscopy. *Nature*, 399:134–137, 1999.
- [4] A. Naber, D. Molenda, U.C. Fischer, H.-J. Maas, C. Höppener, N. Lu, and H. Fuchs. Enhanced light confinement in a near-field optical probe with a triangular aperture. *Phys. Rev. Lett.*, 89:210801–210804, 2002.
- [5] E.J. Sánchez, L. Novotny, and X. S. Xie. Near-field fluorescence microscopy based on two-photon excitation with metal tips. *Phys. Rev. Lett.*, 82:4014–4017, 2005.
- [6] A. Hartschuh, E.J. Sanchez, X.S. Xie, and L. Novotny. High-resolution near-field raman microscopy of single-walled nanotubes. *Phys. Rev. Lett.*, 90:095503–095504, 2003.
- [7] D.W. Pohl, U.Ch. Fischer, and U.T. Dürig. Scanning near-field optical microscopy (snom): Basic principles and some recent developments. *Proc. SPIE*, 897:84, 1988.
- [8] M. Fee, S. Chu, and T.W. Hänsch. Scanning electromagnetic transmission line microscope with sub-wavelength resolution. *Optics Commun.*, 69:219, 1989.
- [9] R. D. Grober, R. J Schoellkopf, and D. E. Prober. Optical antenna: Towards a unity efficiency near-field optical probe. *Appl. Phys. Lett.*, 70:1354–1356, 1997.

- [10] Ch. Fumeaux, J. Alda, and G.D. Boreman. Lithographic antennas at optical frequencies. *Opt. Lett.*, 24:1629–1631, 1999.
- [11] D.W. Pohl. *Near-Field Optics: Principles and Applications*, chapter Near field optics seen as an antenna problem. World Scientific, Singapore, 2000. The Second Asia-Pacific Workshop on Near Field Optics, Beijing, China October 20-23, 1999; Ohtsu, M. and Zhu, X. eds.
- [12] K.B. Crozier, A. Sundaramurthy, G.S. Kino, and G.S. Quate. Optical antennas: Resonators for local field enhancement. *J. Appl. Phys.*, 94:4632–4642, 2003.
- [13] K. Kneipp, Y. Wang, H. Kneipp, L.T. Perelman, I. Itzkan, R.R. Dasary, and M.S. Feld. Single molecule detection using surface enhanced raman scattering (sers). *Phys. Rev. Lett.*, 78:1667–1670, 1997.
- [14] J.B. Jackson, S.L. Westcott, L.R. Hirsch, J.L. West, and N.J. Halas. Controlling the surface enhanced raman effect via the nanoshell geometry. *Appl. Phys. Lett.*, 82:257–259, 2003.
- [15] A.J. Haes, W.P. Hall, L. Chang, W.L. Klein, and R.P. Van Duyne. A localized surface plasmon resonance biosensor: First steps toward an assay for alzheimer’s disease. *Nano Letters*, 4:1029–1034, 2004.
- [16] L. Novotny, R.X. Bian, and X.S. Xie. Theory of nanometric optical tweezers. *Phys. Rev. Lett.*, 79:645–648, 1997.
- [17] H. Xu and M. Käll. Surface-plasmon-enhanced optical forces in silver nanoaggregates. *Phys. Rev. Lett.*, 89:246802–4, 2002.
- [18] A.J. Hallock, P.L Redmond, and L.E. Brus. Inaugural article: Optical forces between metallic particles. *Proc. Natl. Acad. Sci. U S A*, 102:1280–1284, 2005.
- [19] J. R. Krenn and et al. Squeezing the optical near-field zone by plasmon coupling of metallic nanoparticles. *Phys. Rev. Lett.*, 82:2590–2593, 1999.
- [20] S.I. Bozhevolnyi, J. Erland, K. Leosson, P.M.W. Skovgaard, and J.M. Hvam.

- Waveguiding in surface plasmon polariton band gap structures. *Phys. Rev. Lett.*, 86:3008–3011, 2001.
- [21] S.A. Maier, P.G. Kik, H.A. Atwater, S. Meltzer, E. Harel, B.E. Koel, and A.A.G. Requicha. Local detection of electromagnetic energy transport below the diffraction limit in metal nanoparticle plasmon waveguides. *Nature Materials*, 2:229–232, 2003.
- [22] W.L. Barnes, A. Dereux, and T.W. Ebbesen. Surface plasmon subwavelength optics. *Nature*, 424:824–830, 2003.
- [23] P. Michler et al. A quantum dot single-photon turnstile device. *Science*, 290:2282, 2000. P. Michler, A. Kiraz, C. Becher, W. V. Schoenfeld, P. M. Petroff, Lidong Zhang, E. Hu, and A. Imamoglu.
- [24] D.W. Pohl. *Scanning Near-field Optical Microscopy (SNOM)*, in *Advances in Optical and Electron Microscopy*, volume 12. Academic Press London, London, 1991. Editor:T. Mulvey and C. J. R. Sheppard.
- [25] D.P. Fromm, A. Sundaramurthy, P.J. Schuck, G.S. Kino, and W.E. Moerner. Gap-dependent optical coupling of single "bowtie" nanoantennas resonant in the visible. *Nano Lett.*, 4:957–961, 2004.
- [26] P.J. Schuck, D.P. Fromm, A. Sundaramurthy, G.S. Kino, and W.E. Moerner. Improving the mismatch between light and nanoscale objects with gold bowtie nanoantennas. *Phys. Rev. Lett.*, 94:017402–4, 2005.
- [27] K. Li, M.I. Stockman, and D.J. Bergman. Self-similar chain of metal nanospheres as an efficient nanolens. *Phys. Rev. Lett.*, 91:227402–4, 2003.
- [28] J.B. Pendry, L. Martin-Moreno, and F.J. Garcia-Vidal. Mimicking surface plasmons with structured surfaces. *Science*, 305:847–848, 2004.
- [29] G.T. Boyd, Z.H. Yu, and Y.R. Shen. Photoinduced luminescence from noble metals and its enhancement on roughened surfaces. *Phys. Rev. B*, 33:7923–7936, 1986.

- [30] M.R. Beversluis, A. Bouhelier, and L. Novotny. Continuum generation from single gold nanostructures through near-field mediated intraband transitions. *Phys. Rev. B*, 68:115433–10, 2003.
- [31] R.R. Alfano and S.L. Shapiro. Emission in the region 4000 to 7000 Å via four-photon coupling in glass. *Phys. Rev. Lett.*, 24:584–587, 1970.
- [32] Y.D. Qin, D.L. Wang, S.F. Wang, and Q.H. Gong. Spectral and temporal properties of femtosecond white-light continuum generated in h₂o. *Chin. Phys. Lett.*, 18:390–392, 2001.
- [33] P.A. Champert et al. White-light supercontinuum generation in normally dispersive optical fibre using original multi-wavelength pumping system. *Opt. Express*, 12:4366–4371, 2004.
- [34] D. von der Linde and H. Schueler. Breakdown threshold and plasma formation in femtosecond laser-solid interaction. *J. Opt. Soc. Am. B*, 13:216–222, 1996.
- [35] J.N. Farahani, D.W. Pohl, H.-J. Eisler, and B. Hecht. Single quantum dot coupled to a scanning optical antenna: A tunable superemitter. *Phys. Rev. Lett.*, 95:0174021–0174202, 2005.
- [36] J.-J. Greffet. Nanoantennas for light emission. *Science*, 308:1561–1562, 2005.
- [37] C. A. Balanis. *Antenna Theory*. John Wiley & Sons, Inc., Arizona State University, 2 edition, 1997.
- [38] R. King and C. W. Harrison. The distribution of current along a symmetrical center-driven antenna. *Proceedings of the I.R.E.*, pages 548–567, 1943.
- [39] K. F. Lee. *Principles of Antenna Theory*. John Wiley & Sons, Inc., The Chinese University of Hong Kong, 1 edition, 1984.
- [40] C. F. Bohren and D. R. Huffman. *Absorbption and Scattering of Light by Small Particles*. Wiley & Sons, Inc., Pennsylvania State University, 2 edition, 1998.

- [41] J. D. Jackson. *Classical Electrodynamics*. John Wiley & Sons, Inc., University of California, Berkeley, 3 edition, 1999.
- [42] C. A. Balanis. Antenna theory: A review. *Proceedings of the IEEE*, 80:7–22, 1992.
- [43] H.C. Pocklington. Electrical oscillations in wires. *Proceedings of the Cambridge Philosophical Society*, 9(7):324–332, 1897.
- [44] E. Hallén. Theoretical investigations into the transmitting and receiving qualities of antennae. *Nova Acta Regiae Societatis Scientiarum Upsaliensis*, 11(4):1–44, 1938.
- [45] S.J. Orfanidis. *Electromagnetic Waves and Antennas*. <http://www.ece.rutgers.edu/~orfanidi/ewa/>, ECE Department, Rutgers University, New Jersey, 2004.
- [46] R. Feynman. *The Feynman Lectures on Physics II*. Addison-Wesley Publishing Company, Massachusetts, 1 edition, 1989.
- [47] R.C. Compton, R.C. McPhedran, Z. Popovic, G. M. Rebeiz, P.P. Tong, and D.B. Rutledge. Antennas on a dielectric half-space: Theory and experiment. *IEEE Transactions on Antennas and Propagation*, AP-35:622–631, 1987.
- [48] C. Sönnichsen. *Plasmons in metal nanostructures*. Cuviller Verlag, Göttingen, 1 edition, 2001.
- [49] P.B. Johnson and R.W. Christy. Optical constants of noble metals. *Phys. Rev. B*, 6:4370–4379, 1972.
- [50] U. Kreibig and M. Vollmer. *Optical Properties of Metal Clusters*. Springer Series in Materials Science, University of California, Berkeley, 1 edition, 1995.
- [51] L.G. Schulz. The optical constants of silver, gold, copper and aluminum. *J. Opt. Soc. Am.*, 44:357–368, 1954.
- [52] E. Hutter and J.H. Fendler. Exploitation of localized surface plasmon resonance. *Adv. Mater.*, 16:1685–1706, 2004.

- [53] C. Sönnichsen, T. Franzl, T. Wilk, G. von Plessen, J. Feldmann, O. Wilson, and P. Mulvaney. Drastic reduction of plasmon damping in gold nanorods. *Phys. Rev. Lett.*, 88:077402, 2002.
- [54] M. Paulus and O.J.F. Martin. Light propagation and scattering in stratified media: A green's tensor approach. *J. Opt. Soc. Am. A*, 18:854–861, 2001.
- [55] A. Taflove and S.C. Hagness. *Computational Electrodynamics*. ARTECH HOUSE, INC., Boston, 3 edition, 2005.
- [56] J.M. López-Alonso, J.M. Rico-García, and J. Alda. Numerical artifacts in finite-difference time-domain algorithms analyzed by means of principal components. *IEEE Transaction on Antennas and Propagation*, 53:2920–2927, 2005.
- [57] R. E. Howard, E. L. Hu, L. D. Jackel, P. Grabbe, and D. M. Tennant. 400-linewidth e-beam lithography on thick silicon substrates. *Appl. Phys. Lett.*, 36:592–584, 1980.
- [58] Y. D. Park and et al. Fabrication of nanometr-sized magnetic structures using e-beam patterned deposition masks. *J. Appl. Phys.*, 81:4717–4719, 1997.
- [59] G. M. Shedd, H. Lezec, A. D. Dubner, and J. Melngailis. Focused ion beam induced deposition of gold. *Appl. Phys. Lett.*, 49:1584–1586, 1986.
- [60] S. Matsui and Y. Ochiai. Focused ion beam application to solid state devices. *Nanotechnology*, 7:247–258, 1996.
- [61] P. Hoffmann and et al. Direct writing of gold nanostructures using a gold-cluster compound and a focused-ion beam. *J. Appl. Phys.*, 74:7588–7591, 1993.
- [62] D. S. Kong, J. S. Varsanik, S. Griffith, and J. M. Jacobson. Conductive nanostructure fabrication by focused ion beam direct-writing of silver nanoparticles. *J. Vac. Sci. Technol. B*, 22:2987–2991, 2004.
- [63] V. Bouchiat and D. Esteve. Lift-off lithography using an atomic force microscope. *Appl. Phys. Lett.*, 69:3098–3100, 1996.

- [64] R. Lüthi, R. R. Schlittler, J. Brugger, P. Vettiger, M. E. Welland, and J. K. Gimzewski. Parallel nanodevice fabrication using a combination of shadow mask and scanning probe methods. *Appl. Phys. Lett.*, 75:1314–1316, 1999.
- [65] C. Martin, G. Rius, X. Borrise, and F. Perez-Murano. Nanolithography on thin layers of pmma using atomic force microscopy. *Nanotechnology*, 16:1016–1022, 2005.
- [66] C. Terrier. *Non-equilibrium coherent transport in mesoscopic conductors*. PhD thesis, Diss. phil.-nat., Univ. Basel, 2002.
- [67] D.-J. Kang H.-W. Li, M.G. Blamire, and W.T.S Huck. Focused ion beamfabrication of silicon print masters. *Nanotechnology*, 14:220–223, 2003.
- [68] C. J. Murphy and N. R. Jana. Controlling the aspect ratio of inorganic nanorods and nanowires. *Adv. Mater.*, 14:80–82, 2002.
- [69] C. J. Johnson, E. Dujardin, S. A. Davis, C. J. Murphy, and S. Mann. Growth and form of gold nanorods prepared by seed-mediated, surfactant-directed synthesis. *Journal of Materials Chemistry*, 12:1765–1770, 2002.
- [70] W.E. Moerener and D.P. Fromm. Methodes of single-moelecule fluorescence spectroscopy and microscopy. *Rev. Sci. Inst.*, 74:3597–3619, 2003.
- [71] F. de Fornel. *Evanescent Waves*. Springer Series in Optical Science, Berlin, 1 edition, 2001.
- [72] R. Carminati and J.-J. Greffet. Two-dimensional numerical simulation of the photon scanning tunneling microscope. concept of transfer function. *Opt. Commun.*, 115:316–321, 1995.
- [73] B. Hecht, H. Bielefeldt, Y. Inouye, D. W. Pohl, and L. Novotny. Facts and artifacts in near-field optical microscopy. *J. Appl. Phys.*, 84:2492–2498, 1997.
- [74] A. Dereux, C. Girard, and J.-C. Weeber. Theoretical principles of near-field optical microscopies and spectroscopies. *J. Chem. Phys.*, 112:7775–7789, 2000.

- [75] J. C. Weeber et al. Near-field observation of surface plasmon polariton propagation on thin metal stripes. *Phys. Rev. B*, 64:045411, 2001.
- [76] S. I. Bozhevolnyi, V. S. Volkov, E. Devaux, and W. Ebbesen. Channal plasmon-polariton guiding by subwavelength metal grooves. *Phys. Rev. Lett.*, 95:046802, 2005.
- [77] M. L. M. Balistreri, J. P. Korterik, L. Kuipers, and N. F. van Hulst. Photon scanning tunneling optical microscopy with a three-dimensional multiheight imaging mode. *Appl. Phys. Lett.*, 77:4092–4094, 2000.
- [78] S. I. Bozhevolnyi, V. S. Volkov, T. Sndergaard, A. Boltasseva, P. I. Borel, and M. Kristensen. Near-field imaging of light propagation in photonic crystal waveguides: Explicit role of bloch harmonics. *Phys. Rev. B*, 66:235204, 2002.
- [79] R. Quidant et al. Addressing and imaging microring resonators with optical evanescent light. *Phys. Rev. B*, 69:081402, 2004.
- [80] A. Gustafsson, M.-E. Pistol, L. Montelius, and L. Samuelson. Local probe techniques for luminescence studies of low-dimensional semiconductor structures. *J. Appl. Phys.*, 84:1715–1775, 1998.
- [81] V.I. Safarov, V.A. Kosobukin, C. Hermann, G. Lampel, C. Marliere, and J. Peretti. Near-field magneto-optics with polarization sensitive stom. *Ultramicroscopy*, 57:270–276, 1995.
- [82] G. Krausch, S. Wegscheider, A. Kirsch, H. Bielefeldt, J.C. Meiners, and J. Mlynek. Near field microscopy and lithography with uncoated fiber tips: a comparison. *Opt. Commun.*, 119:283–288, 1995.
- [83] M. Minsky. Memoir on inventing the confocal scanning microscope. *Scanning*, 10:128–138, 1988.
- [84] R.H. Webb. Confocal optical microscopy. *Rep. Prog. Phys.*, 59:427–471, 1996.
- [85] J. A. Buck. *Fundamentals of Optical Fibers*. Wiley & Sons, Inc., Massachusetts,

1 edition, 1995.

- [86] B. Lamprecht. *Ultrafast plasmon dynamics in metal nanoparticles*. PhD thesis, Institute for Experimental Physics, Karl-Franzens-Univ. Graz, 2000.
- [87] J. Aizpurua, G.W. Bryant, L.J. Richter, F.J. García de Abajo, B.K. Kelley, and T. Mallouk. Optical properties of coupled metallic nanorods for field-enhanced spectroscopy. *Phys. Rev. B*, 71:235420, 2005.
- [88] W. Rechberger, A. Hohenau, A. Leitner, J.R. Krenn, B. Lamprecht, and F.R. Aussenegg. Optical properties of two interacting gold nanoparticles. *Optics Commun.*, 220:137–141, 2003.
- [89] R. Stöckle, C. Fokas, V. Deckert, R. Zenobi, B. Sick, B. Hecht, and U. P. Wild. High-quality near-field optical probes by tube etching. *Appl. Phys. Lett.*, 75:160–162, 1999.
- [90] D. Barchiesi and D. Van Labeke. A perturbative diffraction theory of a multilayer system: applications to near-field optical microscopy snom and stom. *Ultramicroscopy*, 57:196–203, 1995.
- [91] K. Karrai and R. D. Grober. Piezoelectric tip-sample distance control for near field optical microscopes. *Appl. Phys. Lett.*, 66(14):1842–1844, 1995.
- [92] K. Karrai and R. D. Grober. Piezo-electric tuning fork tip-sample distance control for near field optical microscopes. *Ultramicroscopy*, 61(1-4):197–205, 1995.
- [93] J. Barenz, O. Hollricher, and O. Marti. An easy-to-use non-optical shear-force distance control for near-field optical microscopes. *Rev. Sci. Instrum.*, 67(5):1912–1916, 1996.
- [94] A. G. T. Ruiter, K.O. van der Werf, J.A. Veerman, M. F. Garcia-Parajo, W. H. J. Rebsen, and N. F. van Hulst. Tuning fork shear-force feedback. *Ultramicroscopy*, 71:149–157, 1998.
- [95] J. Salvi, P. Chevassus, A. Moufard, S. Davy, M. Spajer, D. Courjon, K. Hjort, and

- L. Rosengren. Piezoelectric shear force detection: A geometry avoiding critical tip/tuning fork gluing. *Rev. Sci. Instrum.*, 69(4):1744–1746, 1998.
- [96] D. Mulin, C. Vannier, C. Bainier, D. Courjon, and M. Spajer. Easy-to-use unglued tip replacement near-field optical microscope with piezoelectric shear force detection. *Rev. Sci. Instrum.*, 71(9):3441–3443, 2000.
- [97] A. Crottini, J. L. Staehli, B. Deveaud, X. L. Wang, and M. Ogura. Ultra stable tuning fork sensor for low-temperature near-field spectroscopy. *Ultramicroscopy*, 90(2-3):97–101, 2002.
- [98] J. Rychen, T. Ihn, P. Studerus, A. Herrmann, K. Ensslin, H.J. Hug, P.J.A. Schendel, and H.J. Güntherodt. Operation characteristics of piezoelectric quartz tuning forks in high magnetic fields at liquid helium temperatures. *Rev. Sci. Instrum.*, 71:1695–1697, 2000.
- [99] C. Zilg, R. Mülhaupt, and J. Finter. Morphology and toughness/stiffness balance of nanocomposites based upon anhydride-cured epoxy resins and layered silicates. *Macromol. Chem. Phys.*, 200:661–670, 1999.
- [100] D. Sarid. *Scanning Force Microscopy*. Oxford University Press, revised edition, 1994.
- [101] K. Karrai and I. Tiemann. Interfacial shear force microscopy. *Phys. Rev. B*, 62(19):13174–13181, 2000.

Appendix

A. First Appendix

A.1. Glue-free tuning fork shear-force microscope

A.1.1. Introduction

Piezoelectric shear-force sensors are widely used for probe-sample distance control in scanning near-field optical microscopy (SNOM) [91–97], and other scanning probe techniques (see [98] for further ref.) In SNOM usually the optical probe is attached to a quartz tuning fork (TF), of the type used in watches. The interaction of the probe with the surface induces a shift of the TF's resonance frequency. This shift or the resulting impedance change can be used for distance control by means of a feedback mechanism acting on the so-called z-piezo, usually a piezo-electric ceramic tube. The TF is excited either mechanically by a piezo-electric element, or electrically by a driving voltage applied directly to the TF [92]. The stiffness and fragility of fiber SNOM probes requires a sensitive and fast feedback to prevent probes from crashing during approach and scanning. Therefore a sensor with high quality factor (Q), in combination with a phase-locked loop (PLL) feedback system, is desirable.

The standard method of connecting a fiber probe to the TF is gluing with epoxy [91, 94, 97]. This process is somewhat problematic since the adhesive tends to form a thin cushion between fiber and TF. The latter forms a "soft" connection because the elastic properties of quartz and epoxy are widely different, the elastic modulus of the latter being $20\times$ smaller than that of quartz (see e.g. [99]) and also having appreciable loss at the typical tuning fork frequencies ($= 32$ kHz). To minimize the resulting damping, the gluing process has to be controlled carefully which requires considerable skill and experience. Once glued, a probe neither can be removed easily, e.g. for characterization, nor can a poorly glued probe be readjusted after curing of the epoxy.

To circumvent probe gluing, mechanical fixation by clamping the fiber probe between the two arms of a TF [95] or connecting the probe to a home-built piezo-ceramic TF [96] has been suggested. The present scheme is based on the same principle, however relying on an improved mechanical design. It provides adjustable Q factors as high as ~ 4000 , resulting in high force sensitivity and in conjunction with a PLL short feedback response time. The very simple compact implementation allows for particularly fast, easy, and reproducible probe exchange. The piezo-ceramic tube used as z-piezo, is mounted between two adaptors kept together by means of an appropriately designed screw instead of an adhesive. The elimination of glued parts from the z-piezo results in similar advantages as described for the shear force sensor although epoxy cushion formation is less critical in this case because of the larger masses involved. The main improvements here are ease of mounting and replacement, aside from well-defined mechanical parameters and higher Q.

A.1.2. Design and Characterization

Fig. A.1 and Fig. A.2 show the relevant parts of the SNOM head. The fixation of probe holder base plate (BP) and z-piezo tube (PT) was designed by J. Toquant and is illustrated in Fig. A.1A. Screw S (steel) exerts a compression force on the assembly that is adjusted by means of a sensitive torque wrench. Torques in the range of 3 to 8 cNm were found to provide stable fixation without damage of the brittle piezo-ceramic material (PZT Staveley EBL3, length = 35 mm , $D = 6.25$ mm, $w = 0.5$ mm).

The electromechanical response of the PT is influenced marginally only by the screw. Since the elastic moduli of steel and standard piezo-ceramics are roughly the same, the longitudinal (z-direction) piezoelectric expansion is reduced in proportion to the ratio of the cross sectional areas which is $< 17\%$, hence irrelevant in most applications. With respect to bending (lateral scanning), the influence is completely negligible since here the area moments of inertia are the relevant parameter which differ by more than three orders of magnitude. Fig. A.1B displays the mechanical resonances of the PT, measured with a spectrum analyzer, the excitation voltage being applied to one pair of the quadrant electrodes of the PT, the signal being picked up from the other pair. The measurement was performed for two different torques applied to screw S and for a conventionally glued z-piezo. Apparently, the low-frequency resonances of the glued piezo tube move

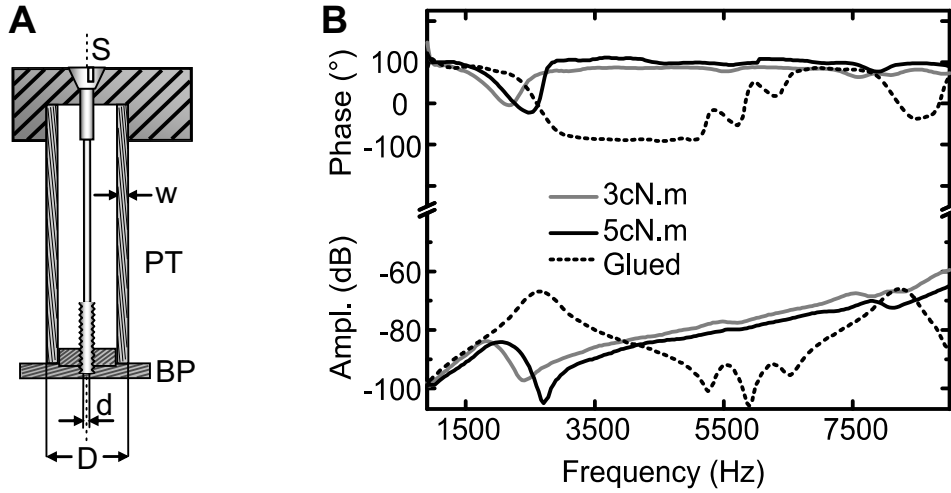


Figure A.1.: Scanner assembly and resonance behavior. (A) Sketch of the clamped piezo tube (PT). S: fixation screw, D: PT outer diameter, w: width of PT walls, d: diameter of the screw. (B) Resonance curves of the clamped piezo tube for different torques exerted on the screw, compared to a glued piezo tube. (Top Phases shift. Bottom: Normalized amplitudes. Designed and measured by J. Toquant).

to higher frequencies for the unglued, clamped piezo.

TF and the fiber probe with removed coating are mounted in separate blocks B1 and B2 (Fig. A.2A, B) such that the fiber is pressed against one prong of the slightly tilted TF near its end. The blocks are screwed to the insulating base plate (BP). The relative position of the blocks determines the position H of mechanical contact between TF and fiber and the amount of fiber bending Δx_F that was adjusted to $\approx 100 \mu\text{m}$ (Fig. A.2C). Bending of the fiber results in a force $F = \Delta x_F \cdot k_F$ acting on the TF. The spring constant of the slightly bent cylindrical fiber, anchored on one side, was calculated as [100] $k_F = (3\pi \cdot E \cdot R^4)/(4 \cdot l_1^3)$ ($\approx 600 \text{ N/m}$). Here E , R , and l_1 are Young's modulus, radius and length of the bent part of the fiber, respectively. With $E = 6 \cdot 10^{10} \text{ N/m}^2$ (SiO_2) [100], $R = 62.5 \mu\text{m}$, $l_1 = 1.5 \text{ mm}$ (Fig. A.2C), the total force exerted by the fiber on the TF amounts to 0.06 N. For stable operation it is instrumental that the probe follows the motion of the tuning fork prong without losing contact at any moment in time during the tuning fork oscillation. The acceleration $\ddot{x}_F(l_1)$ of the free fiber towards the prong hence has to be larger than the maximum acceleration $\ddot{x}_T(H)$ of the TF prong during vibration. To calculate \ddot{x}_F and \ddot{x}_T the solution to the equation of motion of a vibrating lever (fiber respectively TF prong) has to be separated: [100] $x_{F/T}(z, t) =$

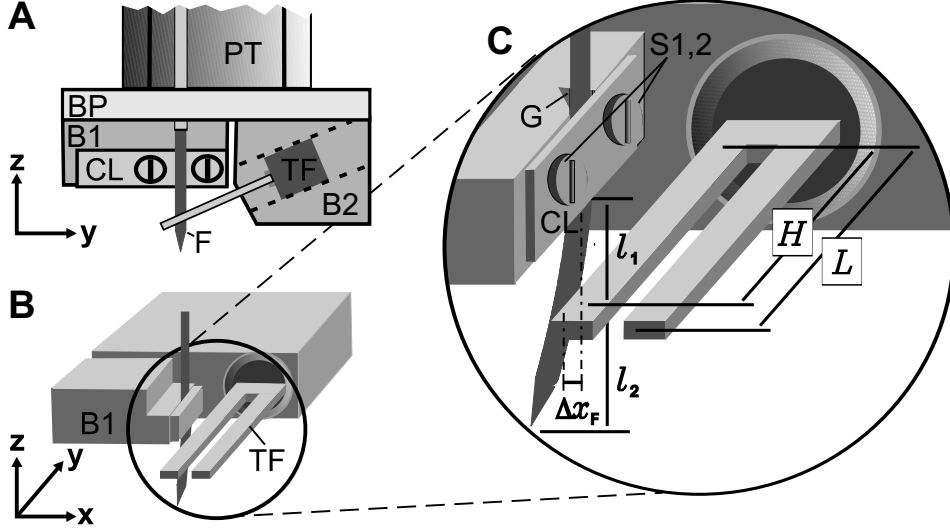


Figure A.2.: Sketch of the tuning fork mount. (A) side view. PT: piezo-tube, BP: insulating base plate, TF: tuning fork, F: fiber, CL: clamp, B1: block with clamp and screws for fiber fixation, B2: block with incorporated TF. (B) rotated view without PT and BP. (C) Magnification of the indicated position in (B). G: grove for fiber guidance, S1,2: screws for clamp fixation, Δx_F : fiber bending amplitude, l_1 : distance between fixed fiber end and TF, l_2 : length of free fiber end, H : distance between TF base and fiber, L : TF length

$x_{F/T}(z) \cdot \exp(i\omega t)$. The maximum acceleration for the fundamental resonance frequency $\omega_{F/T}$ follows as:

$$|\ddot{x}_{F/T}(z)|_{max} = |\omega_{F/T}^2| \cdot |\Delta x_{F/T}(z)|, \quad (\text{A.1})$$

where $|\Delta x_{F/T}(z)|$ is the maximum bending amplitude of the lever. The fundamental resonance frequency of an oscillating fiber with a circular cross-section fixed on one end is: [100]: $\omega_F = 1.76 \sqrt{\frac{E}{\rho}} \cdot R/l^2 \approx 2\pi \cdot 15 \text{ kHz}$ where $\rho = 2.2 \cdot 10^3 \text{ kg/m}^3$ is the specific mass density of SiO_2 [100], and $l = l_1 + l_2 \approx 2.5 \text{ mm}$ the length of the oscillating free fiber (Fig. A.2C). This results in $|\ddot{x}_F(l_1)|_{max} \approx 8 \cdot 10^5 \text{ m/s}^2$. The vibration amplitude $|\Delta x_T(H)|$ of the free TF was estimated from the driving voltage $V_D = 0.8 \text{ mV}$ and resulting current signal $I_{max} \approx 1.4 \text{ nA}$ of our TF (length: $L = 4.0 \text{ mm}$, thickness: $T = 0.63 \text{ mm}$, width: $W = 0.35 \text{ mm}$, res. freq.: $\omega_T = 2\pi \cdot 32768 \text{ Hz}$, static spring constant $k_{stat} = 26.9 \mu\text{N/nm}$) by comparison with data for a TF of a similar type [92] where $V_D = 2 \text{ mV}$, $I_{max} = 2.9 \text{ nA}$ and a vibration amplitude of 0.4 nm were measured. This yields $|\Delta x_T(H)| < 1 \text{ nm}$ and hence $|\ddot{x}_T(H)|_{max} < 40 \text{ m/s}^2$. Thus $|\ddot{x}_F(l)|_{max} \gg |\ddot{x}_T(H)|_{max}$ which ensures save contact between fiber and TF.

The ratio $R = L/H$ between total TF-length L and fiber mounting position H (Fig. A.2C) shows a strong influence on the Q factor of the coupled system fiber/TF, also reported by Crottini [97]. The position H can be tuned to optimum condition in our arrangement by appropriate adjustment of B1 and B2 with respect to the base plate (BP) (Fig. A.2A, B). Once B1 and B2 are fixed in a favorable position. the probe (fiber) can be replaced within a few minutes by loosening screws (S1,2). Clamp CL opens up such that the old fiber can easily be pulled out from groove G and be replaced by a fresh one (Fig. A.2C).

To characterize the influence of the fiber on the TF, a fiber was mounted and unmounted 10 times and the resonance was measured each time (Fig. A.3). An average resonance

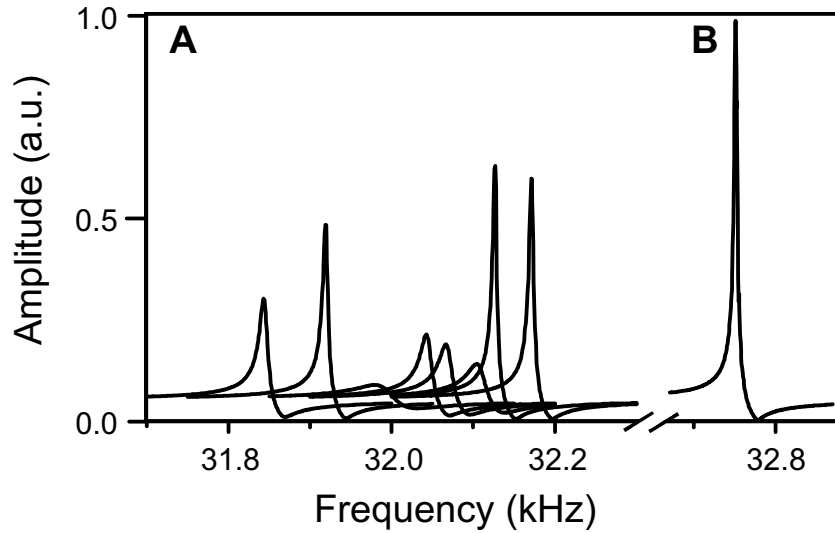


Figure A.3.: (A) Resonance curves for a repeatedly mounted fiber. (B) Resonance of the freely oscillating tuning fork.

frequency $\bar{f}_0 = 32047 \pm 250$ Hz and an average $\bar{Q} = 2032 \pm 1612$ factor were determined. Since the static spring constant k_{stat} of the TF is hardly altered by the fiber, we assign the observed shift (≈ -700 Hz) of the resonance for the coupled fiber/TF system with respect to the free TF (Fig. A.3B) to the increase in effective mass m_0 due to the attached fiber. The scattering of the data is attributed to the uncertainty in length l_2 . The deviation in Q is due to slight variations in clamp fixation (Fig. A.2C).

Samples were mounted on a regulated x-y scan stage (Physik Instrumente, P-733) for imaging. The TF current signal was pre-amplified and converted to an oscillating voltage by a current to voltage amplifier (amplification factor: $2 \cdot 10^7$). Gap width feedback

control was established by means of a phase-locked loop (PLL, Nanosurf AG) and the pre-amplified TF signal. The use of a PLL reduces the response time of the feedback system [94]. Fiber probes were produced by tube etching [89], followed by hot sulfuric acid (96%) removal of the fiber coating on the tip end side.

A.1.3. Operation

Approach curves and shear-force images of a SiO_2 calibration sample were recorded to demonstrate the functionality and robustness of the glue-free TF shear-force microscope. Fig. A.4 shows the damping of the voltage oscillation amplitude and the frequency shift when the tip is approached to and retracted from the SiO_2 surface.

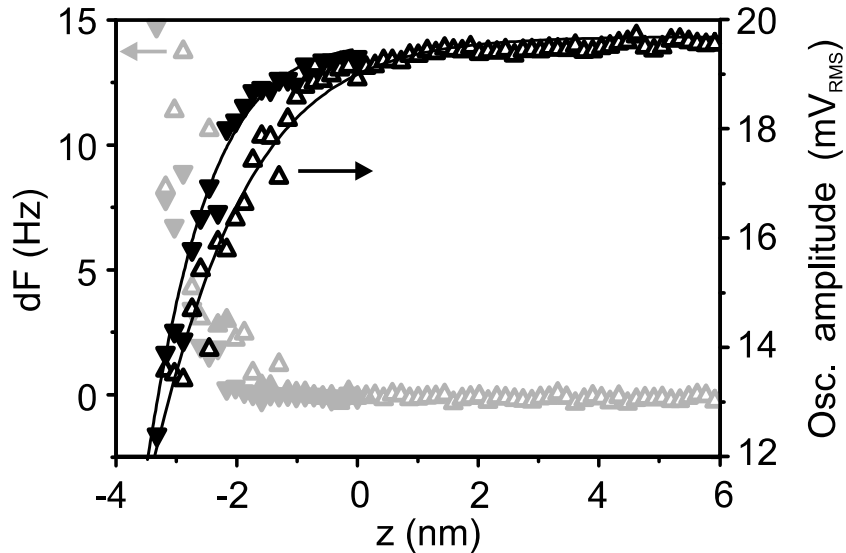


Figure A.4.: Approach curve towards a SiO_2 surface. Voltage oscillation amplitude (black) and frequency shift dF (gray) are recorded during approach (filled triangles) and retract (open triangles) starting from position $z = 0$.

Approach was started in gentle shear-force contact ($z = 0$). Retraction was triggered when the oscillation amplitude reached a predefined lower limit. The deviation between approach and retraction curves is caused by hysteresis of the z -piezo. The fit curves were obtained from a shear-force model [101] describing the damping of the resonance amplitude for an approaching tip. The amplitude drops within 3 nm to 70% of its undisturbed value, comparable to the data reported by others [96, 97]. The resonance frequency was found to increase simultaneously with the damping in amplitude.

Fig. A.5a depicts a shear-force image of a SiO₂ calibration sample, consisting of a 2-dimensional lattice of inverted square pyramids with 200 nm pitch etched into a silicon chip.

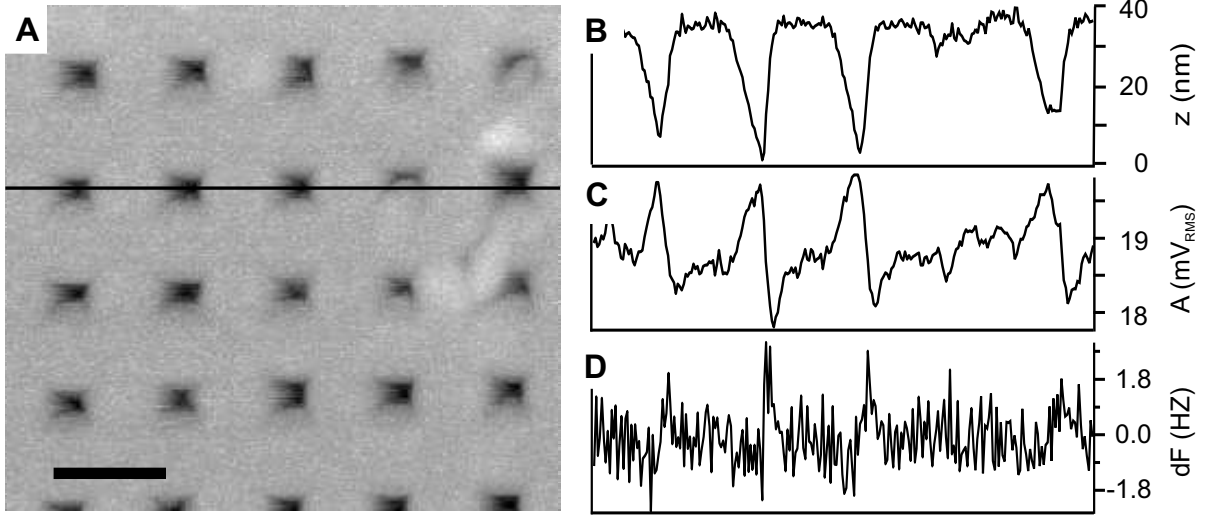


Figure A.5.: (A) Shear-force image of a SiO₂ calibration sample (2D200 by Nanosensors, 200 nm scalbar). (B-D) Indicated line profile from (A). (B) z : Topography signal. (C) A : Voltage oscillation amplitude. (D) dF : Frequency shift (error signal).

Fig. A.5B-D show data recorded along the line marked in Fig. A.5A, topography, the voltage oscillation amplitude, and the frequency shift. At a scans speed of 1 $\mu\text{m/s}$ the topography profile is slightly asymmetric due to the feedback response time (Fig. A.5B), however the amplitude never dropped below 90% (Fig. A.5E). A tip radius of ~ 23 nm was determined by comparing Fig. A.5B with the specifications of the calibration sample.

A.1.4. Summary

The presented tuning-fork microscope with unglued exchangeable probe and piezo-tube achieves a performance e.g. imaging quality and approach stability comparable to the best conventionally glued designs. Probe mounting and replacement, as well as mounting of the piezo-tube, however is much easier, more reproducible, and extremely fast. The absence of glue will be of particular advantage for operation at non-ambient conditions. The adjustability of the Q factor finally allows for an optimal tuning of the feedback

loop.

B. Second Appendix

B.1. Programming

B.1.1. antenna.m

The MATLAB routine pockling.m, which is used here to calculate the antenna current distribution was obtained from [45].

```
V0=1 ; % applied feed-gap voltage
a=1/500; % antenna diameter relative to wavelength
k=2*pi; % incident wavelength set to 1
L=1/8 ; % starting antenna length; L=1: full-wave antenna
Anz=100; % number of different antenna lengths
dL=2/Anz ; % length increase
M=50; % number of moments
type=1;
for n = 1 : Anz % antenna length L(n): L=1/8+(n-1)*dL
    h=L/2; % length of antenna arm
    Dz=h/(M+type*0.5); %
    E=zeros(2*M+1,1); % array representing external field
    E(M+1)= V0/Dz; % delta gap model (excitation in feed-gap)

    %Sinusoidal Current Approximation
    Rc=377; % free space impedance
    Om = 2*log(2*h/a);
    Im(n)=(2*pi*V0)/(Rc*Om*cos(h*k)); %first order approximation
    z= -h : h/Anz : h;
    Is=Im(n)*sin(k*(h-abs(z)));
    Isn(n,:)=Is;
    zs(n,:)=z;

    %Pocklington current distribution
    [In,zn,cnd]=pockling(L,a,E,16,type); % returns Pocklington current distribution
    % L: antenna length, a: radius,
```

B. Second Appendix

```

% E: array representing feed-gap model
Inn(:,n)=In;
znn(:,n)=zn;

%-----Transmitting Antenna-----
Za(n)=V0/In(M+1); % antenna impedance
Ig(n)=V0/Za(n);   % generator current and radiated power; assuming: Zg=0
P(n)=1/2*abs(Ig(n)).^2*Za(n); %complex average radiated power

%-----Receiving Antenna-----
E0=1 ; % incident field on receiving antenna
Isc(n)=(E0/V0)*trapz(zn,In); % approx. of current in receiving antenna
Voc(n)=Isc(n)*Za(n); % open circuit voltage

% Capacitive load represented by gap
d=5*10.^(-9); % gap sizes (5 nm)
r=20*10.^(-9); % antenna radius (20 nm)
A=pi*r.^2;
ebs0=8.85*10.^(-12)
ebs=1; % permittivity
C=(A*ebs*ebs0)/d; % feed-gap capacity (plate capacitor)
w=2*pi*3*10.^8/(830*10.^(-9)) ; % frequency
ZL=1/(i*w*C) ; % capacitive load

% Antenna current and received/reradiated power
Ia(n)=Voc(n)/(ZL+Za(n));
PL(n)=1/2*abs(Ia(n)).^2*ZL ; % average power delivered to load
Pa(n)=1/2*abs(Ia(n)).^2*Za(n) ; % average reradiated power
% -----

L=L+dL; % new antenna length
end

%-----PLOT-----
n= 1 : 1 : Anz;
mpl=max(abs(PL));
mpr=max(abs(Pa));
Ln=1/8+(n-1)*dL ; % array number -> antenna length assignment

%-----Transmitting Antenna-----
plot(Ln,real(P),Ln,imag(P)); % complex average radiated power

%-----Receiving Antenna-----

```

B. Second Appendix

```
plot(Ln,abs(Pa),Ln,abs(PL),'--'); %average power reradiated / delivered to load
plot(Ln,abs(Ia(n)*ZL/d).^2); % field enhancement in gap

% -----Antenna Impedance -----
plot(real(Za),imag(Za));

%----- Current Amplitude Versus Antenna Length -----
plot(Ln,max(abs(Inn(:,n))),'.-',Ln,abs(Im(n))); % Pocklington and sinusoidal
% approximation

% ----- Current Distribution for Specific Antenna Length -----
AL=0.5; % antenna length in wavelength
nr=round((AL-1/8)/dL+1);
Isn=Isn(nr,:);
zsh=zs(nr,:);
Innh=Inn(:,nr);
znnh=znn(:,nr);
misn=max(abs(Isnh));
minn=max(abs(Innh));
phi=atan(imag(Innh)/real(Innh));
plot(znnh,abs(Innh),'.',zsh,abs(Isnh)*minn/misn); %antenna current distribution
plot(znnh,abs(phi*180/pi),'--'); % current phase
```

B.1.2. plasmon.m

```
b=20*10.^(-9); % semi axes of ellipsoid
Anz=400; % number of calculated lengths
da=200*10.^(-9)/Anz % Length increase
em= (1+2.25)/2 ; % approx. permittivity of glass/air interface

%calculates array of polarizability of ellipsoid for different lengths
a=2*b; % starting length
e1=-25+i*1.6 % permittivity of gold at 800 nm
for n = 1 : Anz
    e=sqrt(1-(b/a).^2);
    L1(n)=((1-e.^2)/e.^2)*(-1+(1/(2*e))*log((1+e)/(1-e)));
    alph1(n)=4*pi*a*b*b*((e1-em)/(3*em+3*L1(n)*(e1-em)));
    a=a+da;
end

%calculates array of polarizability of ellipsoid for different lengths
a=2*b; % reset starting length
```

B. Second Appendix

```
e1=-46+i*29    % dielectric constant of aluminum at 800 nm
for n = 1 : Anz
    e=sqrt(1-(b/a).^2);
    L1(n)=((1-e.^2)/e.^2)*(-1+(1/(2*e))*log((1+e)/(1-e)));
    alph2(n)=4*pi*a*b*b*((e1-em)/(3*em+3*L1(n)*(e1-em)));
    a=a+da;
end n= 1 : 1 : Anz;

L=2*(2*b+da*(n-1)); % array with different lengths
plot(L,abs(alph1) ,L,abs(alph2)); % plots polarizability of gold and aluminum
                                % for different ellipsoid lengths
```

C. Third Appendix

C.1. Overview of Analyzed Optical Antennas

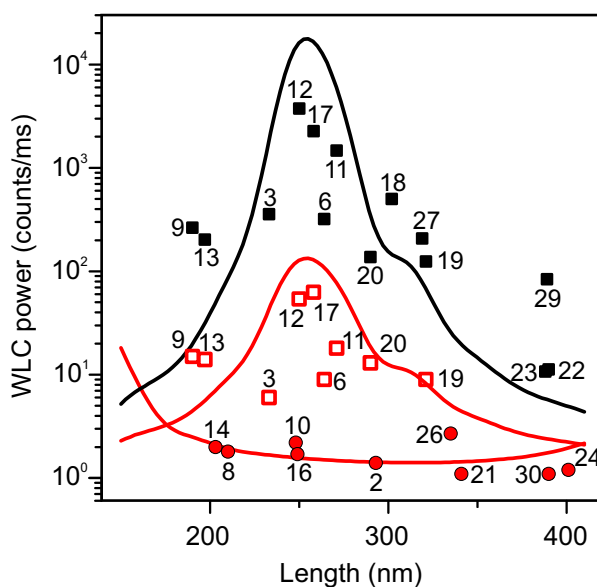


Figure C.1.: Fig. 7.6 with assignment of data points to the specific structures shown in Figs. C.2, C.3, C.4

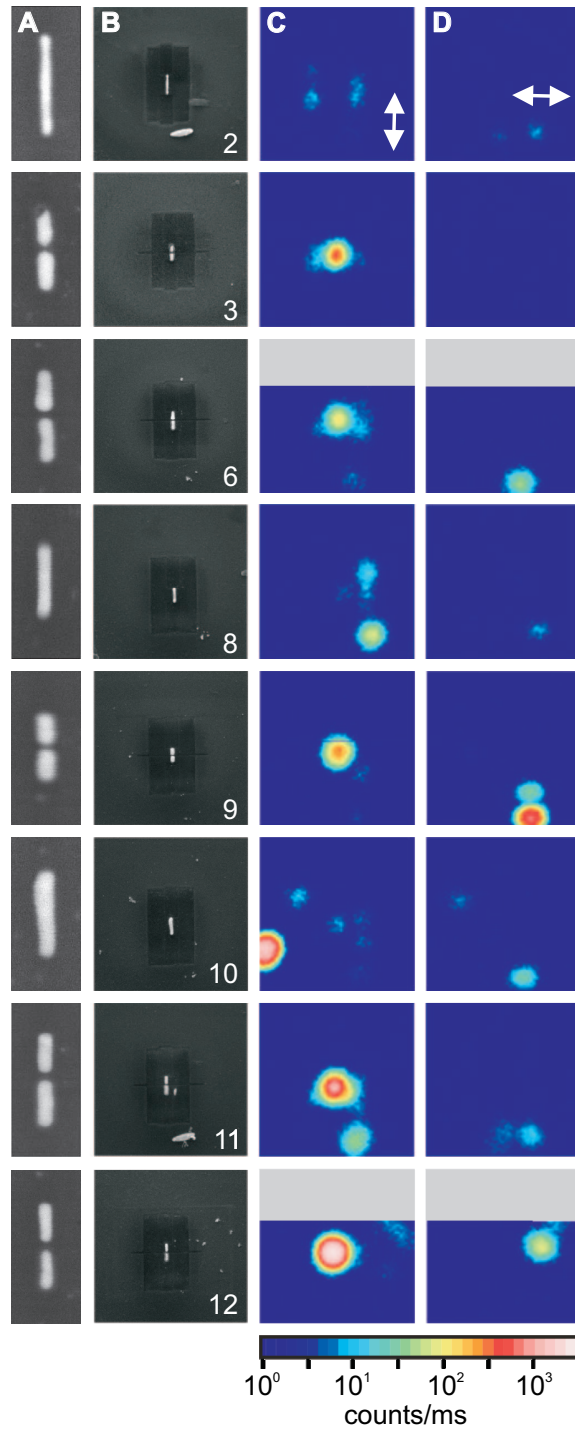


Figure C.2.: (A and B) SEM images, zoom and overview, respectively. (C and D) confocal scan images of the WLC generated by vertically and horizontally polarized laser pulses, respectively (average power $110 \mu\text{W}$, logarithmic color code). Dimensions: (A) $200 \times 450 \text{ nm}^2$; (B to D) $2.5 \times 2.5 \mu\text{m}^2$.

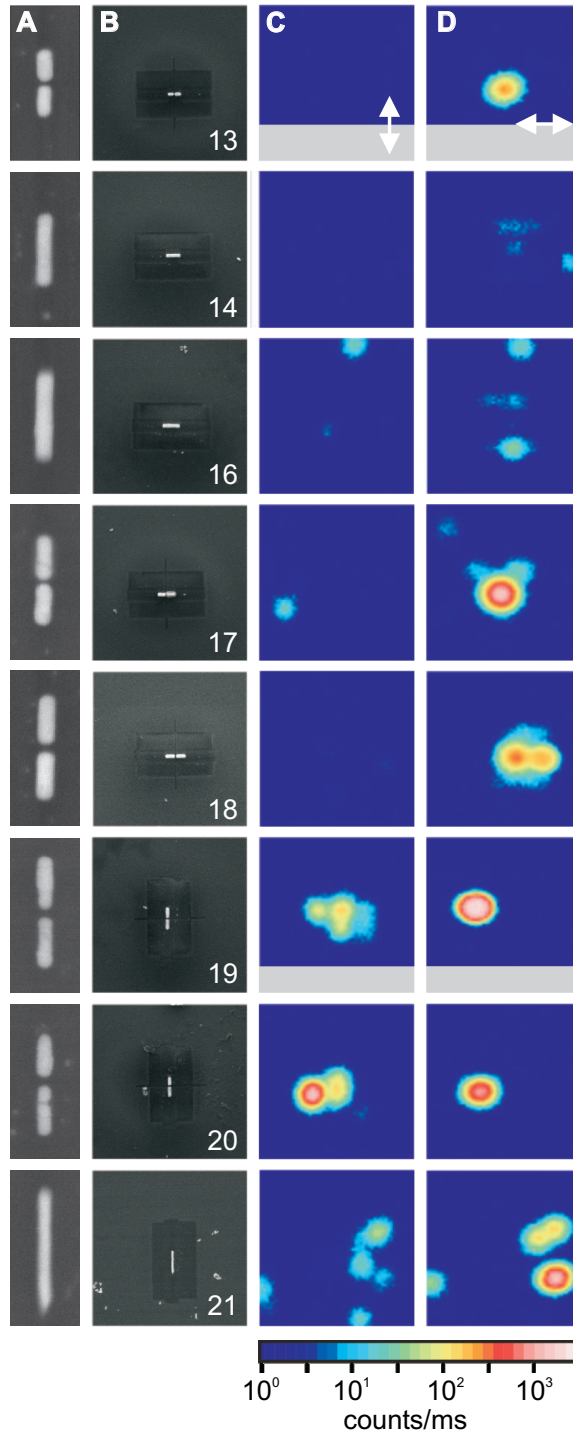


Figure C.3.: (A and B) SEM images, zoom and overview, respectively. (C and D) confocal scan images of the WLC generated by vertically and horizontally polarized laser pulses, respectively (average power $110 \mu\text{W}$, logarithmic color code). Dimensions: (A) $200 \times 450 \text{ nm}^2$; (B to D) $2.5 \times 2.5 \mu\text{m}^2$.

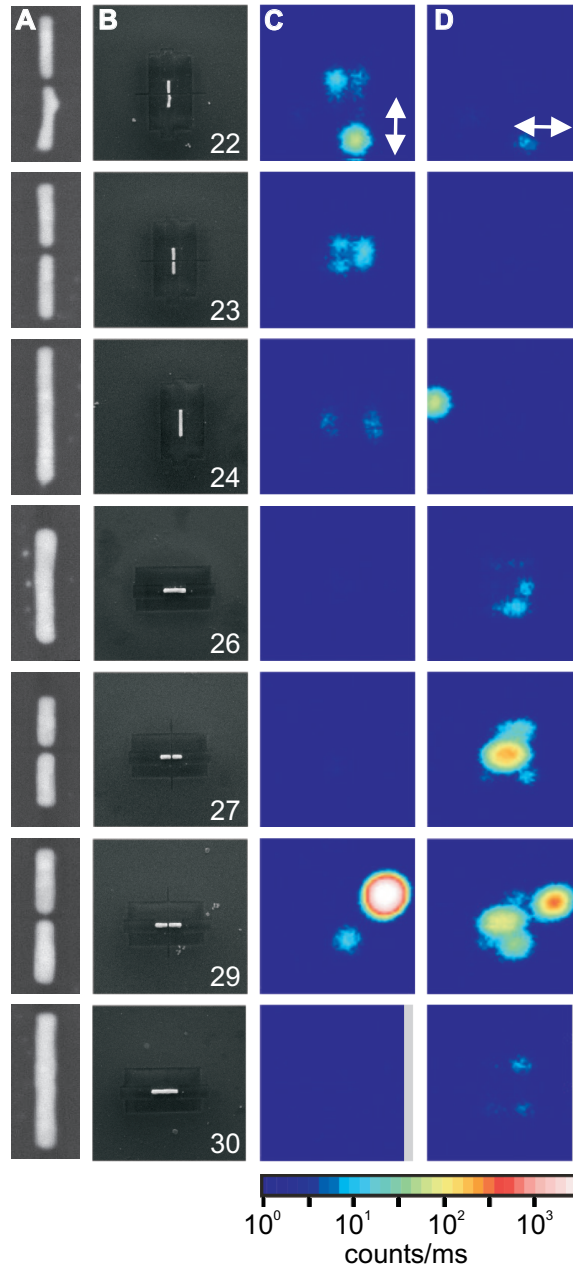


Figure C.4.: (A and B) SEM images, zoom and overview, respectively. (C and D) confocal scan images of the WLC generated by vertically and horizontally polarized laser pulses, respectively (average power $110 \mu\text{W}$, logarithmic color code). Dimensions: (A) $200 \times 450 \text{ nm}^2$; (B to D) $2.5 \times 2.5 \mu\text{m}^2$.

Acknowledgements

First of all I thank Prof. D. W. Pohl, who initiated the research on optical antennas. He invited me to Basel and organized the first financial support. I thank Prof. B. Hecht, who organized further financial support needed for this work. Both supervisors were open for discussions and very help full in experimental and theoretical questions - thank you I learned a lot. I thank Prof. H.-J. Güntherodt for the opportunity to use many of the facilities in his group and for the help when additional money was needed.

Further I thank all the peoples who supported this work with their contribution and help.

Prof. O. J. F. Martin from the EPFL, performed initial near-field simulations of optical dipole antennas, that helped to estimate the achievable field enhancement in the antenna feed gap.

Ph. Gasser and S. Meier from the EMPA in Dübendorf I thank for the operation of the FIB.

Prof Ch. Schönenberger and his group allowed me to use their e-beam facilities and gave me help in questions concerning micro fabrication.

The group of Prof. P. Oelhafen, especially J. Boudaden and I. Mack, who spend a sunny Sunday to prepare the ITO coated glass substrates.

Dr. H.-J. Eisler for organizing the spectrometer and help for aligning the fs-laser.

V. Thoman, who introduced me into AFM imaging and found the sharpest tip for me.

H.-R. Hidber and his team of the electronic workshop for taking care of all my electronic problems.

P. Cattin and S. Martin and their teams in the mechanical workshop, who realized my ideas for setting up and improving the experimental setup.

Dr. M. Hegner for the place in his office and labor, help in software problems and the green plants in the dark basement.

Dr. W. Grange, who encountered peculiar LabView problems just a short time before me and was a great help during setting up the data acquisition and the experimental setups.

G. Weaver, B. Kammermann and A. Kalt for their administrative work.

I thank all the members of the nano-optics group: J. Butter, J. Farahani, S. Karotke, A. Lieb, Y. Lill, T. Steinegger, J. Toquant. They helped out whenever help was needed. Together we had some nice evenings at the Rhine and at the "Soder's Straussi".

A special thank to Iris my dear fellow and little Silvan, who thought me that there is also plenty of life beside work.

Last but not least, I thank my parents for their continuous, not only financial support during my studies.

Curriculum Vitae

Peter Mühlshlegel

Geburtstag: 26. Mai 1972

Geburtsort: Biberach an der Riss, Deutschland

- 10/2001-02/2006 Dissertation am Institut für Physik der Universität Basel (CH)
- 03/2001-08/2001 Wissenschaftlicher Mitarbeiter, Universität Tübingen (D)
- 10/1994-02/2001 Physikstudium an der Universität Tübingen mit den Nebenfächern Informatik und Elektronik. Abschluss mit dem Diplom in Physik.
- 08/1997-09/1998 Studienaufenthalt in den USA, Montana State University und Los Alamos National Laboratory
- 06/1992-09/1993 Zivildienst in der Allgemeine Chirurgie, Universitätsklinikum Tübingen.
- 08/1979-05/1992 Schulausbildung in Biberach. Abschluß mit der Allgemeine Hochschulreife.

Folgenden Dozenten verdanke ich meine Ausbildung

- Universität Basel: D. W. Pohl, B. Hecht, H.-J. Güntherodt, H.-J. Eisler, M. Hegner, Ch. Schönenberger, M. Calam, H. J. Hug, E. Meyer
- Universität Tübingen: M. Peschka, R. Kleiner, R. Hübener, D. Kern, D. Waram, P. Kramer, N. Schopohl, M. Baumann, A. Fessler, H. Fischer, H. Kaul, O. Eible, E. Plies, F. Gönnerwein, G. Wagner, H. Klaeren
- Montana State Univ.: J. Hermanson, G. Tuthill
- Los Alamos National Lab.: S. Gerstel